Università degli Studi di Pisa

Dipartimento di Fisica
Tesi di Dottorato di Ricerca in Fisica Applicata

Submitted by

Tiruppattur Rajamanikkam Saravanan

Thesis advisor

Prof. Anna M. Nobili

Referees

Prof. C.S. Unnikrishnan
Dr. Valerio Iafolla

Ground prototype of a rotating differential accelerometer for testing the Equivalence Principle in space: commissioning and reduction of low frequency noise

December 2012

Dedication

To my Mother

"... Veduto, dico, questo cascai in opinione che se si levasse totalmente la resistenza del mezzo tutte le materie descenderebbero con eguali velocita."

"... Having observed this I came to the conclusion that, if one could totally remove the resistance of the medium, all substances would fall at equal speeds."

– Galileo Galilei
(Discorsi e dimostrazioni matematiche, intorno à due nuove scienze, Leiden 1638)

"This quantity that I mean hereafter under the name of ... mass ... is known by the weight ... for it is proportional to the weight as I have found by experiments on pendulums, very accurately made ..."

– Sir Isaac Newton
(Principia 1687)

"The ratio of the masses of two bodies is defined in two ways which differ from each other fundamentally ... as the reciprocal ratio of the accelerations which the same motive force imparts to them (inert mass) ... as the ratio of the forces which act upon them in the same gravitational field (gravitational mass). The equality of these two masses, so differently defined, is a fact which is confirmed by experiments ...

The possibility of explaining the numerical equality of inertia and gravitation by the unity of their nature, gives to the general theory of ralativity, according to my conviction, such a superiority over the conception of classical mechanics ..."

– Albert Einstein
(The Meaning of Relativity, Princeton)

Contents

Acknowledgements

First of all, I would like to thank my supervisor, Prof. Anna M. Nobili, for giving me the opportunity to work in the GGG group. It was a great pleasure and experience working with her.

I am grateful to Dr. Raffaello Pegna who taught me a lot about the experimental techniques involved in the GGG project with patience and kindness. I thank him for his mentorship and friendship.

I thank Dr. Gian Luca Comandi and Dr. Andrea De Michele for the help they give me whenever I asked.

I thank Dr Donato Bramanti and Prof. Erseo Polacco for the great opportuniuty I had to learn from their research experience.

I thank Dr. Rajalakshmi, from India, for her constant encouragement and support.

Finally, my sincere thanks to Prof. Francesco Pegoraro for his help and kindness during the three years of my PhD program, to Prof. Nicolò Beverini for his suggestions and help during my thesis work and to Prof. Francesco Fuso for helping me with the PhD courses I took.

Introduction

The Universality of Free Fall (UFF), whereby in a gravitational field all bodies fall with the same acceleration regardless of their mass and composition, is an experimental fact that was assumed by Einstein as a "Principle" – the (Weak) Equivalence Principle – at the basis of the General Theory of Relativity.

UFF has been confirmed by experiments to about 10^{-12} in the field of the Sun and to about 10^{-13} in the field of the Earth (see [1], [2], and Table 3 in [3]). In these experiments test masses of different composition are suspended on slowly rotating torsion balances at room temperature. By laser ranging to the Moon (LLR) it has also been found that the Earth and the Moon fall with the same acceleration in the field of the Sun to about 10^{-13} [4].

The main advantage of testing the weak Equivalence Principle in low orbit around the Earth is the much stronger driving acceleration acting on the proof masses as compared to the case in which they are suspended on ground (by about 3 orders of magnitude). Additional very important advantages are weightlessness and isolation of the system in space. The GG satellite has been designed to exploit all these advantages and perform a test of the weak Equivalence Principle/UFF to 10^{-17}, with an improvement by 4 orders of magnitude (see [5], [6]). Though no precise target is available on the level at which a violation should be expected, GG would explore very deeply a totally new domain of physics where chances for a major discovery are high.

The instrument to fly in GG is a differential accelerometer with two concentric test cylinders weakly coupled in the plane perpendicular to the symmetry axis and rotating around it in supercritical regime (i.e. faster than the natural coupling frequency), the purpose of a rapid rotation being that of up-converting the low frequency of the signal – which is the frequency at which the satellite orbits around the Earth – to a much higher frequency in order to reduce electronic, mechanical and thermal noise [7].

GGG ("GG on Ground") is a ground version of the GG sensor instrument which shares its key dynamical features and can therefore be used to test its validity. GGG is presented in Ch. 2 and Ch. 3.

Noise sources typical of the ground environment – and not present in space – need to be made sufficiently small for the GGG sensitivity to be relevant for the space experiment. The most relevant noise sources are tilts and horizontal accelerations due to microseismicity of the local terrain. The GGG rotating shaft is also subject to tilts because of irregularities in the ball bearings which hold it. This Thesis deals with a new set-up of the GGG experiment in which tilt and horizontal acceleration noise at low frequencies is reduced passively by means of 2D laminar joints (see Ch. 4).

We have developed ways of measuring the elastic constant and the performance of the joints by designing and setting up specific apparata, as well as with the GGG full assembly. We have provided evidence that a rotating 2D monolithic joint placed below the ball bearings is very effective in reducing low frequency tilt noise. As a result, a long duration experimental run (by about one month) has shown an improved sensitivity to differential accelerations between the test masses at the low frequencies of interest (Ch. 6). Finally, we have validated a 2D joint with a new geometrical design of the flexures whose improved elastic properties provide on one side a more effective tilt attenuation and on the other a lower natural coupling frequency, hence higher sensitivity (Ch. 5). These are important steps towards reaching a level of ground noise in GGG which brings its sensitivity at low frequencies close to the target sensitivity of GG in space, once accounted for the much weaker coupling of the test masses which is possible only in weightlessness conditions.

References

[1] S. Baeßler *et. al.,* Phys. Rev. Lett. 83, 3585 (1999)

[2] S. Schlamminger *et. al.,* Phys. Rev. Lett. 100, 041101 (2008)

[3] T. D. Wagner *et. al.,* Class. Quantum Grav. 29, 184002 (2012)

[4] J. G. Williams, S. G. Turyshev & D. H. Boggs, Phys. Rev. Lett. 93, 261101 (2004)

[5] Nobili *et al.,* Class. Quantum Grav., 29 184011 (2012)

[6] GG Project Website *http://eotvos.dm.unipi.it*

[7] R. Pegna *et al.*, Phys. Rev. Lett. 107, 200801 (2011)

Chapter 1

Scientific motivation and physics background

1.1 Scientific relevance of the Universality of Free Fall and the Weak Equivalence Principle

Einstein's theory of General Relativity is at present the best theory of gravity. It is based on the assumption that the gravitational force is composition independent, hence that all masses are equally accelerated in the gravitational field of a source body. This is known as the Universality of Free Fall (UFF) and it was first tested by Galileo around 1600.

Newton obtained UFF as a consequence of his mechanics laws and his formulation of the gravitational force under the assumption that the inertial and gravitational mass are equivalent, which he verified experimentally with pendulum experiments similar to those reported by Galileo. This "principle of equivalence" became the basis of classical mechanics. It is now known as the "Weak Equivalence Principle" (WEP) in order to distinguish it from the more general "Einstein Equivalence Principle" (EEP) which assumes the WEP and led Einstein to the formulation of General Relativity in 1915-16. General Relativity requires the WEP/UFF to be valid and Einstein relied on the experimental evidence provided in the same years by Roland von Eötvös and his group in a series of experiments using very sensitive torsion balances that they had originally developed for geophysical purposes [1]. They managed to prove UFF/WEP to the remarkable level of about 10^{-8}; Einstein was aware of these experimental results and therefore regarded General Relativity to be based on very solid foundations.

With the space age General Relativity was put to stringent test in the Solar System under weak-field conditions. More recently it has also been tested in strong-field regime by timing the double pulsar, a unique binary system in which both neutron stars are detectable as radio pulsars providing an ideal testbed for General Relativity[2]. So far all these tests have been successful, yet all attempts at merging gravity with the other forces of nature have failed and most of the mass of the universe is unexplained.

Solar system and double pulsar tests concern the experimental consequences of General Relativity while tests of UFF/WEP concern its foundations. They are therefore expected to have a stronger probing power. Should General Relativity break down at some point, it is likely that such a breakdown will be detected by tests of UFF/WEP. This is why UFF/WEP experiments are worth pushing to better and better accuracy whenever possible.

They belong to the category of small experiments with the potentiality for a major discovery.

1.2 State of the art

After the remarkable and systematic experiments performed by the Eötvös's group at the beginning of 1900, UFF/WEP tests resumed only in the 1960s and early 1970s when an improvement by 3-4 orders of magnitude became possible thanks to the idea of Robert Dicke and his students of considering the Sun as the source body and rather than the Earth and thus exploit the diurnal rotation of the Earth itself to modulate the violation signal. Despite the very slow frequency, this modulation made it possible to achieve 10^{-11}[3] and a few years later 10^{-12} [4].

In 1986 the reanalysis of the Eötvös experiment by Fischbach and collaborators suggested the possible existence of a fifth force [5] and focused the attention of experimental physicists all over the world on the need to perform more sensitive tests of the universality of free fall and the weak equivalence principle. Though the existence of a 5th force was later ruled out, the paper pointed out the importance of testing the foundations of gravity and motivated many research groups worldwide. The most successful experimental results were obtained by the Eöt-Wash group, at the University of Washington, Seattle who used rotating torsion balances in order to modulate the signal at a frequency much faster than the diurnal rotation and at the experimentalist's choice. They confirmed 10^{-12} in the field of the Sun and improved to 10^{-13} in the field of the Earth (see [6], [7], [8]).

The laser reflectors left on the surface of the Moon by American and Russian astronauts has allowed laser ranging to the Moon, yielding a very precise knowledge of its motion. Almost 40 years of lunar laser ranging data have shown that the Earth and the Moon are equally accelerated by the Sun to 10^{-13} ([9], [10]).

1.3 Advantages of space and the GG project

Tests of the Weak Equivalence Principle with rotating torsion balances have reached the thermal noise limit ([11]). Laser ranging technology and physical modeling of the motion of the Moon is being improved [12], but testing UFF with absolute distance measurements from ground suffers fundamental limitations [13]. In both cases the scientists involved are trying to improve the current results by one order of magnitude, but a more significant improvement is out of reach.

A major improvement is possible by performing a torsion balance type of experiment in space inside a spacecraft orbiting the Earth at low altitude. In this case the driving signal from the Earth is about 3 orders of magnitude stronger than it is on ground based torsion balances. In addition, absence of weight allows much weaker suspensions than on ground – hence higher sensitivity – and the satellite housing the apparatus is an isolated system. An improvement by four orders of magnitude is possible provided that the flying instrument is specifically designed to fully exploit all advantages of space.

The proposed GG ("Galileo Galilei") satellite experiments aims at reaching 10^{-17} in the field of the Earth (4 orders of magnitude improvement). It exploits the system isolation by choosing a cylindrical symmetry. Rapid rotation about the symmetry axis provides high frequency modulation of the signal as well as one-axis passive stabilization of the spacecraft. The concentric test cylinders are coupled by very weak mechanical suspensions which provide passive electric grounding. They are free to move in 2D (in the plane perpendicular to the spin/symmetry axis) which allows rotation in supercritical regime (i.e. at frequency much faster than their natural coupling frequency) and self centering by physical laws. Rapid rotation reduces electronic, mechanical and thermal noise ([14], [15]. Finally, the two degrees of freedom of the GG instrument make it possible to fully test it on ground.

On a similar low altitude Earth orbit but with a more conventional instrument the μSCOPE experiment aims at 10^{-15} (2 orders of magnitude improvement). Its slow rotation and higher thermal noise make it impossible to aim at a better target [15]. The μSCOPE satellite is under construction by the French space agency CNES [16].

References

[1] R. V. Eötvös, D. Pekar, E. Fekete, Ann. Phys. 68, 1166 (1922)

[2] M. Kramer *et al.,* Science 314, 97 (2006)

[3] P. G. Roll, R. Krotkov, R. H. Dicke, Ann. Phys. 26, 442-517 (1964)

[4] V. B. Braginsky, V. I. Panov, Sov. Phys. JEPT 34, 463-466 (1972)

[5] E. Fischbach *et al.,* Phys. Rev. Lett., 56, 3 (1986)

[6] S. Baeßler *et. al.,* Phys. Rev. Lett. 83, 3585 (1999)

[7] S. Schlamminger *et. al.,* Phys. Rev. Lett. 100, 041101 (2008)

[8] T. D. Wagner *et. al.,* Class. Quantum Grav. 29, 184002 (2012)

[9] J. G. Williams, S. G. Turyshev & D. H. Boggs, Phys. Rev. Lett. 93, 261101 (2004)

[10] J. Mueller*et. al.,* Class. Quantum Grav. 29, 184006 (2012)

[11] E. G. Adelberger *et al.,* Progress in Particle and Nuclear Physics 62, 102 (2009)

[12] T. W. Murphy *et al.,* Icarus 211, 1103-1108 (2011)

[13] A. M. Nobili *et al.*, Gen. Rel. Grav. 40, 1533-1554 (2008)

[14] GG Project Website *http://eotvos.dm.unipi.it*

[15] Nobili *et al.,* Class. Quantum Grav., 29 184011 (2012)

[16] μSCOPE Website *http://www.cnes.fr/web/CNES-en/2847-microscope.php*

Chapter 2

Basic features of the GGG prototype in the lab

2.1 GG and GGG accelerometer design

As discussed in [1], the key feature of the accelerometer designed for testing the Equivalence Principle with the GG satellite is that the two concentric test cylinders (made of different materials) are coupled so as to be sensitive to differential accelerations in both directions of the plane perpendicular to the symmetry axis, i.e. they form a 2D differential accelerometer. This GG accelerometer at 0-g is designed to detect a relative displacement of the two test cylinders of 0.6 pm pointing to the center of mass of the Earth as the satellite orbits around it at the frequency $\nu_{GG} \simeq 1.7 \cdot 10^{-4}$ Hz ($h \simeq 600$ km orbiting altitude). The cylinders being coupled with a natural oscillation period relative to each other of 540 s, this displacement corresponds to a differential acceleration between them of $8 \cdot 10^{-17}\,\mathrm{m\,s^{-2}}$, yielding a test of the universality of free fall to $\eta_{GG} = 8 \cdot 10^{-17}/g(h) \simeq 10^{-17}$ ($g(h) \simeq 8\,\mathrm{m\,s^{-2}}$).

As shown in Fig. 2.1 the GG accelerometer at 0-g can be perfectly symmetric not only around the spin/symmetry axis of the concentric test cylinders but also "top-down" from the center of mass along the axis. The satellite which encloses in a nested configuration the accelerometer co-rotates with it and is isolated in space. There are no "terrain tilts", external torques are small and have negligible effects due to the extremely high rotation energy of the satellite. Because of conservation of angular momentum no motor is needed to maintain rotation after the initial set-up. Therefore there is no motor or bearings noise to affect the shaft and the test masses.

GGG is a prototype of the GG sensor at 1-g which resembles the GG sensor designed for 0-g. This prototype is designed to demonstrate in the horizontal plane of the lab, at the low frequency ν_{GG}, a sensitivity to differential displacements and differential accelerations as close as possible to those expected for GG in space. In order to build on ground a full scale replica of the instrument to fly shown in Fig. 2.1, GGG is made of two concentric hollow cylinders (10 kg each as in the space experiment) weakly coupled in both directions of the horizontal plane by means of a vertical beam -a tube located along the axis of the cylinders that we refer to as the "coupling arm"- and weak laminar joints sensitive in 2D. The coupling arm is suspended at its midpoint from a rotating vertical shaft in the shape of a tube enclosing it. A total of three joints are needed: a central one to suspend the coupling arm from the rotating shaft (this is the pivot point of the balance), and one for each test cylinder to suspend each of them from the top and bottom end of the vertical coupling arm. They are manufactured in CuBe (for high mechanical quality); their lamellae (two in each direction of the plane) are thin for softness in response to forces in the plane, and wide to ensure sufficient load resistance in the axial direction against local gravity. Thus, the GGG differential accelerometer is in essence a beam balance with two peculiar features which distinguish it from ordinary beam balances: the beam is vertical rather than horizontal and – more importantly – the two masses of the balance are concentric–as required in space to reduce tidal effects. We refer to the dynamical system formed by the two cylinders with the coupling arm and the 3 laminar joints as the "GGG balance".

The relative displacements between the centers of mass of the two cylinders are read by 2 capacitance plates located in between them and with the same cylindrical symmetry at 90° from each other; 2 plates at 180° from each other form 1 capacitance bridge in that direction, so that we have one bridge in each

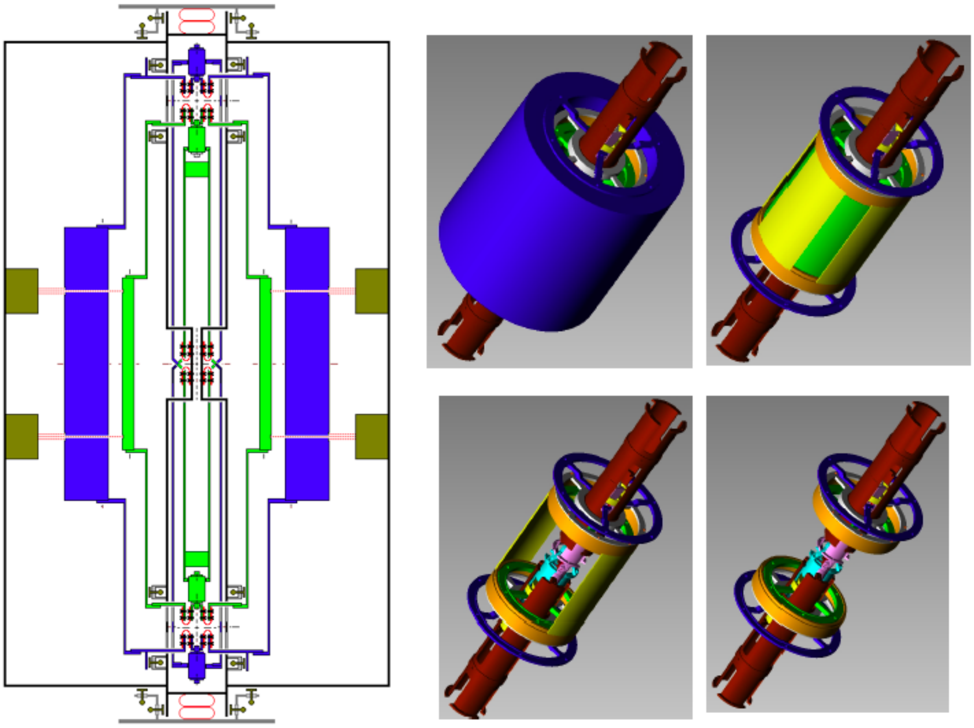

Figure 2.1: The GG sensor made of 2 coaxial concentric test cylinders (in green and blue) spinning around the symmetry axis and weakly coupled to form a beam balance with the beam (coupling arm) along the spin/symmetry axis sensitive to differential forces in the plane perpendicular to it. *Top*: Section along the spin axis of the GG sensor/balance. In addition to the test cylinders at the center it shows the enclosing PGB (an intermediate stage also of cylindrical symmetry) with the springs which connect it to the spacecraft outer shell (not shown). The balance is connected to the PGB shaft from its pivot at the center. All weak connections are U-shaped thin flexures manufatured in CuBe. The masses of the test cylinders are 10 kg each and the diameter of the outer (blue) one is 0.26 m. Due to the complete symmetry of the system the centers of mass of the test cylinders are co-centered at the pivot point of the balance. *Bottom*: Components of the sensor from the outside in. The blue and green cylinders are the test masses; the yellow plates are the capacitance bridge plates located halfway in between the test cylinders to measure their relative displacements along the two orthogonal directions of the plane perpendicular to the symmetry axis. The brown central tube is the PGB shaft from which, at its center is suspended (and pivoted) the balance.

direction of the sensitive plane. They are similar to the plates used in GG in between its test cylinders. In order to be sensitive only to differential effects between the cylinders–which is referred to as “perfect common mode rejection”–the two plates of each bridge should be located perfectly halfway in between the test cylinders. We have manufactured them to be nominally centered, and assembled all plates together, to form what we refer to as “the capacitance cage”; the plates of the cage are not intended to be dismantled individually (which would spoil the manufacture precision).

Detection of very small signals at very low frequency signals is known to be difficult. Difficulties are mitigated by up-converting the low frequency signals to higher frequency (the higher the better) since at high frequencies electronic, mechanical and thermal noise are known to be smaller. Up-conversion of low frequency signals to higher frequency is typically obtained by rotating the apparatus. The fact that the GGG accelerometer has 2 degrees of freedom is crucial to allow rapid rotation around the symmetry axis because, rapid rotation is impossible for an accelerometer with one sensitive axis only. Like in space, rotation occurs around the symmetry axis of the cylinders, the instrument can measure differential accelerations acting between the cylinders in the horizontal plane at very low frequencies and up-convert them to its (much higher) rotation frequency. The rotation frequency is chosen to be higher than the natural coupling frequency of the test bodies so that, like in the space experiment, their centers of mass auto-center on each other in the sensitive plane thus reducing offset errors due to manufacture and assembling. In rotordynamics this is referred to as rotation in supercritical regime.

The GGG instrument up to the top of the shaft is shown in Fig. 2.2 (balance only, i.e. test cylinders plus the coupling arm with the three laminar joints inside it and the capacitance plates of the read-out connected to it), Fig. 2.3 (shaft, up to its top, with the capacitance plates of the read-out connected to it) and Fig. 2.4 (the coupling arm of the balance is inserted inside shaft tube and connected to it through its central joint, thus assembling the full system up to the top of the shaft, to is inserted inside a matched set of ball bearings and set into rotation - ball bearings and other top parts not shown). Figs. 2.2 , 2.3 and 2.4 are taken from the actual construction drawings of the instrument. The GGG prototype in the lab is shown in Fig. 2.5. However, the essence of its dynamical structure is shown in Fig. 2.6, which shows the shaft and the coupling arm tilted from the local vertical by the angles θ_{shaft} and θ_{ca} respectively (both angles are exaggerated for demonstration purposes).

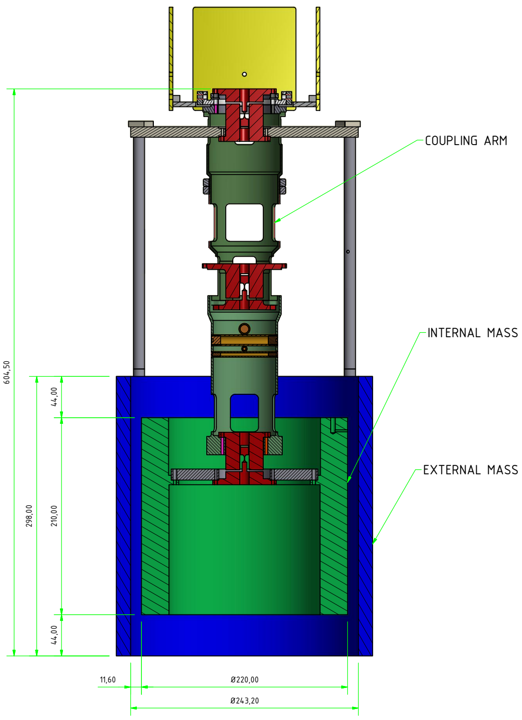

Figure 2.2: Section along the vertical axis of the GGG balance showing the concentric test cylinders with the vertical arm (the coupling arm, in dark green) which couples them through two laminar joints each one sensitive in both directions of the plane, shown in reddish/brown at the top and bottom of the arm. The outer (in blue) cylinder is suspended from the top joint, the inner one (in green) is suspended from the bottom joint. A third similar 2D joint located at the center of the coupling arm suspends the whole balance from a shaft enclosing the coupling arm (not shown here; see next two figures). Its center of oscillation is the pivot point of the balance. All 3 joints are manufactured in CuBe for best mechanical quality. In each joint the width of the lamellae ensures the suspension of the test cylinders ($\simeq$ 10 kg) each against local gravity; compatible with the previous need, the small thickness of the lamellae provides a weak elastic constant in each direction of the horizontal plane of the balance.

Being formed by 3 bodies (the 2 cylinders plus the coupling arm) weakly coupled in the plane, the GGG balance has 3 natural frequencies (or normal modes) in each direction of the plane. The lowest and most relevant one is the differential frequency of oscillation of the test cylinders relative to each other ν_d, with differential period $T_d = 1/\nu_d$. From Fig. 2.6 we can write an analytical formula (which has been found to be in very good agreement with numerical model and experimental results) for the natural period of oscillation T_d of the test cylinders relative to each other in the horizontal plane and is given by

$$T_d^2 = 4\pi^2 \frac{M_t L_t^2 + M_b L_b^2 + m_r \ell_r^2}{k_t + k_c + k_b - M_t g L_t + M_b g L_b - m_r g \ell_r} \tag{2.1}$$

where all symbols are shown in Fig. 2.6. We add that $M_t \simeq M_b \simeq M \simeq 10\,\mathrm{kg}$, $L_t \simeq L_b \simeq L \simeq 0.18\,\mathrm{m}$ and $m_r \ll M$, $\ell_r \ll L$. In these conditions the denominator of (2.1) is essentially $k_t + k_c + k_b - m_r g \ell_r$, and therefore the small regulating body m_r can be adjusted (by changing its mass and its distance from the pivot point of the balance) so as to make the denominator smaller and the differential period longer, hence the balance more sensitive (see below). The smaller the differential frequency (i.e. the longer the differential period), the more sensitive the balance is to differential accelerations acting in between the test

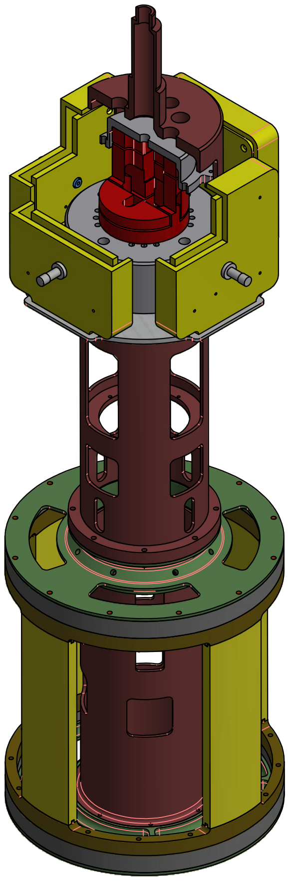

Figure 2.3: The GGG shaft (dark brown tube). Its spindle at the top is inserted inside a matched set of ball bearings (not shown) and set in rotation (motor and relevant components not shown). In the lower part we see 4 capacitance plates (in yellow) rigidly connected to the shaft tube to form –once the full system is assembled, as shown in next figure– 2 capacitance bridges in between the test cylinders. A cut away at the top of the shaft below the spindle shows (in reddish/brown) a 2D weak joint conceptually similar to the balance 2D joints shown in Fig. 2.2 whose purpose is to provide attenuation of low frequency tilts. At the top, a cut-away also shows 4 capacitance plates (in yellow) which are part of an additional read-out to provide the differential displacemnets of the test cylinder after tlits rejection. The coupling arm of the balance shown in Fig. 2.2 fits inside the shaft tube, weakly connected to it through the central joint of the coupling arm, as shown in the assembled system of Fig. 2.4.

cylinders, since $\Delta a = (2\pi\nu_d)^2 \Delta r$ (if Δr is the relative displacement in response to the differential acceleration Δa and ν_d is the natural differential frequency of oscillation of the test masses relative to each other). A differential period twice as long makes the displacement in response to the same differential acceleration four times larger; similarly, the capability of detecting relative displacements twice as small makes the instrument four times as sensitive to differential accelerations. Note that although the numerator (2.1) too contains the regulating mass and its arm, it is essentially unaffected by them since its value is $\simeq 2ML^2$.

Note that though gravity may contribute to weakening the mechanical coupling of the test masses in the sensitive plane it does not affect their relative motion because they are arranged as a balance (while a single pendulum would have a preferential equilibrium position dominated by local gravity); thus, their dynamics has the same features as in space, namely 2 degrees of freedom and rotation in supercritical regime. As it is apparent from the sketch of Fig. 2.6, the body suspended from the top of the balance has a destabilizing effect, hence increasing its mass and/or the length of its arm will make the natural period of differential oscillations longer (and so does the regulation mass if located in the position depicted in Fig. 2.6).

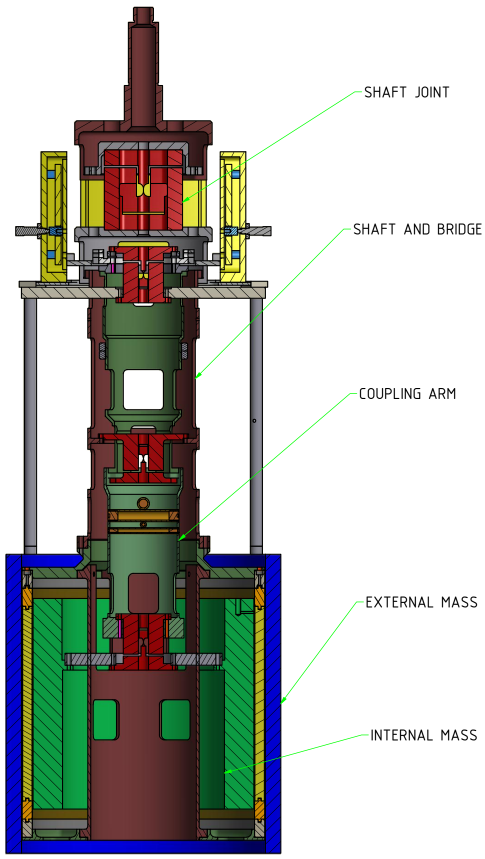

Figure 2.4: Section of the GGG balance, shaft and read-out systems. The top spindle of the shaft is set in rotation (ball bearings, motor and related components not shown); through the 2D weak central joint rotation is transmitted from the shaft to the coupling arm and, through the 2D joint at its top to the outer test cylinder (in blue), and through the 2D joint at its bottom to the inner test cylinder (in green). The oscillation center of the central joint is the pivot point of the balance.

Figure 2.5: GGG prototype in the lab

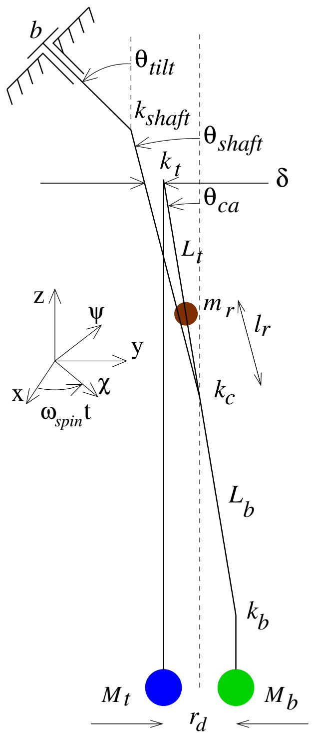

Figure 2.6: Schematic dynamical structure of the GGG rotating balance/differential accelerometer. $M_t \simeq M_b \equiv M \simeq 10\,\mathrm{kg}$ are the masses of test cylinders suspended from the top (the blue one) and from the bottom (the green one) of the coupling arm. They are the outer and inner test cylinder respectively in Fig. 2.2, with the same color code. $L_t \simeq L_b \equiv L$ are the lengths of the top and bottom parts of the coupling arm. k_t, k_c, k_b are the elastic constants (in Nm/rad) along, each direction of the horizontal plane, of the top, central and bottom 2D joints respectively as shown in Fig. 2.2. $m_r \ll M$ is the mass of a small regulating mass located at an arm length ℓ_r above the pivot point of the balance. The top of the shaft is inserted in the bearings b which allow it to rotate. It is shown to be tilted by an angle θ_{tilt} from the direction of the local vertical. On the shaft, somewhat below the bearings, is inserted a 2D laminar joint similar in principle to those on the coupling, with elastic constant k_{shaft} in each direction of the plane with the purpose of attenuating low frequency tilts, so that $\theta_{shaft} < \theta_{tilt}$ is the tilt angle of the shaft after attenuation. Finally, the coupling arm being weakly suspended from the shaft through the central joint k_c will be tilted by $\theta_{ca} < \theta_{shaft}$. All tilt angles are highly exaggerated for demonstration purposes; in reality they are extremely small. The relative displacement between the centers of mass of the test cylinder is indicated as r_d, while the relative displacement between the top of the coupling arm and the shaft is indicated as δ; two different capacitance read-outs allow them to be read independently. r_d is read by the capacitance bridges in between the test cylinders (as in GG), while δ is read by the capacitance bridges shown at the top of Fig. 2.4. The small sketch on the left shows that xyz is the reference frame fixed in lab while $\chi\psi z$ is the one rotating with the GGG shaft at angular velocity ω_{spin}.

2.2 Equations of motion and frequencies of interest

The GG and GGG sensor is a rotating 2D oscillator as shown in Fig. 2.7 whose losses are dominated by internal (or structural) damping in the mechanical suspensions.

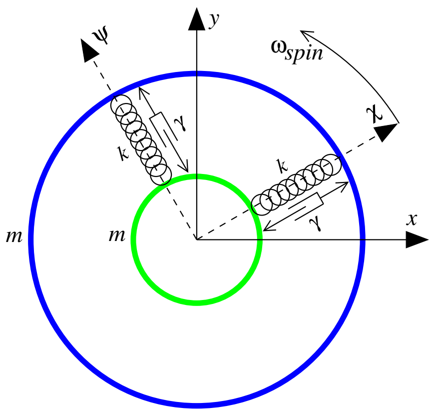

Figure 2.7: Sketch of the 2D rotating oscillator. The proof masses are concentric and rotate–together with the springs–at angular velocity ω_{spin}. They are assumed for the moment as perfectly centered on the rotation axis. The springs are modeled as ideal springs of elastic constant k; to each spring is associated an ideal noiseless damper γ. (x, y) is the inertial frame; (χ, ψ) is the rotating one.

The equations of motion of 2D rotating oscillators as in Fig. 2.7 in which two concentric coaxial test cylinders are weakly coupled with elastic constant k in each direction of the plane perpendicular to the symmetry axis and rotate around it with the angular velocity ω_{spin} can be written in the inertial frame as (see e.g. [2]):

$$\mu\ddot{\vec{r}} + \gamma_{\omega_{spin}}(\dot{\vec{r}} - \vec{\omega}_{spin} \times \vec{r}) + k\vec{r} = \vec{F} \tag{2.2}$$

where $\gamma_{\omega_{spin}}$ is the damping coefficient of the oscillator rotating at ω_{spin}, which is very small; $\vec{F}$ is the signal force whose frequency is so small compared to both ω_{spin} and ω_n that we assume a constant force for simplicity; μ is the reduced mass ($\mu = m/2$ if the bodies have equal mass m); $\omega_n = \sqrt{k/\mu}$ is the frequency of natural oscillations of the masses relative to each other.

The general solution of the equations of motion in the inertial reference frame for the relative position vector $\vec{r}(t)$ of the test masses with ω_{spin} much higher than both the frequency of the force signal and the natural frequency of the system is given by ([2])

$$\begin{aligned} \vec{r}(t) \simeq & -\vec{\epsilon}(\omega_{spin}t)\left(\frac{\omega_n}{\omega_{spin}}\right)^2 + \frac{\vec{F}}{k} - \phi_{\omega_{spin}}\frac{\vec{\omega}_{spin}}{\omega_{spin}} \times \frac{\vec{F}}{k} \\ & + A_0 e^{\phi_{\omega_{spin}}\omega_n t/2}\begin{pmatrix} \cos(\omega_n t + \varphi_A) \\ \sin(\omega_n t + \varphi_A) \end{pmatrix} + \\ & + B_0 e^{-\phi_{\omega_s}\omega_n t/2}\begin{pmatrix} \cos(-\omega_n t + \varphi_B) \\ \sin(-\omega_n t + \varphi_B) \end{pmatrix} \end{aligned} \tag{2.3}$$

This solution consists of three parts which show the physical properties of the sensor. They are:

- **Self-centering at supercritical speed:** The first part of the solution shows self-centering. In Fig. 2.7 we have shown a 2D rotating oscillator in which the proof masses are perfectly centered on the rotation axis. In reality perfect centering is impossible because of inevitable construction and mounting errors; we represent such manufacturing imperfections by an offset vector $\vec{\epsilon}$ of the reduced mass μ from the rotation axis ($\vec{\epsilon}$ is fixed in the rotating frame) which will give rise to disturbances due to centrifugal forces.

Consider now the GGG accelerometer which is spinning at a frequency higher than its natural differential frequency, namely this frequency is in supercritical regime. In supercritical regime the first important fact is autocentering: the centers of mass of the rotating test cylinders, which are necessarily not coincident because of the above mentioned reasons will be closer to each other than they were by construction, thus reducing disturbances due to centrifugal forces.

This can be shown, for simplicity, in the case of a single rotating test mass whose suspension joint S is offset from the rotation axis by a vector $\vec{\epsilon}$ (by construction) as shown in Fig. 2.8. Note that $\vec{\epsilon}$ is fixed in the rotor itself.

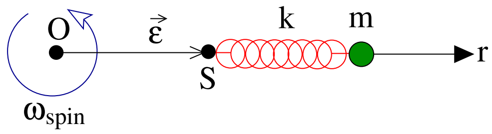

Figure 2.8: O is the center of rotation (the rotation axis is perpendicular to the plane of the drawing and the mass m is not constrained in one direction but can move in the plane). S is the suspension point of the test body, m the location of its center of mass, $\vec{\epsilon}$ the offset vector (fixed in the rotating system) of the suspension point from the center of rotation O. The mass m is subjected to a restoring force towards the suspension point S characterized by the elastic constant k in each direction of the plane.

The equilibrium position of the mass m under the effect of the rotating elastic force and of the centrifugal force will necessarily lie along the direction of the vector $\vec{\epsilon}$, indicated as the axis r. Equilibrium under the forces involved is reached at $\vec{r}_{eq}$ such that:

$$0 = -k(\vec{r}_{eq} - \vec{\epsilon}) + m\omega_{spin}^2 \vec{r}_{eq} \tag{2.4}$$

Introducing the natural frequency $\omega_n = \sqrt{k/m}$, we have the equilibrium condition:

$$\vec{r}_{eq} = \frac{1}{1 - (\omega_{spin}/\omega_n)^2}\vec{\epsilon} \tag{2.5}$$

It shows that for $\omega_{spin} < \omega_n$ (subcritical rotation); $r_{eq} > \epsilon$, which means that equilibrium is reached farther away from the rotation axis than the original offset ϵ (along the same direction of the offset vector); thus, in subcritical regime rotation disturbances increase. Instead, if $\omega_{spin} > \omega_n$, which is the definition of supercritical rotation, at equilibrium it is $|\vec{r}_{eq}| < |\vec{\epsilon}|$, which means that rotation disturbances decrease; moreover, the equilibrium position (fixed on the rotor) is in the opposite direction of the offset vector $\vec{\epsilon}$, which means that it can be reached only if the mass is free to move in the plane perpendicular to the spin axis. If $\omega_{spin} \gg \omega_n$ (rotational frequency much higher than the natural one) (2.5) becomes:

$$\vec{r}_{eq} \simeq -\vec{\epsilon}\left(\frac{\omega_n}{\omega_{spin}}\right)^2 \tag{2.6}$$

which shows the effectiveness of autocentering. Note that in the case of GG and GGG, the two masses weakly coupled in the plane with elastic constant k in each direction the natural frequency is the differential one ω_n with reduced mass μ and the offset vector $\vec{\epsilon}$ is a mutual offset vector resulting from the offsets of the individual masses. The offset vector is anyway not known a prior. This demonstrates that the center of mass of the rotating body reaches equilibrium much closer to the rotation axis than it was by construction, by the factor $(\omega_n/\omega_{spin})^2 \ll 1$. This auto-centering property is what makes fast rotation more advantageous than the slow one. However, the minus sign indicates that for the equilibrium position to be reached the center of mass of the body must be allowed to move in the rotating plane till it sets itself antiparallel to $\vec{\epsilon}$, as required by (2.6): if constrained along a single direction it will not auto-center and be strongly unstable, as it has been known since a long time ([3], Ch. 6). In GGG self-centering has been experimentally demonstrated (see Sec. 3.6 in Ch. 3).

- **Response to the external differential force:** In the presence of an external constant force $\vec{F}$, the equations of motion (2.2) show that (in the inertial frame) the body is displaced to the position:

$$\begin{aligned}\vec{r}_F(t) &= \frac{1}{1 + \frac{\gamma_{\omega_{spin}}^2 \omega_{spin}^2}{k^2}}\left(\frac{\vec{F}_e}{k} - \frac{\gamma_{\omega_{spin}}}{k^2}\vec{\omega}_{spin} \times \vec{F}\right) \\ &\simeq \frac{\vec{F}}{k} - \phi_{\omega_{spin}}\frac{\vec{\omega}_{spin}}{\omega_{spin}} \times \frac{\vec{F}}{k} \simeq \frac{\vec{F}}{k}\end{aligned} \tag{2.7}$$

As we can see, the applied force $\vec{F}$ gives rise to a displacement $\vec{F}/k$ (i.e. inversely proportional to the natural frequency squared) and unaffected by rotation, with an additional effect in the orthogonal direction due to rotation which is negligible because of the very small loss angle $\phi_{\omega_{spin}}$. In the rotating frame of the oscillator this constant displacement observed in the inertial one appears at the rotation frequency $\omega_{spin} \gg \omega_n$, yet it is apparent that no attenuation occurs. This has been proved experimentally (see [4]).

If the same rotating masses are coupled in 1D, the response (maximum displacement along the direction of the force after demodulation to the non rotating frame) is:

$$r_{max} \simeq \frac{\vec{F}}{k}\frac{1}{(\omega_{spin}^2/\omega_n^2) - 1} \tag{2.8}$$

and if $\omega_{spin} \gg \omega_n$

$$r_{max} \simeq \frac{\vec{F}}{k}\frac{\omega_n^2}{\omega_{spin}^2} \ll \frac{\vec{F}}{k} \tag{2.9}$$

So, for an oscillator with 1 degree of freedom, the response to a force acting at frequency $\omega_{spin} \gg \omega_n$ drops off as $(\omega_n/\omega_{spin})^2$. In a nutshell 2D rapid rotation does not affect the signal; in 1D it kills the signal.

- **The phenomenon of forward and backward whirl:** In the assumptions of $\omega_{spin} \gg \omega_n$ and very small internal losses the solution of the homogeneous part of (2.2) is:

$$\begin{aligned} \vec{r}_w(t) \simeq A_0 e^{\phi_{\omega_{spin}}\omega_n t/2} &\begin{pmatrix} \cos(\omega_n t + \varphi_A) \\ \sin(\omega_n t + \varphi_A) \end{pmatrix} + \\ + B_0 e^{-\phi_{\omega_{spin}}\omega_n t/2} &\begin{pmatrix} \cos(-\omega_n t + \varphi_B) \\ \sin(-\omega_n t + \varphi_B) \end{pmatrix} \end{aligned} \tag{2.10}$$

with amplitudes and phases determined by initial conditions. This solution shows that in the inertial reference frame the oscillator performs a combination of a forward and a backward orbital motion–known as *whirl motion*–at the (slow) natural frequency ω_n, and the radii of such orbits are exponentially decaying in the case of the backward whirl and exponentially growing in the case of the forward one. We have written the exponential behavior in terms of the loss angle:

$$\phi_{\omega_{spin}} \simeq \frac{\gamma_{\omega_{spin}}\omega_{spin}}{\mu\omega_n^2} = \frac{\gamma_{\omega_{spin}}\omega_{spin}}{k} \tag{2.11}$$

which is very small because the system has very small losses; hence the forward whirl is a very weak instability. Every natural/whirl period the radius of the forward whirl grows by the fraction $\pi\phi_{\omega_{spin}}$, hence the tangential force which produces the growth is –in modulus– $\phi_{\omega_{spin}} kr$, which is a very small fraction of the elastic force, requiring a correspondingly small force to stabilize it. Its frequency is the natural one and does not interfere with the signal (see [5], [6]). We conclude that whirl motion is a slow instability and can be damped by applying a force along-track, which is much smaller than the elastic force which couples the test masses. Moreover, this force, being along-track does not substantially affect the relative position vector of the test masses in the radial direction, which is the physical quantity of interest. Whirl motions are the only drawback of supercritical rotation.

It is helpful to comment the general solution (2.3) as follows. Assume zero losses and no external force: only the first term is not zero and the solution is the auto-centered position rotating at frequency ω_{spin}; if the force signal $\vec{F}$ is added–still with zero losses–the term $\vec{F}/k$ is not zero and the oscillator is displaced by this vector with auto-centering holding as before; finally, if small losses occur–after the backward whirl has died out, and neglecting the small effect $\propto \phi_{\omega_{spin}}$–the forward whirl slowly grows around the displaced position at frequency ω_n. By controlling this weak instability, rotation (and signal modulation) at a frequency much higher than the natural one are achieved with no signal attenuation and thermal noise reduction.

Having understood the underlying principle and governing dynamics of GG and GGG, now we will briefly discuss the signals of interests both in GG and GGG.

- In order to test the universality of free fall to the level of $\eta_{GG} \simeq 10^{-17}$, the GG sensor is aimed to detect a relative displacement of 0.6 pm between two test cylinders made of different materials being coupled with a natural oscillation period 540 s. The displacement points to the center of mass of the Earth as the satellite orbits around it at the frequency $\nu_{GG} = 1.7 \cdot 10^{-4}$ Hz (given the orbiting altitude $h \simeq 600$ km) .
- The signals of interest for GGG are differential accelerations at very low frequencies: primarily, the frequency of the Equivalence Principle violation signal in the space experiment, which is the orbital frequency of the satellite around the Earth (is $\nu_{GG} \simeq 1.7 \cdot 10^{-4}$ Hz). So GGG must demonstrate in the horizontal plane of the lab, at the frequency ν_{GG}, a sensitivity to differential displacements and differential accelerations as close as possible to those expected for GG in space; secondly, the diurnal frequency at which the Sun moves around the test masses ($\nu_{day} \simeq 1.16 \cdot 10^{-5}$ Hz). Sensitivity to differential accelerations at frequency ν_{GG} tells how far we are from the target sensitivity required in the space experiment, while sensitivity at ν_{day} tells how good is the instrument in testing for an Equivalence Principle violation in the field of the Sun. The smaller the differential acceleration detected, the better the performance of the accelerometer. At the lower diurnal frequency $\nu_{day} \simeq 1.16 \cdot 10^{-5}$ Hz, the sensitivity of GGG to differential accelerations a_{d-day} will express the level at which GGG can test the universality of free fall in the field of the Sun $\eta_{GGG-\odot} = a_{d-day}/a_{\odot-PI}$. $a_{\odot-PI}$ is the common acceleration from the Sun in the horizontal plane of the lab on the GGG test masses located at the latitude of Pisa, whose value changes over the year, reaching a maximum close to $a_{\odot-PI} \simeq 0.0057\,\mathrm{m\,s^{-2}}$ if the experimental run is performed in the months of December and January.

In the case of Earth as a source mass, if two test bodies of different composition are suspended on the ground, each of them reaches equilibrium when the component on the horizontal plane of the centrifugal acceleration due to the diurnal rotation of the Earth

$$a^{\oplus} = 2\omega_{\oplus}^2 R_{\oplus} \sin(2\theta) \tag{2.12}$$

(with $\omega_{\oplus}$ the diurnal angular velocity of the Earth, $R_{\oplus}$ its radius and θ the latitude at which the bodies are located) is balanced by the horizontal component of the local gravitational attraction. This is the equilibrium position of an ordinary plumb line, which does not point to the center of the Earth but is always displaced along the North-South direction towards South. The driving acceleration (2.12) is maximum at 45° latitude where its value is $\simeq 1.7 \cdot 10^{-2}\,\mathrm{m/s^2}$ and it is a DC effect. Since the GGG test bodies are rotors suspended on the Earth and the Earth rotates around its axis, this diurnal rotation gives rise to gyroscopic effects (see Sec. 3.6 of Ch. 3) on the test bodies which result in displacements (different for the two cylinders) in the North-South direction masking a possible violation signal in the field of the Earth. Therefore the GGG accelerometer cannot be used for testing the EP violation due to Earth.

References

[1] R. Pegna, A. M. Nobili, T. R. Saravanan *et al.*, "Attenuation and rejection of vibration noise in the GGG rotating differential accelerometer", in preparation

[2] R. Pegna *et al.*, Phys. Rev. Lett. 107, 200801 (2011)

[3] J. P. Den Hartog, Mechanical Vibrations, Dover Publications, Inc., New York 1985 (First Published in 1934)

[4] A. M. Nobili *et al.*, Class. Quantum Grav. 29, 184011 (2012)

[5] S. H. Crandall, J. Sound Vib. 11(1), 3-18, (1970)

[6] A. M. Nobili *et al.*, Class. Quantum Grav. 16, 1463-1470 (1999)

Chapter 3

The experimental apparatus and its main features

3.1 The vacuum chamber: ad hoc design, instrumentation and thermal control

The design of the vacuum chamber is optimized for hosting the GGG accelerometer and to minimize various disturbances on it. This vacuum chamber consists of a thick stainless steel metal jar (1 m diameter and 1.6 m height) with five glass access windows (Fig. 3.1). Three rigid steel legs at 120° from each other well fixed to the floor, form the basis for this vacuum chamber. Inside the vacuum chamber another three steel legs at 120° from each other with ceramic breaks on top of them are used to connect the bottom of the chamber to the rigid circular plate. The suspended accelerometer is sitting on this plate. The legs with ceramic breaks contribute to thermally decouple the thermal stress coming from the legs into the chamber. The jar can be lifted with the aid of a crane so as to open and close the jar without disturbing the experiment after adjustments and balancing have been applied.

Figure 3.1: The new vacuum chamber designed to host advanced GGG accelerometer and its thermal stabilization

This newly designed vacuum chamber has two features:

- This vacuum chamber has cylindrical symmetry with an axis in the vertical direction exactly like GGG accelerometer sitting inside it.
- This chamber rests on a base frame whose structure is rigid, as a result, the vibrations coming from the terrain and thermally induced expansion/contraction are reduced.

For evacuating the chamber a magnetic suspended turbo pump has been chosen for its low noise performance. And also an ad hoc valve for its smooth and gentle way of operation has been installed to allow us to isolate the chamber momentarily from the rest of the pumping system without disturbing the experiment. The pumping system consists of a turbo molecular pump and a dry scroll pump. Closing the ad hoc valve is sometimes needed; for instance, it was needed at some point to check for leaks. All the electrical feedthroughs are located on the bottom cover to allow the cylindrical body and top lid of the chamber to be lifted to access the experiment without disconnecting all the cables.

Different types of gauges like Bayard-Alpert ionization gauge and Pirani gauge have been mounted on different locations (see Fig. 3.2). Three gauges are mounted on the vacuum system: one on the bottom and another one on the upper part to monitor the pressure inside the chamber; third one mounted on the fore-vacuum line to operate the turbo pump in appropriate conditions. Two gauges on the top and bottom side of the chamber, and another one is mounted at fore-vacuum line so as to switch on the turbo pump in appropriate conditions. These gauges are connected to a multichannel display to monitor the pressure as well as to acquire and save readings on the computer disk for further analysis. The rate of acquisition for the pressure data is 1 Hz, which is the maximum rate available from the product itself and also more than sufficient for our work.

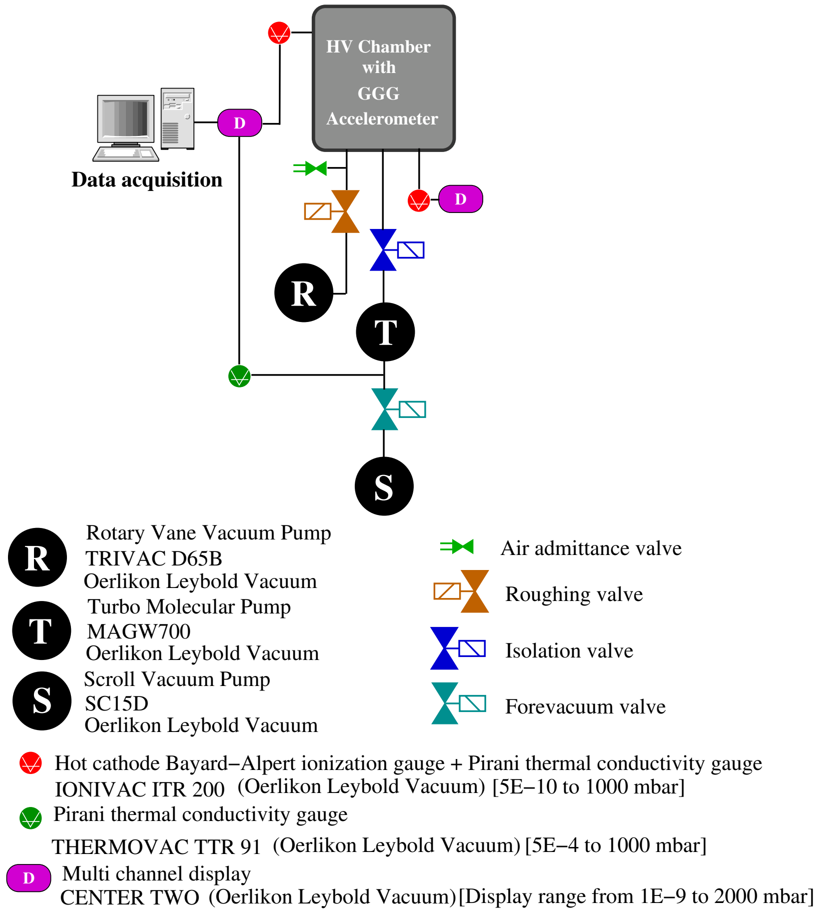

Figure 3.2: Schematics of the GGG vacuum system

The chamber is evacuated as follows:

- A rough vacuum is created by a rotary vane pump, which has a nominal pumping speed of 75 m^3/hr; it can be detached any time from the system by a roughing valve.
- During this time a scroll pump is also switched on, so that it will simultaneously create a rough vacuum in the turbo line too. We must open the fore-vacuum valve to connect this scroll pump to the turbo. This scroll pump has the pumping speed of 13.6 m^3/hr.
- When the pressure in the chamber as well as in turbo line reaches a rough vacuum of about 1 Pa, the roughing valve is closed so as to disconnect the rotary pump from the chamber.
- Then the ad hoc isolation valve is opened so that the turbo molecular pump is connected to the chamber and the turbo pump is switched on. Then the evacuation of the chamber down to a few 10^{-5} Pa takes its time.

The ultimate pressure of a few 10^{-5} Pa is achieved by this turbo molecular pump but we usually operate the experiment at about 10^{-4} Pa. These operations can be well understood from the schematic of the GGG vacuum system shown in Fig. 3.2. All the components to be mounted inside the chamber are thoroughly cleaned with methanol and acetone. After assembling the whole system He leak check have been performed to suspect for any leaks. Fig. 3.3 shows the results from measurement to check the vacuum level and the leak rate. The rate-of-rise curve shows that the vacuum leak rate is about $1.16 \cdot 10^{-5}$ mbar litre/second, which means that vacuum system is sufficiently tight.

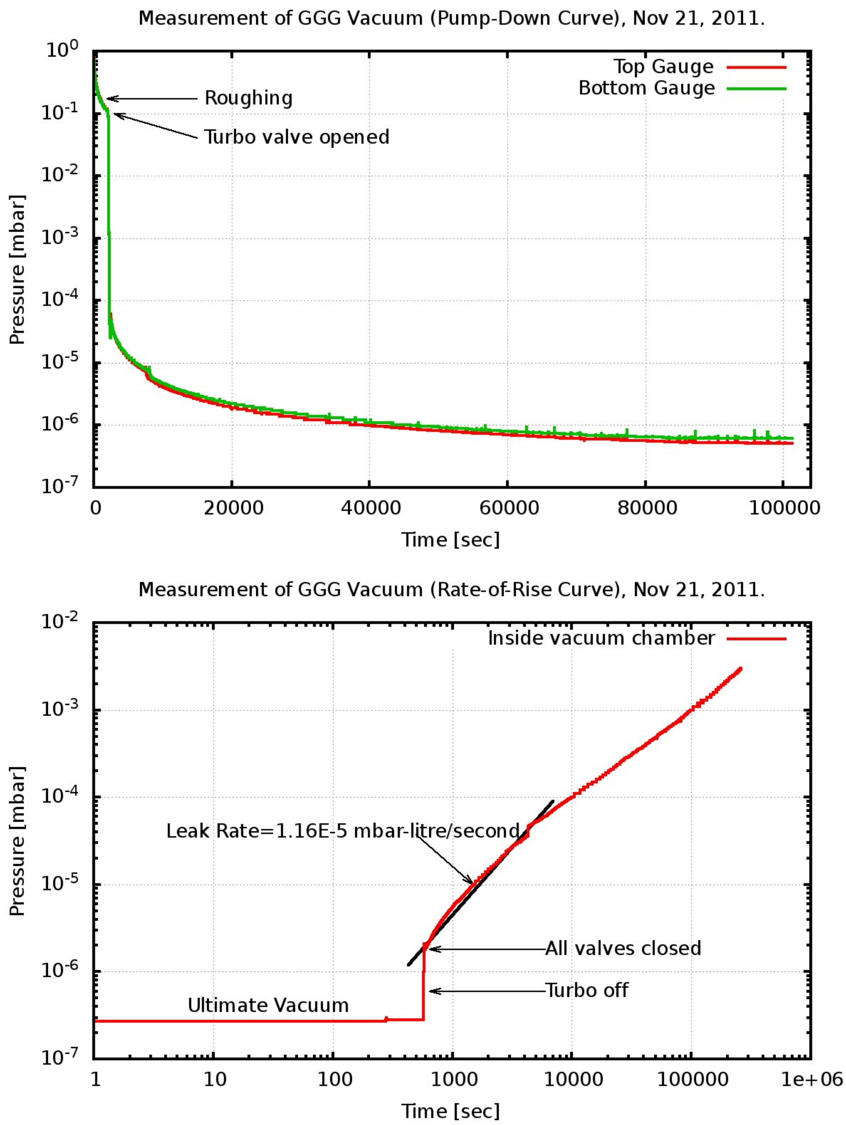

Figure 3.3: GGG vacuum tests

In GGG thermal stabilization of the chamber is necessary to reduce the effect of diurnal and low frequency thermal expansion/contraction effects of the chamber and the entire apparatus on the test masses. Due to the good vacuum and consequent good isolation, it is not wise to use a temperature sensor inside the chamber (e.g. on the steel flange holding the ball bearings) in order to drive the heating (or cooling) of the chamber. A better strategy is to place temperature sensors around the chamber and design the control loop in order to keep the whole surface at the same temperature all the time. To achieve thermal stabilization, the entire vacuum chamber is uniformly coiled outside with a heating wire, since the body of the chamber is stabilized by heating only to about 10°C above the ambient temperature by passing current through this coil. PT-100 sensors are used as temperature sensors. Above that, thermal insulating rubber blanket (Fig. 3.1) is wrapped around the chamber to improve isolation from the outside environment and finally a mylar sheet is wrapped around so that its reflectivity reduces the impact of direct heat by radiation. This temperature control strategy has provided very good results.

The thermal stabilization system is based on the idea that, a Proportional-Integral (PI) algorithm controls the duty cycle of a set of heating resistors thermally coupled to the walls of the vacuum chamber. The temperature sensors (PT-100) are also coupled to the walls of the chamber. Because this system can only heat the chamber, the thermal control set point temperature should be greater than the ambient temperature. The level of thermal stability achieved inside the vacuum chamber housing the GGG experiment and the level of decoupling to 24 hr effects is reported in Fig. 3.4. We have used two PT-100 temperature sensors to carry out this measurement, one outside the chamber to measure the ambient temperature and the other one inside it. FFT of this measurement shows that the 24 hr ambient temperature variations (red line in the plot) are attenuated inside the vacuum chamber (green line in the plot) by two orders of magnitude. We can then state that, within the reached level of 24 hr stabilization, the temperature control system is insensitive to ambient temperature variations.

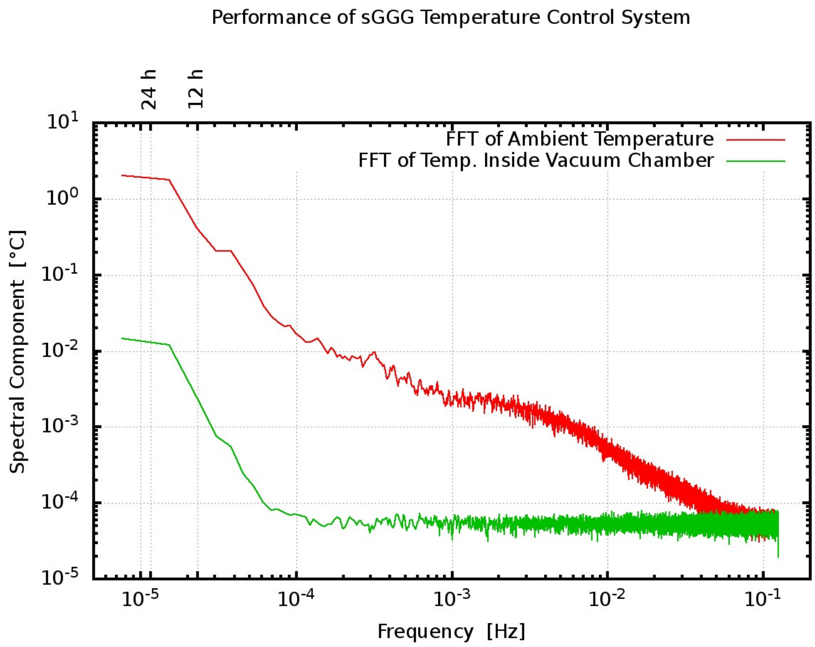

Figure 3.4: Performance of the temperature control system of the GGG experiment. 24 hr ambient temperature variations (red line) are attenuated inside the vacuum chamber (green line) by two orders of magnitude.

3.2 The rotating differential accelerometer and its suspensions

GGG, a rotating suspended differential accelerometer, is a vertical beam balance sensitive to differential accelerations acting in the horizontal plane of the laboratory. It is made of two concentric coaxial test cylinders weakly coupled by a balancing arm suspended at its center from the rotating shaft. Fig. 3.5 shows the schematic of this accelerometer through the spin symmetry axis inside the vacuum chamber. In this section our primary intention is to explain only the basic concept of the GGG mechanical design.

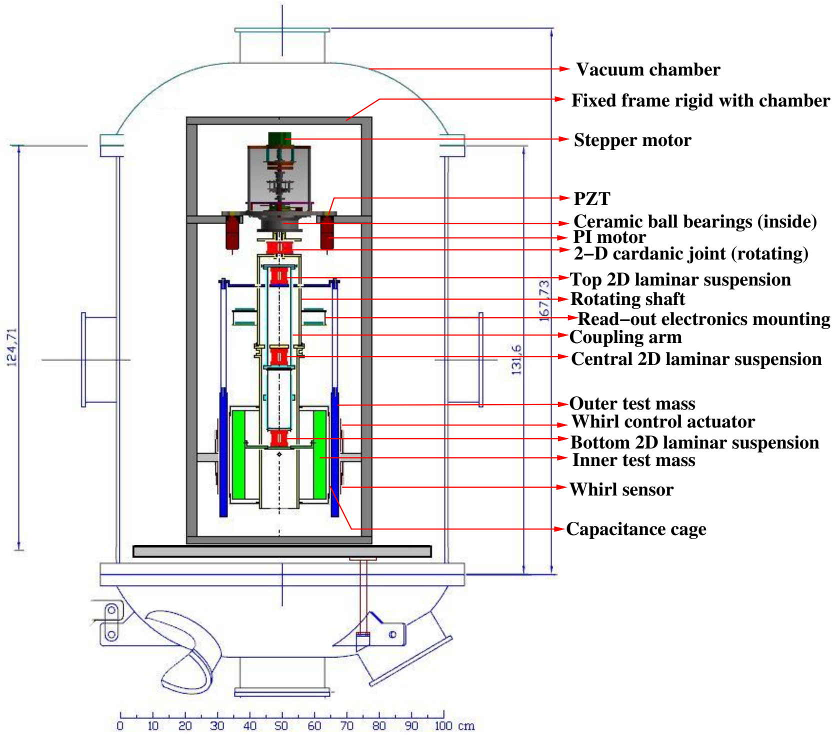

Figure 3.5: Section through the vertical axis of the vacuum chamber and the experimental apparatus mounted inside it.

The fixed frame of the GGG accelerometer hosts and sustains all the weight of the rotating and non-rotating parts of the accelerometer. This frame is rigidly fixed to the base plate of the vacuum chamber and hence the name. It is designed with 4 thick metal bars assembled at 90° from each other rigidly on the bottom base plate of the vacuum chamber. Cross bars interconnect them so as to ensure good rigidity of whole frame. This frame hosts the rotating accelerometer with its non rotating components. The capacitance sensors and actuators for whirl control are rigidly mounted on this frame (see Fig. 3.5) and hence they are not rotating. So totally 8 capacitance plates are placed near the outer surface of the external mass and they are fixed on this fixed frame. One half of them are used as sensors and the other half of them as actuators. The whirl motion and its control scheme is described in detail in Sec. 3.5 of this chapter.

The accelerometer essentially has two parts. A non rotating part (funnel steel flange hosting the ball bearings) and the rotating system with a 2D flexible joint on the shaft plus the rotating accelerometer. This 2D flexible joint has been introduced below the bearings for the following two primary reasons:

- Any diurnal temperature fluctuations may induce a differential thermal expansion/contraction on the 4 long metal bars of the fixed frame. This will give rise to a tilt disturbance on the accelerometer, and hence a differential displacement which will compete with our signal of interest in the laboratory frame (systematic effect). Introducing a passive 2D weak flexible joint below bearing will decouple this effect along with the real terrain tilt.

- It is that $\theta_{tilt} = \theta_{terrain} + \theta_{bearings}$. The first term is as explained above. The second term is the tilt noise due to the bearings used for spinning the accelerometer. It is well known that bearings introduce an inevitable noise due to issues like irregularities of balls, giving rise to tilts of the shaft that should be decoupled. This weak joint below the bearings will do this job effectively. In a nutshell this 2D monolithic flexible joint has been expected to strongly attenuate tilt and horizontal displacement noise introduced by the ball bearings and also expected to reduce the effect of seismic disturbances at low frequencies in the laboratory frame.

This monolithic 2D joint (Fig. 3.6) has been manufactured by electroerosion technique, the same technique and material used to manufacture cardanic joints to couple the test masses. CuBe has been chosen to have better elastic property, monolithic and hence no clamping problem. The angular spring constant in both directions has been measured on-bench and it is about $k_{\theta\chi} \simeq k_{\theta\psi} \simeq 0.17\,\mathrm{Nm/rad}$. So it is expected that the tilt attenuation factor is about 1000 at the low frequencies of interest.

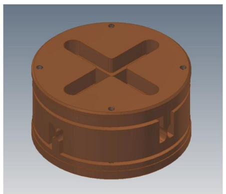

(a)

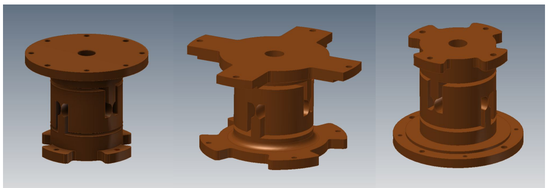

(b) (c) (d)

Figure 3.6: (a, b, c & d) Joint below bearing, top, central and bottom suspensions

The non rotating part contains the main elements for the transmission of rotation, and power to the rotating electronics and rotary optical encoder. These elements are situated above the steel flange, and this steel flange is connected to the fixed frame with the aid of 3 pairs of PZT and PI motors at 120° with each other. This arrangement helps to put the funnel steel flange horizontal. The rotating system contains the vertical balance with capacitance transducers. The rotating shaft is fixed into the non rotating steel flange with the help of matched ball bearings to spin the accelerometer. The issue is that great care should be taken for the connection between the non-rotating part of the accelerometer (funnel steel flange) to the fixed frame through PZT's and PI motors. Otherwise it will create disturbance which will couple to the differential displacements of the test masses. The shaft is set in rotation by a stepper motor through a number of components which will be discussed in detail in the next section of this chapter.

The coupling arm is suspended at its midpoint from the rotating shaft by means of a laminar 2D joint. This is the central suspension which sustains the whole weight of the test masses with the coupling arm. The 3 laminar suspensions (see Fig. 3.6) are designed to be stiff against local gravity in the vertical (axial) direction, and soft in the directions determining the horizontal-sensitivity plane perpendicular to the spin axis. They are carved out of a solid bar of CuBe and properly treated to ensure high quality factor. Fig. 3.7 shows the GGG balance with the inner and outer test cylinder suspended from the shaft through the top and bottom joint respectively. Table 3.1 gives the main characteristics of the balance as well as the four joints.

Table 3.1: (a,b & c): Characteristics of GGG balance, test cylinders and coupling arm (see Fig. 3.7)

Relevant Data of GGG Balance	
L_t	18.3 cm
L_b	18.3 cm
l_r	(changeable)

Dimensions of the GGG Test Cylinders and coupling Arm				
Body	Mass (kg)	Inner Radius (cm)	Outer Radius (cm)	Height (cm)
Inner Cylinder	10	8	10.9	21
Outer Cylinder	10	12.1	13.1	29.8
Balancing Arm	0.5	2.8	3	$L_t + L_b$

Angular Spring Constants of GGG Suspensions			
Suspension	Direction	Theoretical (k_θ) (Ch. 5 (5.1)) (Nm/rad)	Experimental (k_θ) (Nm/rad)
Top	(χ)	0.273	0.26±0.01
	(ψ)	0.273	0.38±0.01
Bottom	(χ)	0.273	0.34±0.01
	(ψ)	0.273	0.33±0.01
Central	(χ)	0.545	0.59±0.01
	(ψ)	0.659	1.14±0.01
Below bearing	(χ, ψ)	0.126	0.17±0.01

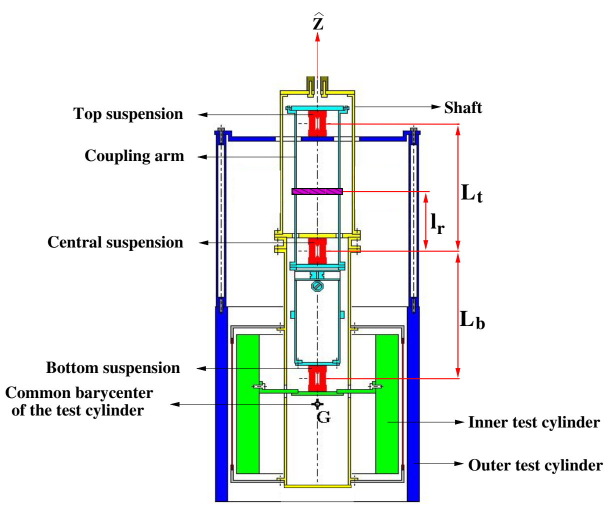

Figure 3.7: Sketch of the GGG balance. The blue and green are the test cylinders coupled by the coupling arm. The coupling arm is connected to the shaft by the central joint. The 3 joints are shown in red. The diameter of the outer test cylinder is 26.2 cm.

3.3 Motor, bearings, power coupling, mechanical coupling and rotation transmission

To spin the GGG rotor we use a 2-phase stepping motor (PK264–E2.OAR11) with a step angle of 1.8° from Oriental Motors. 8 lead wires from this motor are connected in a bipolar mode in series. In this configuration we can obtain maximum holding torque. The step accuracy is of ±3 arc minutes (±0.05°). This stepper motor is driven by a micro stepping motor driver DS1044 from LAM Technologies; it allows us to spin the motor with a resolution of 2000 steps/rev and can be fed with an external clock signal from a precise Rubidium clock. We can program the driver using a USB port connected to the PC. A 10 MHz Rubidium clock signal is fed into the Agilent signal generator as a source signal so as to derive the clock signal for the stepper motor driver from it, taking the Rubidium clock as reference. The motor and the driver are shown in Fig. 3.8.

Figure 3.8: The stepper motor and its driver used to spin the GGG rotor

In order to obtain rotational accuracy, we have carefully selected a set of matched ball bearings (with ceramic balls) suitable for the GGG system in which horizontal load is very small (see Fig. 3.9). The bearings are cleaned to eliminate grease and then lubricated by an oil suitable for vacuum for smooth rotation. Fomblin oil is used for lubrication. We take care of adding some droplets of fomblin oil in the bearings because after some time even this oil evaporates in vacuum; instead, some lubricant is always needed to ensure smoothness and avoid damaging the ceramic balls.

Figure 3.9: The matched set of ceramic ball bearings selected for the GGG rotor

A contactless power coupler has been manufactured in our lab (Fig. 3.10) and is efficiently used to transmit electrical power to the rotating electronics on the GGG rotor (see Fig. 3.11). It works better than sliding contacts used in the past (of various kinds, also with lamellae) because there are no interruptions in power transmission and no dust particles. In essence the power coupler is a contactless electric transformer. Our power coupler has one primary coil, which is not rotating and two secondary coils which are rotating. We use the color code; red for non-rotating parts and blue for rotating parts (see Figs. 3.10 and 3.12). The rotating and non rotating parts are separated by 1 mm gap. The windings are made on plastic substrates within the ferrite cores shown in Fig. 3.10 (EPCOS type). The windings have the characteristics, shown in Table 3.2.

Table 3.2: Characteristics of the power coupler windings

Primary coil	wire diameter 0.85 mm 55 turns
Secondary coil-1	wire diameter 0.85 mm 37 turns (For the provision of +5 V)
Secondary coil-2	wire diameter 0.50 mm 68+68 turns (For the provision of ±12 V)

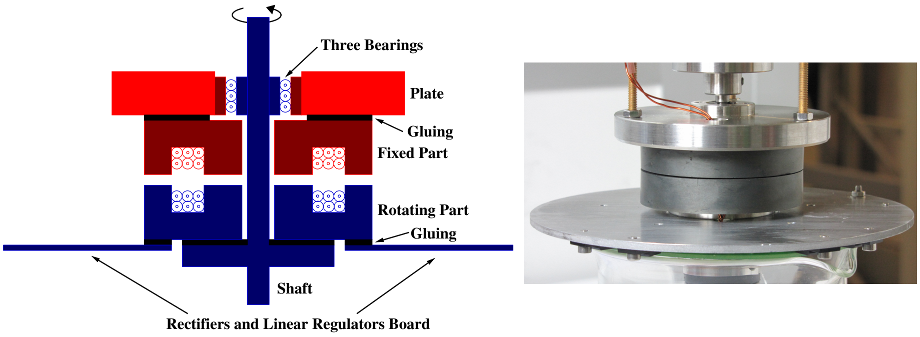

Figure 3.10: Power coupler and a view of the two ferrite cores with windings (both primary and secondary

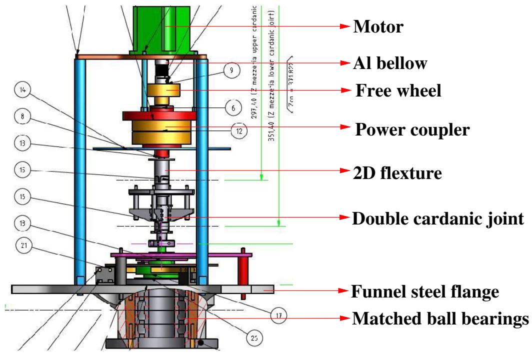

Figure 3.11: (a & b) Upper parts of the GGG apparatus located inside the fixed frame

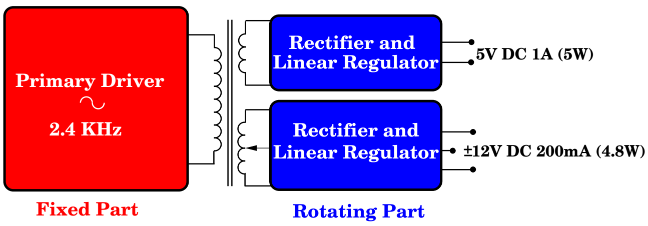

Figure 3.12: Block diagram of the power coupler

Referring to Fig. 3.12, the primary driver is the driver for the primary of the transformer. It consists of a sinusoidal signal generator with frequency 2.4 KHz AC coupled to a power amplifier that is directly connected to the primary coil. 5 V and ±12 V DC voltages at 5 watt and 4.8 watt respectively are obtained by rectification and linear regulation of the secondary coils voltages. The power required for rotating electronics is only a few watts. Fig. 3.10 shows how these primary and secondary coils are mounted on the system. The ferrite cores are glued to their supports. A circular shaped aluminium plate fixed to the rotating coil core is used as a power heat sink for the linear regulators ICs and the rectifiers.

The assembly of the motor, the power coupler and the other components – down to the funnel shaped steel flange inside which are mounted the ball bearings and the shaft spindle – is shown in Fig. 3.11 where all the joints are identified. Among various components a crucial element called free wheel (see Fig. 3.13) is mounted above the power coupler to allow the rotor to spin freely in case of motor failure, so that the weak CuBe suspensions are not damaged.

Figure 3.13: Free wheel to avoid damage to CuBe joints in case of motor failure (mounted above power coupler)

3.4 Capacitance read-out, ADC conversion, optical data transfer and data acquisition

The relative mechanical displacements of the GGG test cylinders in the χ and ψ directions of the plane perpendicular to the spin/symmetry axis z are read by two orthogonal capacitance bridges, rotating with the system. Each bridge is made of two capacitance plates located halfway in between the test cylinders as shown in Fig. 3.14. The read-out has cylindrical symmetry. The four plates which form the two bridges are assembled in a cage not to be ever dismantled, as this would impair the symmetry and construction precision. The gap between each plate and the facing surface of the test cylinder is 1 mm. Parameters of the capacitance transducer are given in Table 3.3.

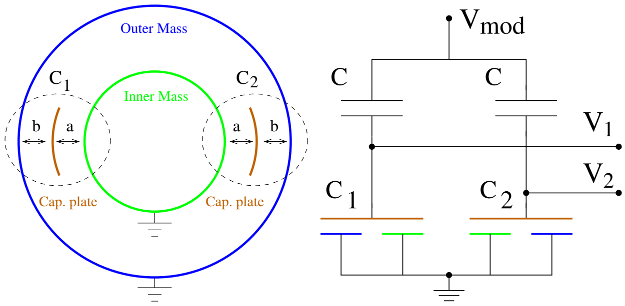

Figure 3.14: Schematic drawing of the two capacitance sensor of the bridge of the GGG read out system for detecting relative displacements of the inner and outer test cylinder with respect to one another. Each capacitor is formed by two surfaces, one for each of the two grounded bodies, and one plate, to which a sinusoidal voltage is applied. The other two capacitors of the bridge are fixed capacitors. Any differential displacement of the test masses with respect to the plates causes a loss of balance of the bridge and therefore an output signal.

Table 3.3: Parameters of the capacitance transducer

Height (h)	Width (w)	Area (S)	d
19.4 cm	6 cm	116.4 cm^2	1 mm
($C_0 = \epsilon_0 S/d \simeq 200$ pF)			

Now we will estimate the signal in the Wheatstone bridge shown in Fig. 3.15. Let C_a and C_b are the capacitances between the isolated rotating capacitive plates and the GGG grounded test masses. If the GGG test masses are displaced by Δx_{dm} as shown in Fig. 3.16 (we do not discuss here the common mode motion and the relative common mode rejection of the capacitive bridge).

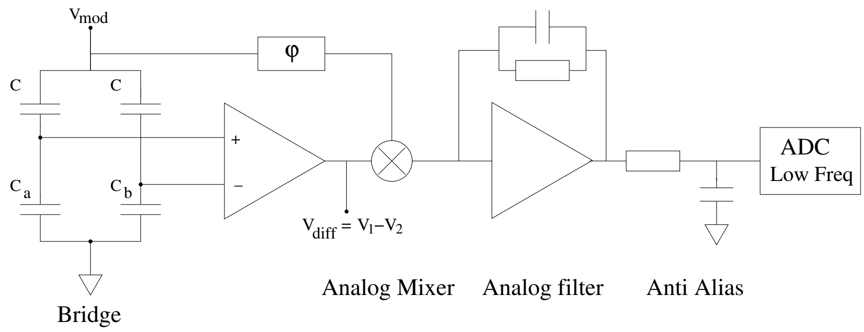

Figure 3.15: Simplified GGG Wheatstone bridge schematics. The first amplifier is a INA111 differential instrumentation amplifier; the mixer is a phase–controlled rectifier using an AD630 demodulator Integrated Circuit (IC); the ADC is an AD7738 24 bits IC. Note that this electronics must rotate with the test cylinders, and therefore needs to be powered from the non rotating frame (see Sec. 3.3).

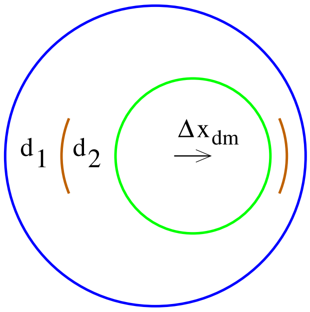

Figure 3.16: In brown color it is illustrated one of the GGG capacitances bridges. The test masses are displaced by Δx_{dm}.

For C_a it holds:

$$
\begin{aligned}
C_a &= \epsilon_0 \frac{S_1}{d_1} + \epsilon_0 \frac{S_2}{d_2} \\
d_1 &= d_2 = \frac{d_0 + \Delta x_{dm}}{2} \\
S_1 &\simeq S_2 \simeq S \\
C_a &= \frac{4\epsilon_0 S}{d_0 + \Delta x_{dm}}
\end{aligned}
\tag{3.1}
$$

Similarly for C_b:

$$
C_b = \frac{4\epsilon_0 S}{d_0 - \Delta x_{dm}} \tag{3.2}
$$

Relative variations are:

$$
\begin{aligned}
\frac{\Delta C_a}{C_a} &= -\frac{\Delta x_{dm}}{d_0} \\
\frac{\Delta C_b}{C_b} &= \frac{\Delta x_{dm}}{d_0}
\end{aligned}
\tag{3.3}
$$

The gain of the bridge itself is:

$$
V_+ - V_- = V_{diff} = V_{mod}\left(\frac{Z_a}{Z_1 + Z_a} - \frac{Z_b}{Z_2 + Z_b}\right) \tag{3.4}
$$

$$
\begin{aligned}
Z_a &= \frac{1}{i\omega_{mod} C_a} = \frac{d_0 + \Delta x_{dm}}{4\epsilon_0 S i\omega_{mod}} \\
Z_b &= \frac{1}{i\omega_{mod} C_b} = \frac{d_0 - \Delta x_{dm}}{4\epsilon_0 S i\omega_{mod}} \\
Z_1 &= Z_2 = \frac{d_0}{4\epsilon_0 S i\omega_{mod}} \\
V_{diff} &= V_{mod}\left(\frac{d_0 + \Delta x_{dm}}{2d_0 + \Delta x_{dm}} - \frac{d_0 - \Delta x_{dm}}{2d_0 - \Delta x_{dm}}\right) = V_{mod}\left(\frac{2\Delta x_{dm} d_0}{4d_0^2 - \Delta x_{dm}^2}\right)
\end{aligned}
\tag{3.5}
$$

For small differential displacements Δx_{dm} we can approximate as:

$$
V_{diff} \simeq V_{mod}\frac{\Delta x_{dm}}{2d_0}; \quad |\Delta x_{dm}| \ll d_0 \tag{3.6}
$$

Fig. 3.17 reports the plot of V_{diff} as a function of Δx_{dm} for $-d_0 < \Delta x_{dm} < d_0$ and $d_0 = 2\,\mathrm{mm}$.

If $V_{mod} = 1\,\mathrm{V}$ then the gain for small test mass differential displacements is:

$$
\frac{V_{diff}}{\Delta x_{dm}} \simeq 250 \frac{\mathrm{nV}}{\mathrm{nm}} \tag{3.7}
$$

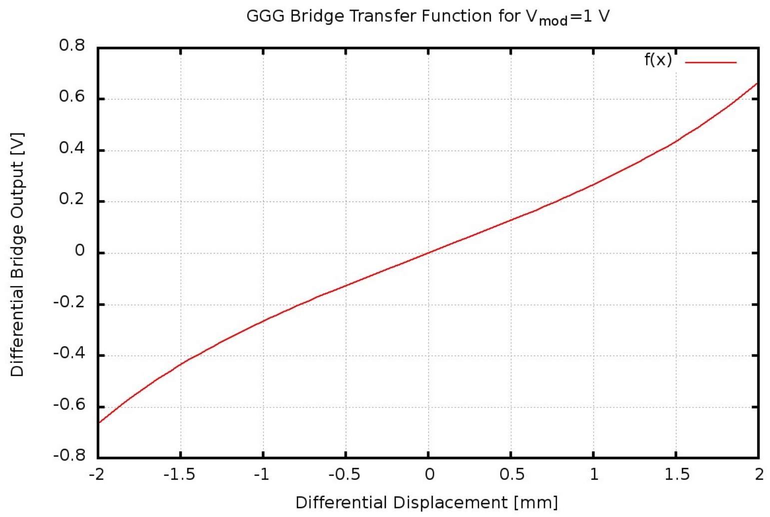

Figure 3.17: Amplitude of the signal of the GGG capacitive bridge as a function of the test masses differential displacement.

Value of capacitances C_a and C_b is about 200 pF and their differential variation due to the differential displacements is:

$$\frac{\Delta(C_b - C_a)}{\Delta x_{dm}} = 2 \cdot 10^{-4} \frac{\mathrm{pF}}{\mathrm{nm}} \tag{3.8}$$

From these relationships it is possible to derive the signal of the bridge and the bridge capacitances differential variation corresponding to a 1 nm differential displacement. With $V_{mod} = 1\,\mathrm{V}$, we have $V_{diff} = 1.25\,\mathrm{mV}$ when $C_b - C_a = 1\,\mathrm{pF}$.

Let's the ADC dynamical range be 2.5 V; dynamical range of the mechanical differential displacement is $-2\,\mathrm{mm} < \Delta\mathrm{x}_{\mathrm{dm}} < 2\,\mathrm{mm}$. The overall gain of the amplifier circuit should then be:

$$\frac{2.5\,\mathrm{V}}{4\,\mathrm{mm}} = \frac{625\,\mathrm{nV}}{\mathrm{nm}} \tag{3.9}$$

The gain of the bridge is $A_{bridge} = 250\,\mathrm{nV/nm}$ so that the gain of the amplifier circuit should be $A_{ampli} = 2.5\,(\mathrm{V/V})$. Requiring to be sensitive at the nm level, the discretization noise σ_{discr} of the ADC should be:

$$\sigma_{discr} = \frac{2.5\,\mathrm{V}}{\sqrt{12} \cdot 2^{N_{bits}}} < 625\,\mathrm{nV} \tag{3.10}$$
$$N_{bits} > 20.14$$

The bandwidth of the amplifier circuit should be limited to $\ll \nu_{samp}/2$ in order to avoid aliasing. Regarding the rotating experiment, the minimum bandwidth required for demodulating to the non-rotating frame the bridge signals is limited to ν_{spin}. It has been chosen to limit the amplifier bandwidth to $\ll \nu_{samp}/2$, this allows the correct sampling of the bridge signals so that a further bandwidth reduction can be obtained by filtering the acquired samples.

The capacitance cage (Fig. 3.18) has been manufactured for the plates to be nominally at exactly the same distance from the inner and outer test cylinder respectively. The better the plates are centered in between the cylinders, the more insensitive the bridge is to their displacements in common mode. Ideally we would like the bridge to be sensitive only to differential displacements of the cylinders relative to each other but in reality this happens only if the plates are centered exactly. Otherwise we have (see Fig. 3.19):

$$\frac{C_1 - C_2}{2C_0} \simeq \frac{a-b}{a^2}\Delta x_{cm} - \frac{1}{a}\Delta x_{dm} \tag{3.11}$$

C_0 is the nominal value of the capacitance of each plate facing one of the test cylinders (about 200 pF) and C_1, C_2 are the capacitances of each plate resulting from the displacements.

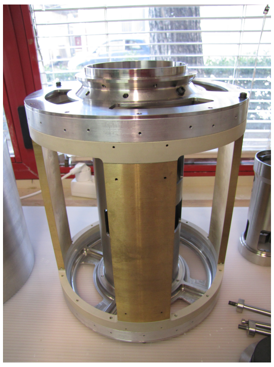

Figure 3.18: Four capacitance plates manufactured from a single brass cylinder, subsequently cut and assembled in a cage, not to be ever dismantled to maintain symmetry and construction precision.

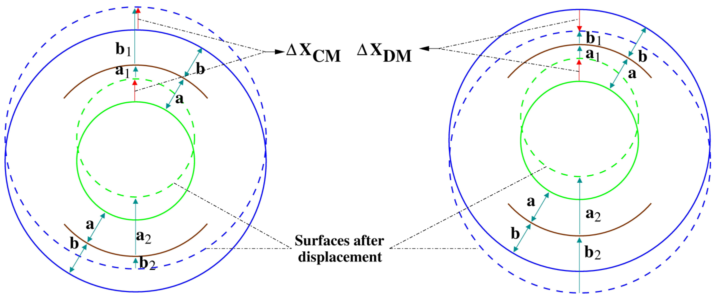

Figure 3.19: The surfaces of the capacitors before and after: a) a common mode displacement and b) a differential mode displacement. For a non zero $(a-b)$ both a differential and a common mode displacement would contribute to the (capacitance) unbalance of the bridge, hence to the output potential.

The test cylinders are coupled in such a way that the natural frequency in common mode is about 10 times higher than that in differential mode, which makes the system 100 times more rigid in response to common mode forces. In addition to our efforts in centering the capacitance cage (i.e. in reducing $(a-b)$) this takes care to reducing the response of the bridges to common mode forces. Then, sensitivity to differential effects is improved by: a) reducing noise sources which are known to be differential; b) improve the balance of the test cylinders so as to better reject common mode effects.

A sinusoidal signal (1 V) of high frequency (400 kHz) is applied to the bridge in order to shift the signal of interest to a high frequency band with reduced $1/f$ electronic noise. The high frequency signal from the bridge is first amplified, demodulated and then digitized by a 24 bits ADC. Fig. 3.15 reports this scheme of the rotating analog electronics completely.

Since the capacitance bridges rotate with the accelerometer, power and data transfer must be ensured between the rotating and non-rotating reference frame. For power transfer we use an ad hoc power coupler (see Sec. 3.3). The digitized data are optically transferred from the rotor to the non-rotating frame by an optical LED placed on the axis of the shaft. In order to be able to transform the relative displacement as measured by the bridges in the rotating frame (O, χ, ψ, z) of the rotor to non-rotating frame of the laboratory (O, x, y, z), we need to know in correspondence of each data point also the phase angle of the rotor. For this purpose a small size, high resolution, non-contact optical rotary chip encoder (from MicroE systems) (see Fig. 3.20) has been chosen. It has a reflective grating on the glass scale and generates 32768 counts per revolution as well as an index pulse. The 32768 pulses are divided by 2^{10} to obtain 32 pulses per rotation by a logical pulse divider (implemented on a FPGA programmable logical chip).

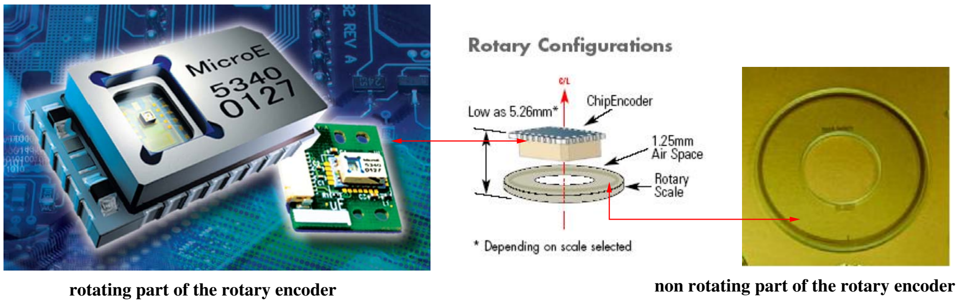

Figure 3.20: Optical rotary encoder, mounting configuration and its reflective grating

The capacitance bridge is calibrated to convert the voltage signal from the bridge to differential displacement between the test cylinders (see Sec. 3.6) for the calibration procedure). The signal of the bridge after digitization is transmitted by using an optical link through a serial bus to the non-rotating system. Finally the transmitted position signal is time stamped using the Rb clock and stored in a PC using LabView real time program for post processing.

3.5 Natural frequencies, whirl motions and whirl control

We have seen that the GGG differential accelerometer is formed by two hollow cylinders weakly coupled to each other with 2D laminar joints through a coupling arm (in the shape of a tube). With 3 bodies involved we expect the system to have 3 natural frequencies (or normal modes) in each direction of the plane. They have been extensively discussed in [1]. The most relevant of these 3 frequencies is the differential one, namely the frequency at which the test cylinders oscillate relative to each other (in each direction). The lower this frequency, the higher the sensitivity of the accelerometer to differential accelerations, i.e. the higher the differential displacement in response to a differential acceleration (the displacement grows as the inverse of the natural frequency squared).

In the current set-up the (rotating) differential accelerometer is suspended by the weak 2D joint below the bearings (co-rotating). We therefore expect another natural frequency to appear corresponding to the pendulum frequency of the entire suspended system (differential accelerometer along with 2D joint below bearing). We must avoid that this frequency and/or its higher harmonics resonate with the 3 natural frequencies of the GGG accelerometer. We know that the oscillation period of the suspended "pendulum" is given by:

$$T_{pendulum} = 2\pi\sqrt{\frac{I_{sp}}{M_{sp} g h_{sp}}} \tag{3.12}$$

where g is the local gravitational acceleration, M_{sp} the total mass of the suspended pendulum, I_{sp} its moment of inertia relative to an axis passing through the suspension point and perpendicular to the oscillation plane, h_{sp} the distance from its center of mass to the suspension point. From the engineering construction drawings of the system we can calculate the value of $T_{pendulum}$ and from the typical values (expected and measured) in the past for the natural frequencies of the differential accelerometer we can establish if there will be danger of resonance or not. Once we saw no danger of a resonance we could proceed with the construction of the suspended apparatus.

With the accelerometer ready for measurements inside the vacuum chamber, the chamber is closed and evacuated. The natural frequencies of the system are measured as follows. The accelerometer does not spin and data from the read out capacitance bridges in between the test cylinders are acquired; they contain primarily the oscillations at the natural differential frequency–since these affect directly the bridges–but they also contain oscillations at the pendulum frequency of the suspended system and at the other two natural frequencies of the accelerometer itself. Though these oscillations are not inherently differential (of the test cylinders relative to each other) they are nevertheless read by the capacitance bridges.

The reason is the following. The GGG accelerometer is designed as a balance in order to reject common mode effects; however common mode rejection is not perfect (particularly at 1-g due to the special role of the vertical direction) which makes it impossible to built the accelerometer as perfectly symmetric, both in azimuth and top/down. Previous analysis shows that common mode effects are rejected by about a factor 700 ([2]-Sec. 4.7). This means that only a fraction 1/700 of a common mode effect affects the test cylinders like a differential one and is therefore read by the capacitance bridges as differential. All the rest of it (699/700, i.e. most of it) affects the test masses in common mode, with a consequent displacement depending on the common mode natural frequency involved (always higher than the differential one), hence yielding a smaller displacement as compared to the case in which the same effect were differential. If the capacitance plates of the bridge were perfectly centered in between the test cylinders this common mode displacement would give no output signal. In reality we expect that it gives rise to a non zero output signal.

We can measure all the natural frequencies of the system from the output data (while the rotor is not spinning) of the read out capacitance bridges which provide the relative displacements of the test cylinders. The FFT of the relative displacement data from χ and ψ bridge respectively allow us to identify all the natural frequencies involved. They are reported in Figs. 3.21 and 3.22 and also tabulated in Table 3.4.

Table 3.4: Measured Normal Mode frequencies of the GGG accelerometer

Bridge	Differential Mode	First Common Mode	Second Common Mode
χ	$\nu_{\chi diff}$=0.124 Hz	$\nu_{\chi com1}$=1.05 Hz	$\nu_{\chi com2}$=1.40 Hz
ψ	$\nu_{\psi diff}$=0.061 Hz	$\nu_{\psi com1}$=1.05 Hz	$\nu_{\psi com2}$=1.40 Hz

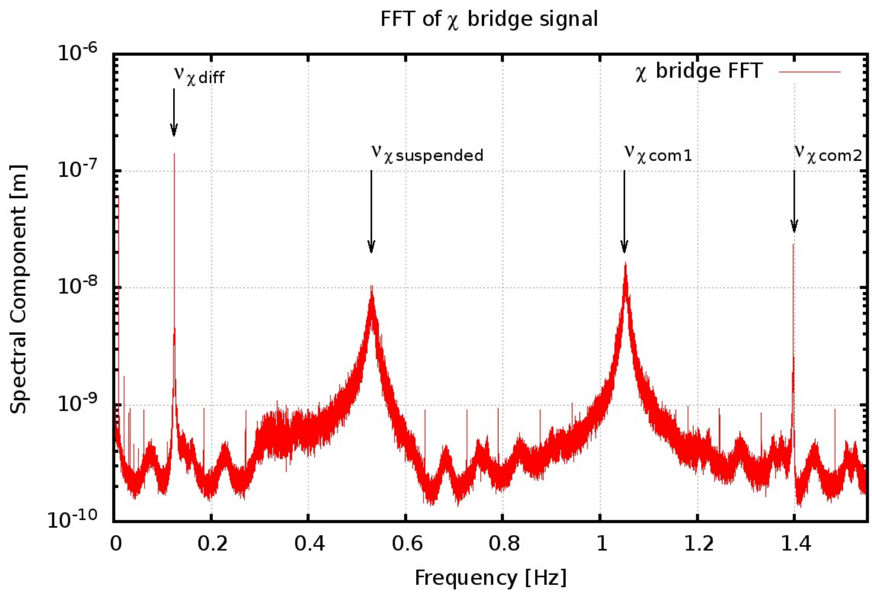

Figure 3.21: FFT of the relative displacements of the test cylinders (system not spinning) in the direction of the χ bridge. The natural frequency of differential oscillations is 0.124 Hz. The natural frequency of oscillation of the entire suspended system is 0.53 Hz. We note also two additional frequencies which are expected for the 2 test cylinders and the coupling arm [3].

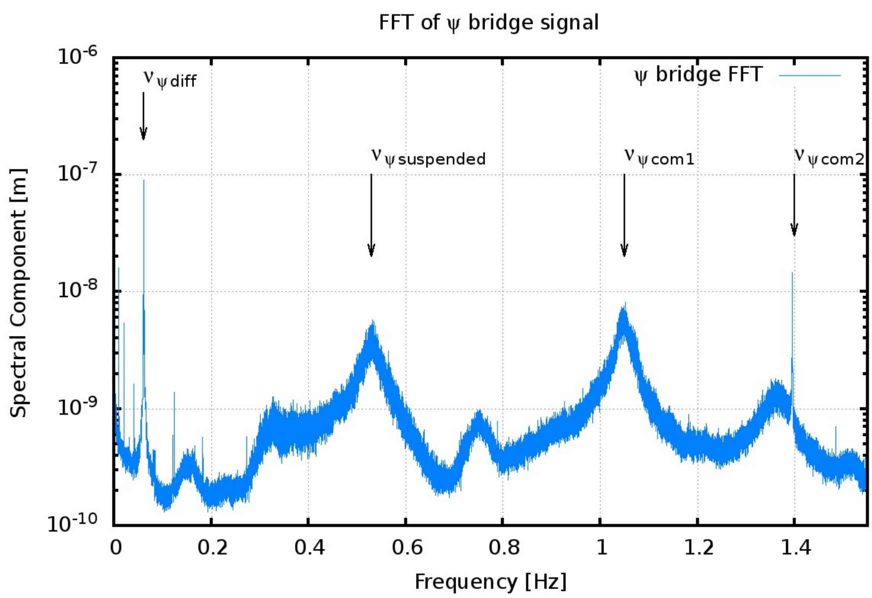

Figure 3.22: Same as Fig. 3.21 in the direction of the ψ bridge

From Figs. 3.21 and 3.22 we notice that the natural frequencies of differential oscillations of the test cylinders in the χ and ψ directions of the rotor are not the same. This is due to differences in the deformations of the 4 lamellae (2 in the χ, 2 in the ψ direction) of the 2D joints which couple the test cylinders (particularly the central one) due to small differences in manufacture of the lamellae in the two directions and the effect of weight. Note that the suspension of the entire system from the rotating suspension below the bearings gives rise to the pendulum frequency of 0.53 Hz.

Consider now the GGG accelerometer when it is spinning at a frequency higher than its natural differential frequency, namely this frequency is in supercritical regime. When the rotor spins, in order to understand its dynamical behaviour we must compare the spin frequency with the natural frequencies (normal modes) of the rotating system. In supercritical regime the first important fact is autocentering: the centers of mass of the rotating test cylinders, which are necessarily not coincident because of inevitable construction errors will be closer to each other than they were by construction, thus reducing disturbances due to centrifugal forces.

As we have seen in Sec. 2.2, the equations of motion (2.2) in the presence of internal damping in the suspensions result in the onset of whirl motions in the non-rotating frame in the form:

$$\vec{r}_w(t) \simeq A_0 e^{\phi_{\omega_{spin}}\omega_n t/2} \begin{pmatrix} \cos(\omega_n t + \varphi_A) \\ \sin(\omega_n t + \varphi_A) \end{pmatrix} + B_0 e^{-\phi_{\omega_{spin}}\omega_n t/2} \begin{pmatrix} \cos(-\omega_n t + \varphi_B) \\ \sin(-\omega_n t + \varphi_B) \end{pmatrix} \tag{3.13}$$

where the amplitudes and phases are determined by initial conditions, $\omega_n = \sqrt{k/(m/2)}$ is the natural differential angular frequency, $\omega_{spin} \gg \omega_n$ is the spin angular frequency and $\phi_{\omega_{spin}}$ is the loss angle (see e.g. [4]). This solution shows that in the inertial reference frame the oscillator performs a combination of a forward and a backward orbital motion–(slow) natural frequency ω_n, and the radii of such orbits are exponentially decaying in the case of the backward whirl and exponentially growing in the case of the forward one. The exponential depends on the loss angle:

$$\phi_{\omega_{spin}} \simeq \frac{\gamma_{\omega_{spin}}\omega_{spin}}{\mu\omega_n^2} = \frac{\gamma_{\omega_{spin}}\omega_{spin}}{k} \tag{3.14}$$

which is very small because the system has very small losses; the smaller the losses, the slower the growth rate of the forward whirl.

We can summarize briefly as follows (see [5],[6],[7],[8],[9],[10],[11]):

- A circular forward whirl motion is occuring in the same direction of the spin and is self–excited. The amplitude grows exponentially in time but since $\gamma_{\omega_{spin}}$ is very small it is a very weak instability. Every natural/whirl period, the radius of the forward whirl grows by the fraction $\pi\phi_{\omega_{spin}}$, hence the tangential force which produces the growth is –in modulus– $\phi_{\omega_{spin}} kr$, which is a very small fraction of the elastic force, requiring a correspondingly small force to stabilize it. Its frequency is the natural one and does not interfere with the signal.
- A circular backward whirl motion of test masses occurs in the opposite direction of the spin and is self–damped.

Control force: As already shown the whirl motion can be described by the vector:

$$\vec{r}_w = r_w \ e^{t/\tau_w} \ \big(\cos(\omega_n t), \sin(\omega_n t)\big) \tag{3.15}$$

where $\tau_w = 2Q_{spin}/\omega_n$ and $Q_{spin} = 1/\phi_{\omega_{spin}}$. If the loss angle is very small the quality factor is very high ($Q_{spin} \gg 1$) and the time constant τ_w is long compared to the whirl period T_w, namely $\tau_w \gg T_w$. Hence we can write the modulus of the whirl radius (3.15) as:

$$r_w(t) \simeq r_w(0)\left(1 + \frac{\omega_n t}{2Q_{spin}}\right). \tag{3.16}$$

Following [5] and [11] we write the fractional increase after 1 natural (whirl) period of the amplitude of the whirl (orbital) motion

$$\frac{(\Delta r_w)_{T_n}}{r_w} \simeq \frac{\pi}{Q_{spin}} \tag{3.17}$$

and interpret this increase in amplitude as due to an acceleration along-track (along the whirl orbit), that we call a_w, such that

$$\frac{1}{2}a_w T_n^2 = 2\pi(\Delta r_w)_{T_n} \tag{3.18}$$

yielding:

$$a_w \simeq \frac{1}{Q_{spin}}\omega_n^2 r_w. \tag{3.19}$$

This is the acceleration which increases the orbital velocity and causes the whirl radius to grow. However, we can see that the corresponding force is very small:

$$F_w = \mu a_w = \frac{1}{Q_{spin}}\mu\omega_n^2 r_w = -\frac{1}{Q_{spin}}kr_w = \frac{1}{Q_{spin}}F_{suspension} \tag{3.20}$$

because it is only $\frac{1}{Q_{spin}}$ of the elastic force of the suspension and it is $Q_{spin} \gg 1$ (we have used the fact that the centrifugal force due to the orbital whirl motion is balanced by the restoring elastic force of the suspension).

The whirl velocity is obtained by taking the derivative of (3.15), which is:

$$\dot{\vec{r}}_w = r_w\ e^{t/\tau_w}\ \big((\cos(\omega_n t)/\tau_w - \omega_n \sin(\omega_n t)), (\sin(\omega_n t)/\tau_w + \omega_n \cos(\omega_n t))\big). \tag{3.21}$$

Since $\tau_w \gg T_w$, $1/\tau_w \ll \omega_w$, the first term can be neglected and we obtain the whirl orbital velocity which must be damped:

$$\dot{\vec{r}} \simeq r_w \omega_n e^{t/\tau_w}(-\sin(\omega_n t), \cos(\omega_n t)). \tag{3.22}$$

By observing that $\sin(\omega_n(t - T_w/4)) = -\cos(\omega_n t))$ and $\cos(\omega_n(t - T_w/4)) = \sin(\omega_n t))$, (3.22) becomes

$$\dot{\vec{r}} \simeq -\omega_n \vec{r}_w(t - T_w/4) \tag{3.23}$$

showing that the damping signal which is proportional to the whirl velocity is obtained by delaying the relative displacement (3.15) by $(T_w/4)$.

We have seen that the whirl motion is a slow instability which can be damped by applying a force along-track (equal and opposite to (3.20)), which is much smaller than the elastic force which couples the test masses. Moreover, this force, being along-track does not substantially affect the relative position vector of the test masses in the radial direction, which is the physical quantity of interest. Any residual whirl appears in the data at a well known natural frequency and does not interfere with the sensitivity of the accelerometer at the very low frequencies of interest.

Whirl control in GGG: In the GGG rotor whirl motion is damped using non rotating capacitance sensors/actuators. Since whirls occur at the natural frequencies in the inertial (non rotating) frame, this is the simplest thing to do. The capacitance plates of whirl control face the outer test cylinder only, i.e. they detect only the motion of the outer test cylinder and act only on it. This allows whirl motion of both masses to be damped because they are coupled to each other via the coupling arm.

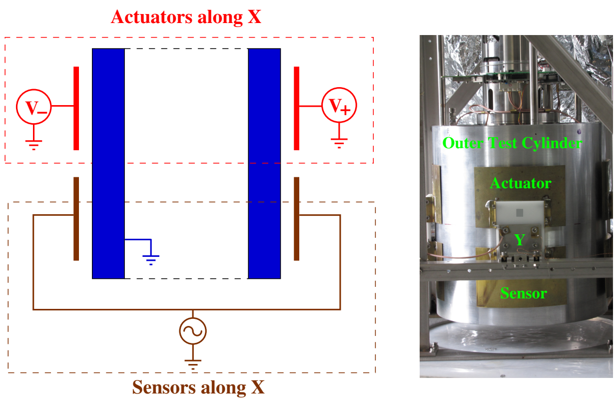

Figure 3.23: Simplified schematic and real arrangement of sensors/acturators used for control of the whirl in GGG. The section is shown through the spin axis of the outer test cylinder (blue). 8 capacitance plates are placed near the outside of the outer test cylinder (only four plates are shown). They are fixed with the vacuum chamber and hence fixed in the non-rotating laboratory frame (X-Y). One half of them is used as sensors: measurements of the displacement of the outer test mass are used to build a damping command proportional to its velocity. The other half is used as actuators: control voltages ($\mathrm{V}_+ = \mathrm{V}_{\mathrm{const}} + \alpha \mathrm{v}_{\mathrm{x}}$) and ($\mathrm{V}_- = \mathrm{V}_{\mathrm{const}} + \alpha \mathrm{v}_{\mathrm{y}}$) are applied in the range of (0-360 Volt) which are proportional to whirl velocity in order to damp whirl motion. Where and α, $\mathrm{V}_{\mathrm{const}}$(=180 Volt) and ($\mathrm{v}_{\mathrm{x}}$,$\mathrm{v}_{\mathrm{y}}$) are the amplifier gain, constant voltage applied to 4 actuator plates and components of the whirl velocity respectively. The X (Y) component of the active force is proportional to the X (Y) component of the whirling velocity.

When the GGG accelerometer is in supercritical regime, the centres of mass of the test cylinders develop an orbital motion around their position of relative equilibrium in the horizontal plane of the laboratory (X-Y) due to whirl (see Figs. 3.24, 3.25 and 3.26). As already discussed, only forward whirl has to be damped due to its instability. It is actively damped by means of capacitance based sensor/actuator arrangement as shown in Fig. 3.23. The controlling force is applied on the outer test cylinder. In order to avoid the influence of control force on the equilibrium position of the test masses (it will affect the low frequency signal of interest) the control force applied is proportional to the velocity of the outer test cylinder in the laboratory frame (X-Y) and opposite in phase.

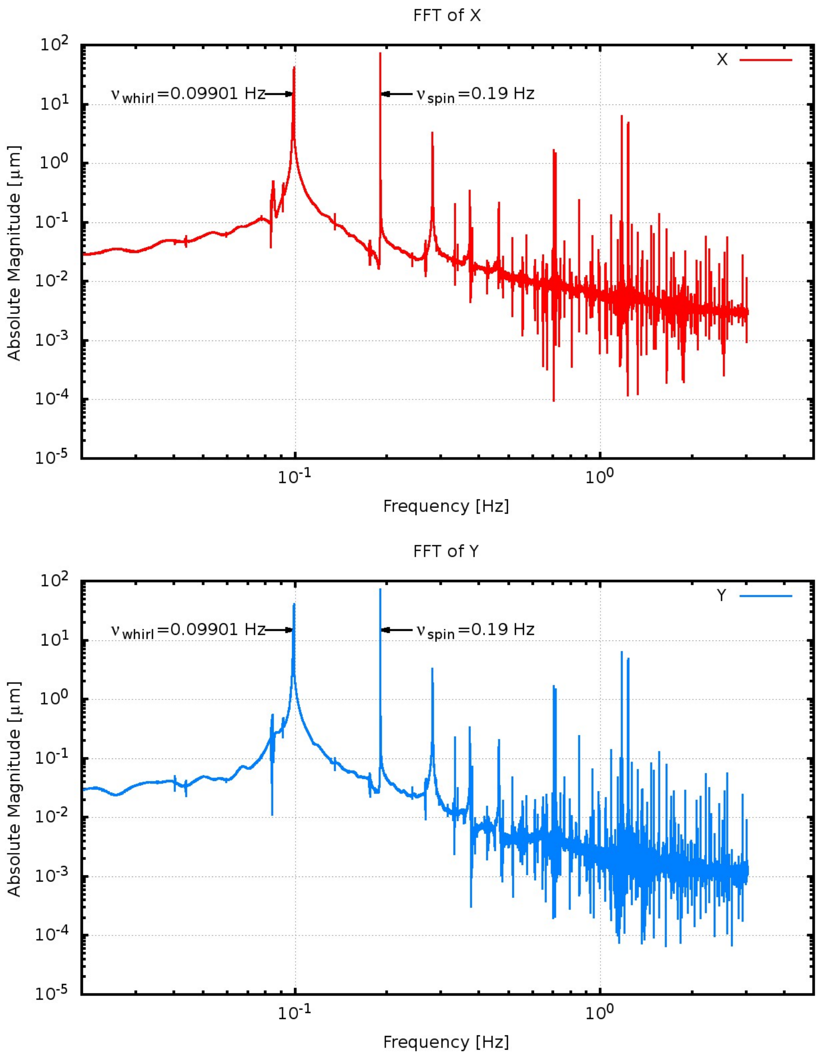

Figure 3.24: Top: FFT of the signal in the laboratory frame X Bottom: FFT of the signal in the laboratory frame Y. The 1^{st} and 2^{nd} peaks from the left are the frequency of whirl and spin respectively.

The outer test cylinder is surrounded by two sets of four capacitance plates each. The upper four are actuators and the lower four are sensors. The plates used as actuators have the same dimensions as those used as sensors and are arranged symmetrically with respect to the outer text cylinder. In the lower set each pair of opposite plates form one sensor. Thus there are two sensors one along X direction and the other along Y. They are mounted on the fixed frame and hence rigid with the vacuum chamber. Each plate forms one capacitor in an AC capacitance bridge. The bridge is balanced initially at the equilibrium position of the test cylinders, which is held at ground potential. Any subsequent displacement of the cylinders causes an imbalance in the bridge, giving rise to an AC signal at the bridge excitation frequency. The bridge is excited at high frequency (350 kHz). The displacement signal is demodulated using an anlog phase-locked-loop circuit, yielding a sensitivity of about $100\,\mathrm{nm}/\sqrt{\mathrm{Hz}}$ in the range $(10^{-2} - 10^{-3}\,\mathrm{Hz})$. The upper four plates similarly form two capacitance actuators, one along X and the other along Y. The capacitance actuator is capable of applying forces in the range of $(-10^{-4}$ to $+10^{-4}\,\mathrm{N})$ with a precision of $10^{-8}\,\mathrm{N}$. Table 3.5 gives the dimensions and characteristics of the actuators and sensors used in GGG.

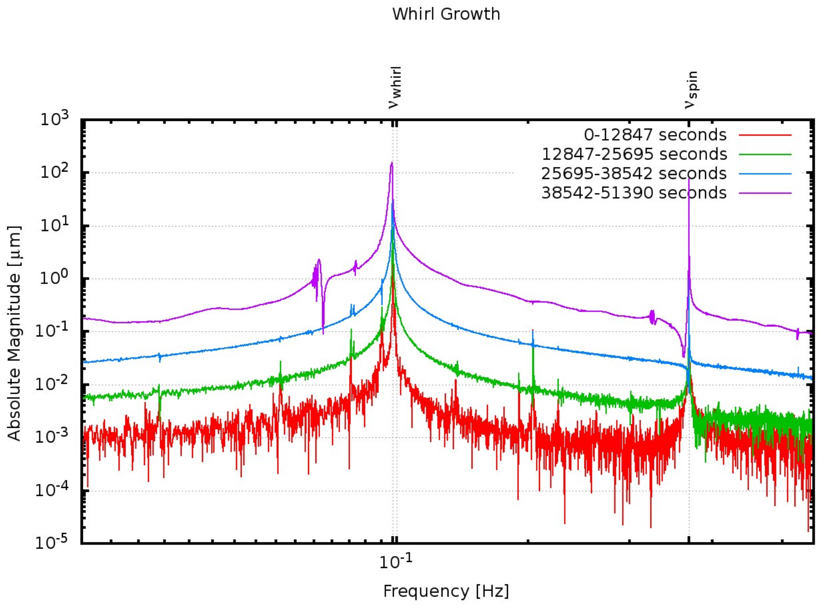

Figure 3.25: FFT of the relative displacements showing growth of the whirl component in the absense of whirl active control.

The whirl control scheme is implemented in Labview by using a NI PCI-6035E DAQ board (16-bit). The whirl control loop is described step by step below. All the individual operations in this loop are user defined and can be altered in real time.

- The whirl motion is registed from the movement of outer test cylinder by the capacitance sensor in two directions X and Y. The outputs of the circuit are two low frequency signals that are acquired. These are the displacements of the external mass in the directions X and Y. The sampling frequency is currently 17.13 Hz. The acquired data are collected in two vectors.
- N components are buffered. We have chosen N=4753
- Buffered components are Fourier transformed with Hanning window applied
- Frequency bands are selected by the user for damping whirl. So 3 digital bandpass filters are applied on the resulting Fourier transformed data.
- This band selected data is inverse fourier transformed to have only the signal which has components of the selected 3 bands to damp. The signals obtained after the filter are the components X and Y of the motion of whirl of the external mass.
- The reconstructed signals are differentiated to obtain the velocity v_x and v_y whirl. The component v_x is obtained from the signal in the X direction, while the component v_y is obtained from the signal Y. In this way, the controlling force in the X direction is proportional to the velocity in this direction. The same applies to the direction Y.
- The resulting signal is delayed by an integer number of perioids of whirl. It is necessary to delay it, because the signal reconstructed is well apart from the last data set (N components) that cannot be used for the control.
- Two 16-bit DACs of the same NI PCI-6035E board converts these digital signals into two analog signals in the DAC limited range between -3 V and +3 V. This voltage is amplified with a gain of α by an external amplifier. Along with this voltage four actuator plates is applied a constant voltage of $V_{const} = 180\,V$. For instance, for the gain of 60, the total voltage applied to the plates varies between ($V_{const} - 3\,V \cdot 60 = 0\,V$) and ($V_{const} + 3\,V \cdot 60 = 360\,V$). If v_x is the x component of whirl velocity in the X direction the control voltage ($V_+ = V_{const} + \alpha v_x$) is applied to the plate placed along positive

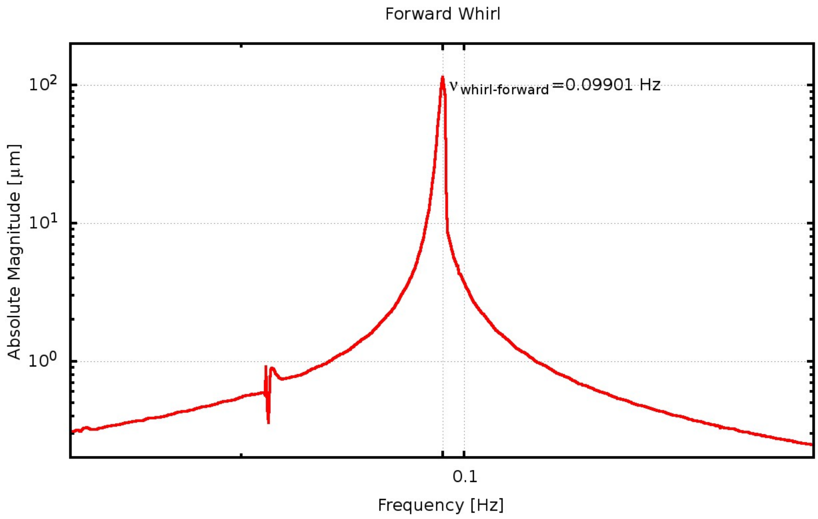

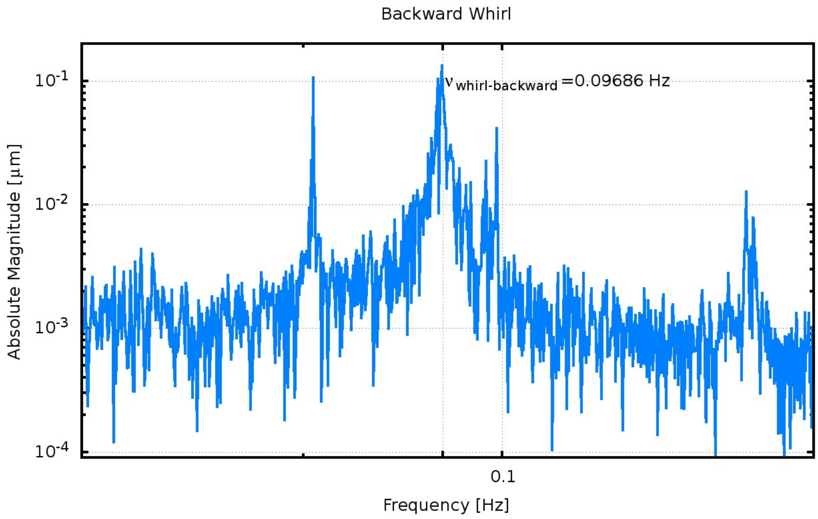

Figure 3.26: Top: Forward whirl Bottom: Backward whirl

X direction while ($\mathrm{V_- = V_{const} - \alpha v_x}$) is applied to the plate in the negative X direction. Then the resultant force exerted by the two plates on the external mass is then:

$$F_X = \frac{1}{2}\epsilon_0 S \frac{V_+^2}{d^2} - \frac{1}{2}\epsilon_0 S \frac{V_-^2}{d^2} = \frac{2\epsilon_0 S}{d^2} V_{const}\alpha v_x \tag{3.24}$$

similarly

$$F_Y = \frac{1}{2}\epsilon_0 S \frac{V_+^2}{d^2} - \frac{1}{2}\epsilon_0 S \frac{V_-^2}{d^2} = \frac{2\epsilon_0 S}{d^2} V_{const}\alpha v_y \tag{3.25}$$

where S is the surface area of the actuator plate, d the distance to the surface of the outer test cylinder. So these two control forces damps the whirl motion completely. All these steps in whirl control loop are shown in Fig. 3.27.

- In this real time control scheme you have provision of adding offset voltages to compensate for any asymmetries in the assembly of the plates and it is also possible to add two sinusoidal signals in the laboratory frame (X-Y). Adding signal was very useful to demonstrate that in a 2D oscillator in supercritical rotation modulation of low-frequency signals by rotation at a frequency above resonance can be performed without the response of the oscillator being attenuated.

As theory predicts that the relevant losses of a supercritical rotor are those at the spin frequency, not at the (lower) natural frequency for which rotation is supercritical. Therefore, by measuring the growth of whirl motion, which is determined by such losses, we can measure the Q of the system at spin frequency,

Table 3.5: Parameters of the whirl sensors/actuators

Height (h)	Width (w)	Area (S)	Distance (d) from Outer TM	ADC & DAC	
Sensors (C = ϵ_0S/d $\simeq$ 22pF)					Displacement Sensitivity
9 cm	14 cm	126 cm^2	5 mm	16 bit	100 nm/$\sqrt{\text{Hz}}$
Actuators					Applied Force (Resolution & Range)
9 cm	14 cm	126 cm^2	5 mm	16 bit	10^{-8} N (-10^{-4} N to $+10^{-4}$ N)

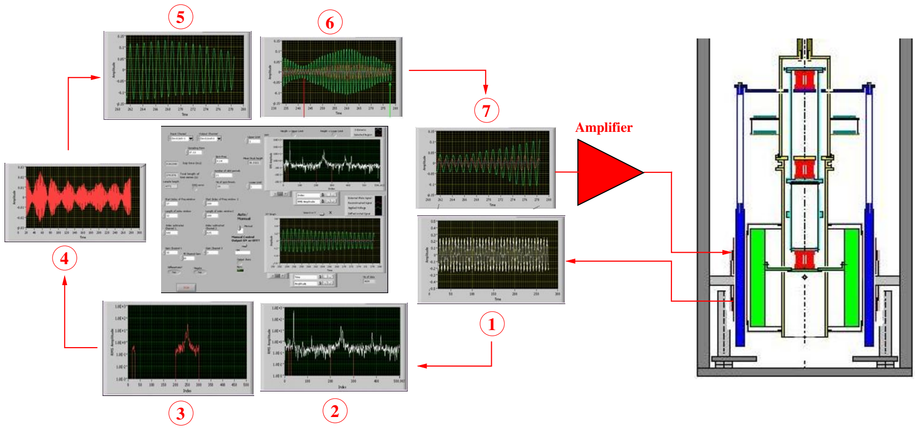

Figure 3.27: Various steps in whirl control loop implemented in Labview: 1. Position of the external test cylinder from capacitance sensors 2. FFT of the position data in order to monitor the spectral components in real-time 3. Selected bands in the frequency spectrum to damp 4. Inverse FFT of the selected bands 5. Differentiate and negate to obtain the control force to apply 6. Control signal delayed by one beat period to keep the phase correct 7. Control signal applied to the actuator plates

in the case of 0.19 Hz. Such measurement is shown in Fig. 3.28. We get Q of about 3200.

It is important to remember that in the case of non-isotropic rotor we have slightly different natural differential frequencies in two orthogonal directions. So when the system spins at a frequency above both these natural frequencies the whirl motions will appear at frequencies given by

$$\nu_{whirl} = \pm\sqrt{\frac{\nu_\chi^2 + \nu_\psi^2}{2}} \tag{3.26}$$

Since the GGG balance has natural frequencies in two directions, $\nu_\chi = 0.0695\,\text{Hz}$ ($T_\chi = 14.39\,\text{s}$) and $\nu_\psi = 0.1244\,\text{Hz}$ ($T_\psi = 8.039\,\text{s}$), which gives $\nu_{whirl} = 0.1076\,\text{Hz}$.

At present the nominal gap between the capacitance plates of the read out and the surface of each test cylinder is about 1 mm. Since we operate at pressure $\lesssim 10^{-4}$ Pa (10^{-6} mbar), losses in the suspensions still dominate over viscous damping due to Brownian motion in the residual air. Losses in the system at a natural oscillation frequency ω_n are expressed by the quality factor Q as given in the equation

$$E(t) = E(0)e^{-\frac{\omega_n t}{Q}} \tag{3.27}$$

expressing the decay in time of the energy E of the system. The higher the value of Q, the lower the losses, the slower the energy decay. Q is measured from the decay of the amplitude A of the oscillation at ω_n. Since:

$$A(t) = A(0)e^{-\frac{\omega_n t}{2Q}} \tag{3.28}$$

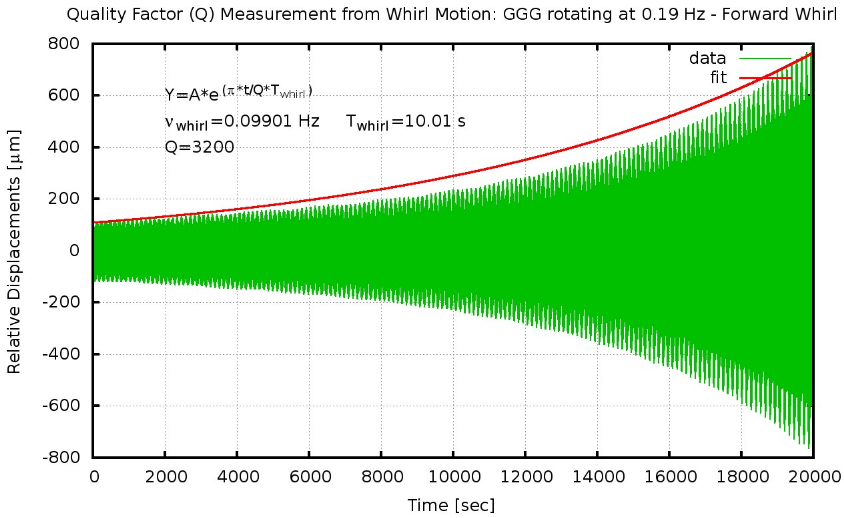

Figure 3.28: Measurement of Q from forward whirl motion. The rotor is spinning at $\nu_{spin} = 0.19\,\mathrm{Hz}$. We get Q of about 3200.

by measuring the amplitudes A_1 and A_2 at times t_1 and t_2 respectively we have:

$$Q = \frac{\omega_n(t_2 - t_1)}{2\ln(\frac{A_1}{A_2})} \tag{3.29}$$

Here we briefly describe the recent measurment procedure for measuring the quality factors at natural frequencies for GGG at zero spin rate. For these measurements we used the main capacitance sensors of GGG. These sensors provide best sensitivity to differential oscillations, while are sensitive to common mode displacements only because of their small common mode sensitivity. This residual common mode sensitivity is sufficient for the measurement of the common mode oscillations quality factors.

A harmonic oscillator of mass m, elastic constant k, natural frequency ω_0 and damping γ has quality factor $Q = \frac{m\omega_0}{\gamma}$, and when subjected to the force $F(t)$ obeys the equation:

$$m\ddot{x} + \gamma\dot{x} + kx = F(t) \tag{3.30}$$
$$\omega_0^2 = \frac{k}{m}$$

Using the Fourier Transform method, from (3.30) we find the transfer function:

$$\left|\frac{\hat{x}(\omega)}{\hat{F}(\omega)}\right| = \frac{1}{m\omega_0^2}\left|\frac{1}{1 - \frac{\omega^2}{\omega_0^2} + i\frac{\omega}{\omega_0}\frac{\gamma}{m\omega_0}}\right| = \frac{1}{m\omega_0^2}\frac{1}{\sqrt{(1 - \frac{\omega^2}{\omega_0^2})^2 + (\frac{\omega}{\omega_0}\frac{\gamma}{m\omega_0})^2}} = \frac{1}{m\omega_0^2}\frac{1}{\sqrt{(1 - \frac{\omega^2}{\omega_0^2})^2 + (\frac{\omega}{\omega_0}\frac{1}{Q})^2}} \tag{3.31}$$

The quality factors have been measured by fitting the Fourier transform of the bridge signals to the function:

$$f(\omega) = \frac{A}{\sqrt{(1 - \frac{\omega^2}{\omega_0^2})^2 + (\frac{\omega}{\omega_0}\frac{1}{Q})^2}} \tag{3.32}$$

with parameters Q, A and ω_0 in a small frequency range around the resonance frequencies. The excitation force source is the background noise force to which the experiment is always subject. We made the reasonable assumption that in the narrow frequency ranges where we interpolated the measured data this background noise is spectrally flat, that is $\left|\hat{F}(\omega)\right| =$ constant. Fig. 3.29 and Table 3.6 refer to data taken in a GGG run of October 2011 GGG. The errors of the results reported are about 0.1 for the Q values, and about 10^{-5} for the frequencies of the differential normal modes.

We compare this result with an old measurement of Q at zero spin rate performed in 2003 (see [3]). At the time of the measurement the nominal gap between the capacitance plates of the read out and

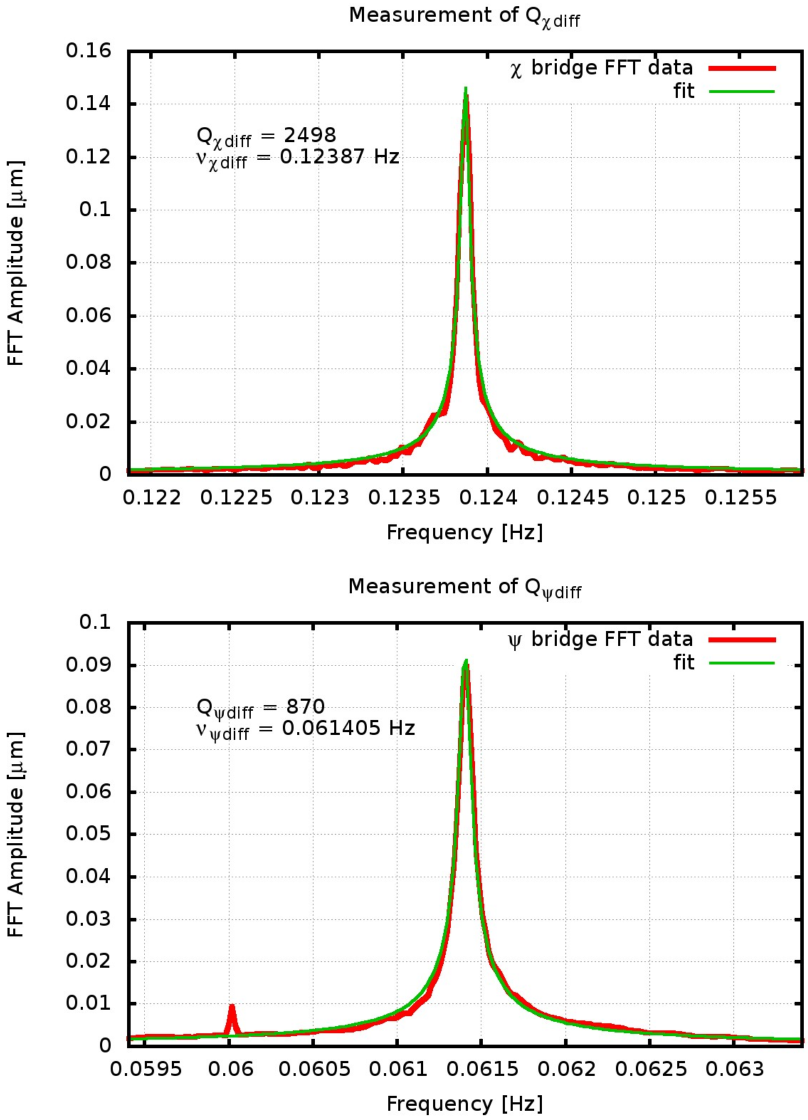

Figure 3.29: Q measurements for displacements in the χ (Top) and in the ψ (Bottom) directions reporting the FFT of the χ and ψ signals of the main GGG capacitive bridge and its interpolation around the resonance peaks corresponding to the differential normal modes.

the surface of each test cylinder was 5 mm. Measurements were performed at about 10^{-3} Pa (10^{-5} mbar) using as read-out the capacitance plates facing the outer test cylinder (see later in the section) since they can detect in addition to differential displacements (from displacements of the outer cylinder) also common mode displacements without rejection. So the Q values of the GGG accelerometer at its 3 natural frequencies, that we know are due to losses in the mechanical suspensions themselves (independent of the pressure), have been measured by exciting it at each natural frequency and measuring the decay in the oscillation amplitude. It is also referred to as internal (or structural) damping. The results are reported in [3] and shown in Fig. 3.30. At that time (along the χ direction) the natural frequencies were: 0.0553 Hz in differential mode and 0.891 Hz and 1.416 Hz in common mode. A peak detection was performed by fitting the signal (in Volt) to the function

$$V(t_i) = \sum_{i=1,2,3} A_i e^{-\frac{t}{\tau_i}} cos(\omega_i t + y_i) \tag{3.33}$$

for all 3 natural frequencies and the parameters of the fit were determined, particularly the time constants $\tau_i = 2Q_i/\omega_i$ of the decay yielding the value of the quality factor at each natural frequency. From Fig. 3.30 we see that, as expected, smaller Q values are measured at lower frequencies. This past measurement shows that the value of Q increases with the frequency (losses are smaller at higher frequencies) reaching

Table 3.6: Measured Quality factors and Differential Normal Mode frequencies at zero spin rate. Relative errors are about 0.1 for the Q values, about 10^{-5} for the frequencies of the differential normal modes.

	Differential Mode
χ	$Q_{\chi diff}$=2500 at $\nu_{\chi diff}$=0.123870 Hz
ψ	$Q_{\psi diff}$=870 at $\nu_{\psi diff}$=0.061405 Hz

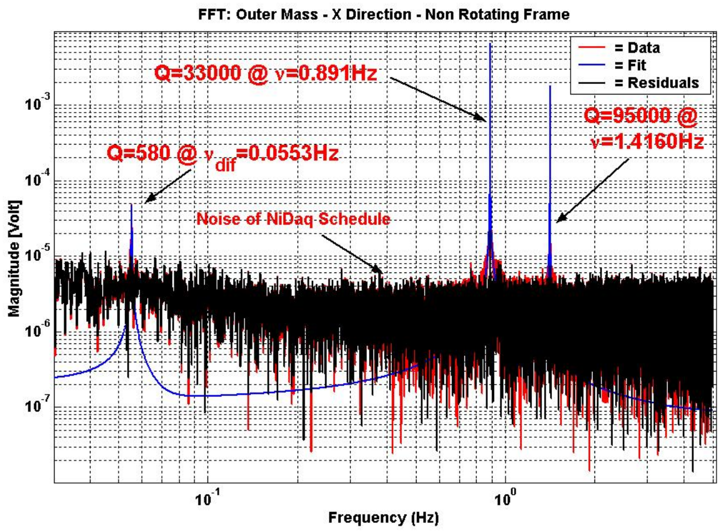

Figure 3.30: Resulting quality factors of the GGG accelerometer at the natural frequencies (at zero spin) as obtained by measuring the oscillation decay of the system as described in the text. Figure taken from [3].

very high value of about 95000 at $\nu_{com2} = 1.416$ Hz. At differential mode $\nu_{diff} = 0.0553$ Hz, Q is about 580.

We can summarize the results of the present and past measurements of Q as follows:

1. Present and past measurements of Q at zero spin rate reveal that Q increases with the frequency (losses are smaller at higher frequencies).

2. In present measurement at zero spin rate Q is different in the two directions (χ, ψ) because of the non-isotropy of the suspensions (the angular spring constant is different in the two orthogonal directions). Again Q increases with the frequency.

3. In the present measurement at $\nu_{spin} = 0.19$ Hz, the rate of whirl growth (for a whirl frequency of 0.099 Hz) yields a Q of about 3200 which (as known from theory) refers to losses at the spin frequency and is an encouraging result (see [5], [11])

3.6 Read-out calibration, self-centering of the test cylinders and balancing of the GGG "balance"

The calibration of the GGG capacitive bridges readout should be performed after the adjustments described in the preceding Sec. 3.6. The gap between the capacitance cage and each one of the test cylinders is about 1 mm, so that the test masses relative displacement range is about 4 mm. The read–out has been calibrated by displacing from the central equilibrium position the outer test mass in the χ and in the ψ directions with a 10 μm resolution micrometric screw gauge as shown in Fig. 3.31. The inner mass displacement was due to its differential coupling to the outer mass. The resulting readout signal versus displacement calibration plots are shown in Fig. 3.32. The calibration factors are obtained as the slope of the straight line fitted to the measured data. The measured calibration factors for the χ and ψ bridges are:

$$\left|\frac{dV_{out}}{dx}\right|_{\chi-sensor} = 1.0824\,\mathrm{mV}/\mu\mathrm{m} \tag{3.34}$$

$$\left|\frac{dV_{out}}{dx}\right|_{\psi-sensor} = 1.2945\,\mathrm{mV}/\mu\mathrm{m} \tag{3.35}$$

Great care was taken that while displacing the test masses in one direction the signal in the other direction stays unchanged. For this purpose we designed an aluminium plate connected with the micrometer screw which moves the outer mass in one direction without sliding in the perpendicular direction, as shown in Fig. 3.31.

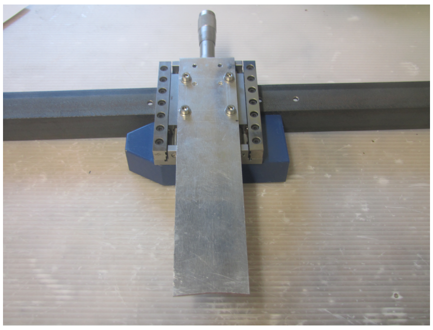

Figure 3.31: Curve-edged aluminum plate and micrometer assembly used for GGG displacement sensor calibration, in order to constrain the motion of the test masses in one direction while calibrating on other direction

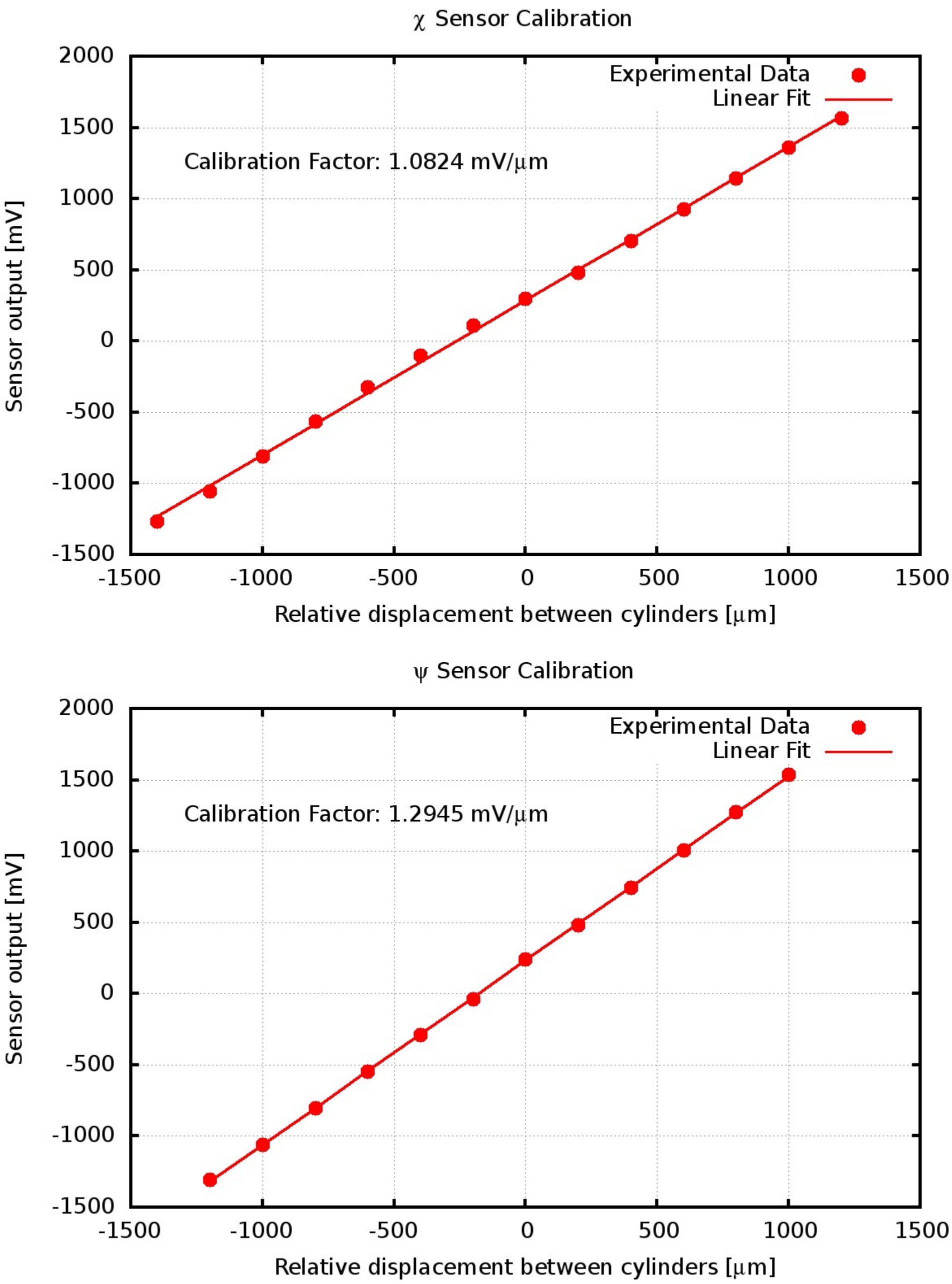

Figure 3.32: Calibration plot of χ and ψ bridges

- The centers of mass of the tests bodies cannot be perfectly concentric. The offset vector $\vec{\epsilon}$ (fixed with the rotating masses) is not zero but in 2D it is reduced by the factor $(\omega^2_{diff}/\omega^2_{spin})$. In these conditions the solution of the equations of motion for the vector $\vec{r}$ of the differential displacement of centers of mass of the test cylinders relative to each other in the horizontal plane of the lab (after demodulation from the rotating frame rotating frame is (see e.g. [4]):

$$\vec{r}(t) \simeq -\varepsilon \left(\frac{\omega^2_{diff}}{\omega^2_{spin} - \omega^2_{diff}} \right) \begin{pmatrix} \cos(\omega_{spin}t + \varphi) \\ \sin(\omega_{spin}t + \varphi) \end{pmatrix} \simeq -\varepsilon \left(\frac{\omega^2_{diff}}{\omega^2_{spin}} \right) \begin{pmatrix} \cos(\omega_{spin}t + \varphi) \\ \sin(\omega_{spin}t + \varphi) \end{pmatrix}. \quad (3.36)$$

We can also write the above expression in the inertial frame (χ, ψ) as:

$$r_{\chi,\psi}(\nu_{spin}) \simeq -\varepsilon_{\chi,\psi} \frac{\nu^2_{\chi,\psi}}{\nu^2_{spin} - \nu^2_{\chi,\psi}} \quad (3.37)$$

At $\nu_{spin} = 0$, measurement gives $\varepsilon_\chi \simeq -220$ μm and $\varepsilon_\psi \simeq -180$ μm (see Fig. 3.34). Self-centering couples ν_{spin} and r. The spectral component of the spin speed noise around ν_{spin} produces a low frequency test masses displacement noise after demodulation to the horizontal non rotating plane of the lab. In presence of a variation $\delta\nu_{spin}$ of the spin speed ν_{spin} we have a variation $\delta r_{\chi,\psi}$ of the test masses diplacement in the rotating frame:

$$\delta r_{\chi,\psi}(\delta\nu_{spin}) \simeq 2\varepsilon_{\chi,\psi} \cdot \frac{\nu^2_{\chi,\psi}\nu_{spin}}{(\nu^2_{spin} - \nu^2_{\chi,\psi})^2}\delta\nu_{spin} \quad (3.38)$$

Considering $\delta\nu_{spin} \simeq 2 \cdot 10^{-4}$ Hz/$\sqrt{\text{Hz}}$ at a frequency $\simeq 10^{-4}$ Hz apart from the spin speed $\nu_{spin} \simeq 0.19$ Hz, see Fig. 3.33, $\varepsilon \simeq 100$ μm and $\nu_{\chi,\psi} \simeq 0.1$ Hz, see Fig. 3.34, this gives $\delta r \simeq 10^{-7}$m/$\sqrt{\text{Hz}}$ of displacement noise in the rotating frame at a frequency $\simeq 10^{-4}$ Hz apart from the spin frequency. When demodulating the test masses displacement from the rotating frame to the non rotating frame of the laboratory this noise is shifted at the low frequency of $\simeq 10^{-4}$ Hz.

It should be noted that the figure of $\varepsilon \simeq 100$ μm can be easily reduced by one order of magnitude by appropriately balancing the GGG rotor. We can also reduce the spin speed noise of the stepper motor with a control loop.

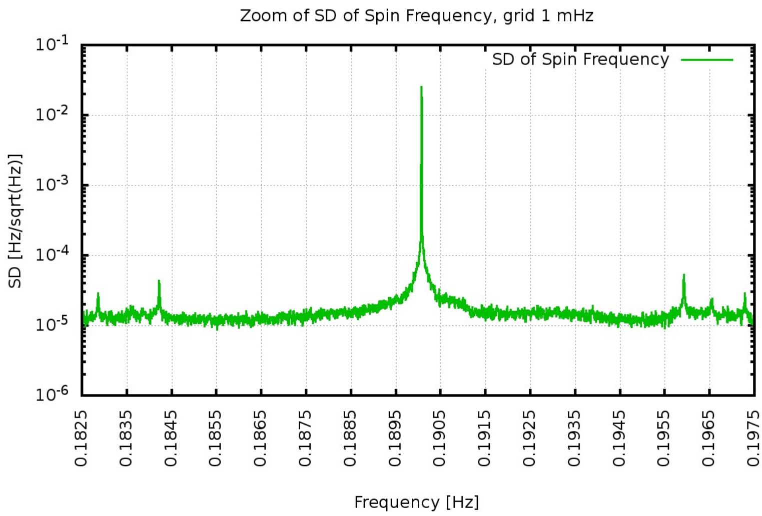

Figure 3.33: GGG rotating at $\nu_{spin} \simeq 0.19$ Hz. The spin speed of GGG is not a constant but is affected by noise. The linear spectral density of the spin speed around the spin frequency $\nu_{spin} \simeq 0.19$ Hz shows that the noise $\simeq 10^{-4}$ Hz apart from the peak is about 10^{-4} Hz/$\sqrt{\text{Hz}}$.

- Since the GGG test bodies are rotors suspended on the Earth and the Earth rotates around its axis, this diurnal rotation gives rise to gyroscopic effects on the test bodies whereby they move not in

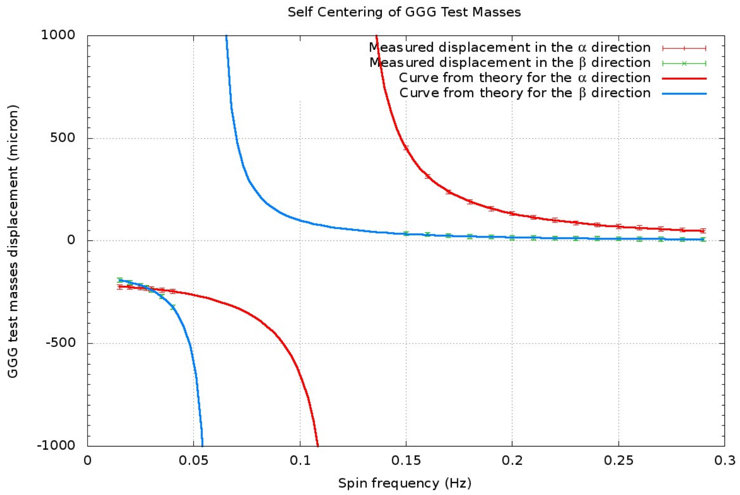

Figure 3.34: Self–centering of GGG test masses. The plot reports the relative displacements of the GGG test cylinders (10 kg, as designed in GG) due to rotation in the χ and ψ directions fixed on the rotor. The center of mass are initially displaced by $\varepsilon_\chi \simeq -220\ \mu$m and $\varepsilon_\psi \simeq -180\ \mu$m. Centrifugal forces due to rotation in sub–critical regime (i.e. at rotation frequencies smaller than the natural frequencies $\nu_\chi = 0.123$ Hz and $\nu_\psi = 0.06$ Hz tend to increase the displacements, while in supercritical regime the test masses displacements go to the opposite direction and are reduced in perfect agreement with the theory of supercritical rotors. In this plot the symbols α and β are used instead of χ and ψ.

the direction of the applied force but along the component of the external torque perpendicular to the spin axis resulting in nonzero differential displacement. In the ground laboratory the gyroscopic effect for a body of mass m, angular momentum and center of mass suspended with an arm is due to the torque generated by the local gravity and to the angular velocity of the Earth's diurnal rotation around its axis, and is given by

$$\left(\frac{d\vec{L}}{dt}\right)_{lab} = \vec{l} \times m\vec{g} - \vec{\omega}_\oplus \times \vec{L} = (\vec{\Omega}_g - \vec{\omega}_\oplus) \times \vec{L} \tag{3.39}$$

where $\Omega_g = -mgl/L$ and $\omega_\oplus$ is the diurnal angular velocity of the Earth. Gravity makes the body precess around the local vertical (unless the center of mass lies exactly on the vertical itself), while the non-inertial nature of the laboratory reference frame (because of its diurnal rotation with the Earth) makes it precess around the Earth's rotation vector; the suspensions produce a restoring force towards the vertical. Equilibrium is reached in the North-South direction, the only direction along which the acting torques can balance each other. The test cylinders of GGG undergo different gyroscopic effects, resulting in a net relative displacement in the North-South direction. Its calculation shows a constant displacement at any given spin rate, and a linear increase with it, reaching several microns at a few Hz; if the laminar suspension of the inner test cylinder is substituted by a rigid connection the differential gyroscopic effect increases by about a factor of 10. In both cases the effect has the same direction and much larger in magnitude. In the past numerous measurements have been performed, at various spin frequencies both in clockwise and counter-clockwise rotation, as reported in Fig. 3.35 (see [12]).

If the spin frequency changes, it has also a direct dynamical effect on the test masses because it changes the amount of relative displacement of the test cylinders due to the gyroscopic effect (which gives a differential acceleration between the test cylinders in the North-South direction). The relevant spin frequency noise in this case is that at the low frequencies of interest (see Fig. 3.36). At 10^{-4} Hz it is about 10^{-8} Hz. From this value and past measurements (see Fig. 3.35), we have

$$\frac{\Delta r_{NS}}{\Delta \nu_{spin}} \simeq 10\ \mu\text{m/Hz} \tag{3.40}$$

$$\delta\nu_{spin} \simeq 10^{-6}\ \text{Hz}/\sqrt{\text{Hz}} \tag{3.41}$$

$$\delta r_{NS} = \frac{\Delta r_{NS}}{\Delta \nu_{spin}} \delta\nu_{spin} = 10^{-11}\ \text{m}/\sqrt{\text{Hz}} \tag{3.42}$$

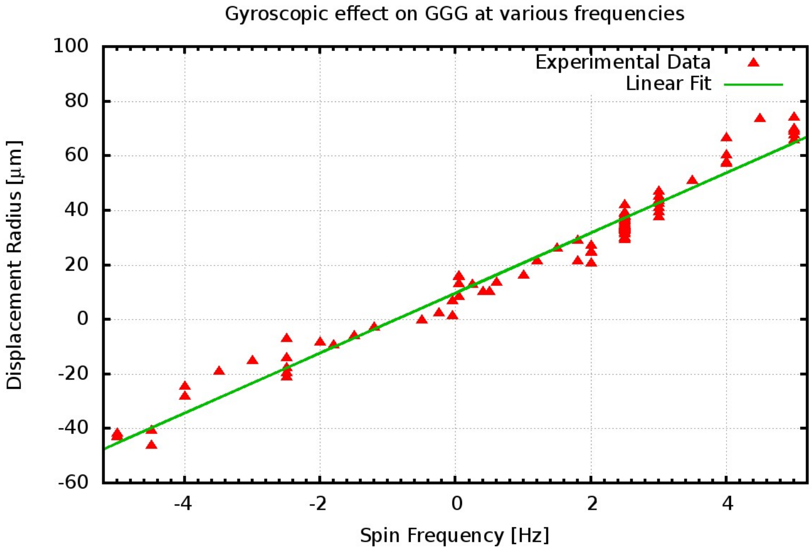

Figure 3.35: Relative displacements (crosses) of the test cylinders, in the non-rotating horizontal plane of the laboratory, as function of the spin frequency and the sense of rotation, with linear fit to a straight line (clockwise frequencies are indicated as negative, counter-clockwise frequencies as positive). The linear increase with the spin rate and the change of sign can be ascribed to the gyroscopic effect. The slope gives $\frac{\Delta r_{NS}}{\Delta \nu_{spin}} \simeq 10\ \mu$m/Hz. The offset at zero spin is due to the inclination of the suspension shaft from the vertical (taken from [12]).

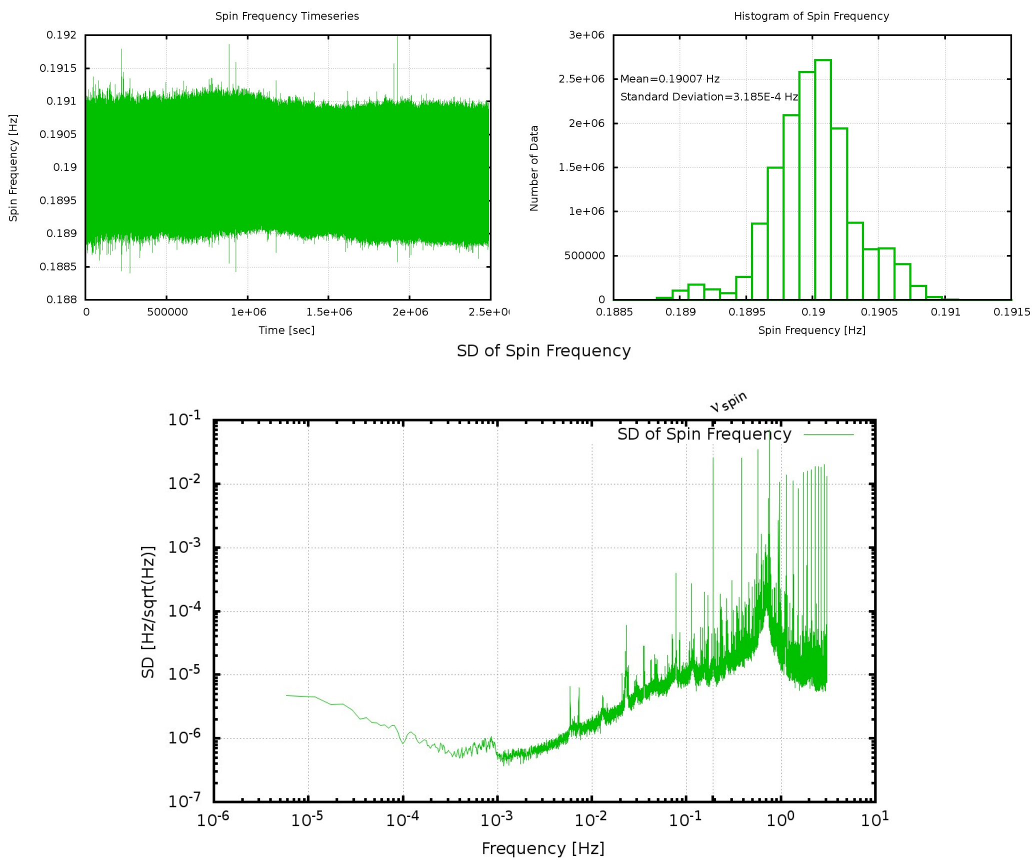

Figure 3.36: Top: Time series of spin frequency and histogram. Bottom: Distribution of the spin frequency noise (spectral density). Measurements show $\delta\nu_{spin} \simeq 10^{-6}$ Hz/$\sqrt{\text{Hz}}$ at 10^{-4} Hz.

and we conclude that the effect is negligible.

The system is designed so that the capacitance cage (assembled and never to be disassembled, rigid with the shaft) is by construction at the right location in between the test cylinder) when they are in the nominal configuration in which the coupling arm is perfectly vertical. The "right" location has been computed taking into account the curvature of the plates and test cylinders surfaces and it turns out to be such that the cage should be closer to the inner cylinder than to the outer one by 50 μm. There is no way of adjusting this configuration: the central cardanic suspension (connecting the coupling arm to the shaft) cannot be moved, therefore the relative position of the cylinders in their nominal position w.r.t. the cage cannot be changed. The cage is an assembled system and individual plates cannot be moved. This was done on purpose because adjustments would be too difficult; we therefore decided to rely on construction.

The adjustments required are (in order of priority):

1. **Alignment of the shaft with respect to spin axis:** The external mass and the three rods which holds it were removed; a comparator was placed in contact with the shaft at the height of the central cardanic joint and at the middle of the capacitive plates respectively. By rotating the shaft its misalignment with respect to the bearing rotation axis is measured. The measured misalignment has been corrected by placing appropriate spacers on appropriate locations of the bayonet attack of the shaft to the spindle. After that the resulting alignment has been measured again with the comparator.

2. **Alignment of spin axis with respect to plumb line:** In case of an inclination of the shaft with respect to the local vertical there will be a deformation of the central suspension which suspends the beam balance and a consequent relative displacement of the test cylinders. The displacement is fixed in the laboratory (non-rotating) frame along the direction identified by the misalignment of the shaft and is modulated by the rotating capacitance bridges at their spin frequency. There are two ways to measure this tilt of the shaft with respect to the plumb line: the first one is a rough measurement using a spirit level; in the second method the χ and ψ readings of the capacitance bridges are transformed into the x and y relative displacements between the test masses in the non-rotating frame that indicate the inclination of the shaft with respect to the local vertical. The adjustment is performed by means of three vertical screws placed at 120° from one another on the steel flange which control the position of the bearing flange, hence the spin axis inclination with respect to the vertical.

3. **Adjustment of the upper cardanic joint position:** The external mass has been mounted; the

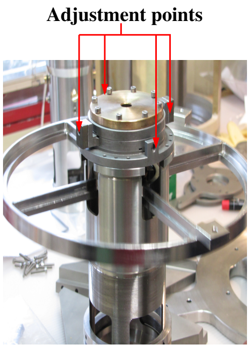

Figure 3.37: Adjustment of the position of the upper cardanic joint

steel plate holding the bearing has been adjusted to be horizontal using a spirit level; We increased the inner mass weight by fixing a brass ring of about 200 gm on the lower cardanic joint. In this way the balance is highly stable. We then measured the positive and negative maximum displacements χ_+, χ_- and ψ_+, ψ_- of the external mass from its equilibrium position to the position in which it is in contact with the corresponding capacitive plate in the directions χ and ψ. We adjusted the position of the upper cardanic joint, see Fig. 3.37 so as to make $\chi_+ = \chi_-$ and the $\psi_+ = \psi_-$. In such a way we centered the inner and outer test masses when the balance is in equilibrium position.

4. **Balancing of the mass offset and zeroing of the capacitive bridge readout electronics:** We started a slow rotation of the balance and we recorded the average over many turns periods of the displacements χ and ψ as a function of the spin frequency. By fitting the measured averaged

displacements to the relationship (3.43) with parameters $M_{offset(\chi,\psi)}$, $E_{offset(\chi,\psi)}$ and $\nu_{(\chi,\psi)}$, we measured the mass and electrical offsets and the differential frequency of the balance. The expression (3.43) is the same representation of the relation (3.37). The differential period of the balance was increased in small steps reducing the weights added to the lower cardanic joint and rising the position of the balancing rings on the coupling arm in small steps; the offsets were measured and corrected after each step.

$$f_{(\chi,\psi)}(\nu_{spin}) = M_{offset(\chi,\psi)} \frac{\nu^2_{(\chi,\psi)}}{\nu^2_{(\chi,\psi)} - \nu^2_{spin}} + E_{offset(\chi,\psi)} \tag{3.43}$$

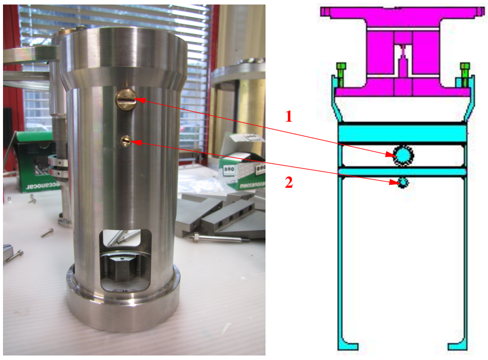

Figure 3.38: The adjustment masses (5 g each) can be displaced across the arm's axis in the χ and ψ directions in order to reduce the mass offsets. For yet a finer adjustment there are two additional smaller masses (0.5 g each).

The mass offset can be reduced by displacing the mass balancing screws of the coupling arm (close to just below the central suspension) across the arm's axis in the χ and ψ directions, see Fig. 3.38. The electrical offsets of the capacitance bridges are corrected by two variable capacitances trimmers. The final result obtained by this iteration procedure is already shown in the Fig. 3.34 of this section. That figure shows the measurement of differential periods, electrical and mass offsets by slow rotation in air by fitting the average mass displacement in the rotating frame to the relation (3.43).

3.7 Up-conversion of low frequency forces without attenuation

As shown in Sec. 2.2, (2.7), a crucial advantage of a 2D oscillator like GGG and GG is that the response to a low frequency signal is not attenuated when the oscillator rotates and up-converts it above its natural differential frequency. The plots in Fig. 3.39 report the result of an experimental test performed with GGG which demonstrates this fact (see [13]).

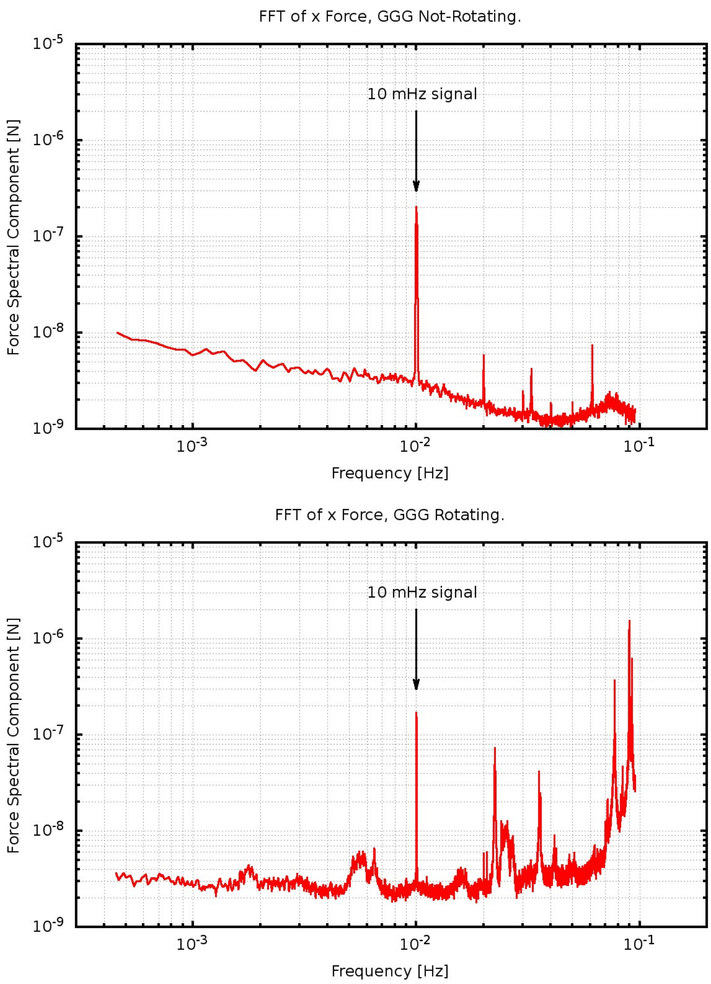

Figure 3.39: GGG measurements showing that in a 2D oscillator in supercritical rotation modulation of low-frequency signals by rotation at a frequency above resonance can be performed without the response of the oscillator being attenuated. (Top): GGG is not rotating and a differential force signal of about 2×10^{-7} N at 0.01 Hz is applied to the test cylinders along the x direction of the horizontal plane of the lab. In this direction, the natural oscillation frequency of the test cylinders relative to each other is $\nu_\chi = 0.124$ Hz; thus, the force is applied below the resonance. (We add that the natural oscillation frequency in the perpendicular direction is $\nu_\psi = 0.063$ Hz). (Bottom): GGG has been set in rotation at $\nu_{spin} = 0.19$ Hz, the natural oscillation frequency during rotation is $\nu_{whirl} = \sqrt{(\nu_\chi^2 + \nu_\psi^2)/2} = 0.098$ Hz and the same force signal is applied, in the same direction x. The force signal is up-converted by rotation above the GGG natural frequency. The experimental data have been demodulated back to the non-rotating horizontal plane of the lab for comparison with the non-rotating case shown before. If GGG were an oscillator in 1D, a similar rotation above its natural frequency would have attenuated its response to signal by a factor 2.56, which would have been easily appreciated. We can see that in a non-rotating case (Top plot) noise at lower frequencies is higher. The real advantage is to up-convert above resonance a signal at very low frequency, where noise in the absence of rotation is considerably higher. This is the case with GGG and GG. In the test presented here, the force was applied at a not so low frequency so that it could be performed with a short duration run. The purpose was to experimentally demonstrate that rotating a 2D oscillator does up-convert a signal to frequencies above resonance without reducing the response of the oscillator to the signal. (Figure taken from [13]).

References

[1] G. L. Comandi *et al.*, Rev. Sci. Instrum. 77, 034501 (2006)

[2] G. L. Comandi, PhD Thesis, (2004)

[3] G. L. Comandi *et al.*, Physics Letters A 318, 213-222 (2003)

[4] R. Pegna *et al.*, Phys. Rev. Lett., 107, 200801 (2011)

[5] A. M. Nobili *et al.*, AAAF-ESA 3, 74189 (1996)

[6] Genta, G., Vibration of Structures and Machines, Springer, New York, (1993)

[7] J. P. Den Hartog, Mechanical Vibrations, (Dover Publications, Inc., New York 1985, First published in 1934)

[8] M. S. Darlow, Balancing of high speed machinery, Springer, New York, (1989)

[9] H. D. Nelson, S. H. Crandall, Analytic Prediction of Rotordynamic Response, Handbook of Rotordynamics, F.E. Enrich Ed., McGraw Hill, (1992)

[10] S. H. Crandall, The role of Damping in Vibration Theory, J. Sound Vib., 11(1), 3-18, (1970)

[11] A. M. Nobili *et al.*, Class. Quantum Grav. 16, 1463-1470 (1999)

[12] A. M. Nobili *et al.*, New Astronomy 8, 371-390 (2003)

[13] A. M. Nobili *et al.*, Class. Quantum Grav. 29, 184011 (2012)

Chapter 4

Tilt and horizontal acceleration noise

4.1 Tilts and horizontal accelerations at low frequencies

Tilt and horizontal acceleration noise in GGG is the subject of [1]. Here we present the most relevant issues in same detail.

In GGG the signals of interest are at very low frequencies: the frequency of the target equivalence principle violation signal in the GG satellite experiment, namely its orbital frequency around the Earth $\nu_{GG} \simeq 1.7 \times 10^{-4}$ Hz at which we want to establish the sensitivity of GGG, and the diurnal frequency ν_{day} at which an equivalence principle violation in the field of the Sun would affect the GGG accelerometer. Therefore only tilts and horizontal accelerations at such very low frequencies are relevant. They are by far much lower than all the "pendulum" frequencies we deal with in GGG, so their effects can be understood as the effects of DC perturbations. Consider first the case of a pendulum suspended inside the vacuum

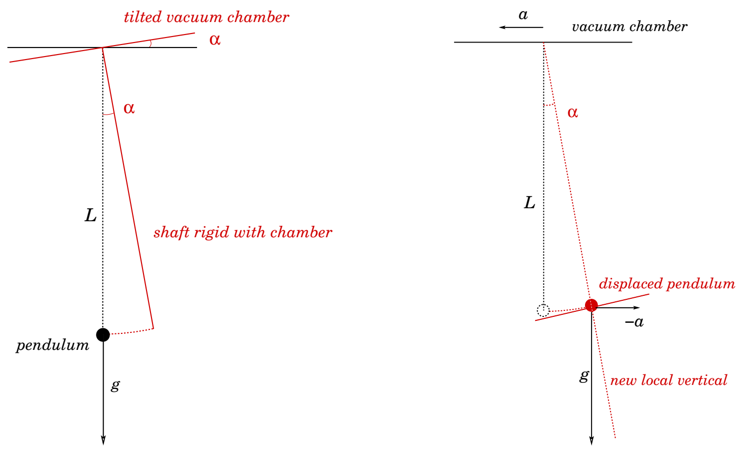

Figure 4.1: Left: Effect of a tilt angle α of the chamber, due to the terrain (of thermal origin or not) or to the chamber itself (of whatever origin too). The pendulum does always identify the direction of the local vertical, but its position relative to the chamber – which was originally coincident with the rigid shaft shown in red – is now displaced from it by the tilt angle α and linearly by $\Delta x \simeq L\alpha$. If the tilt angle α is slowly varying in time we shall observe that this relative displacement will also change with time. Right: Effect of a horizontal acceleration of the vacuum chamber. The equilibrium position is reached at a displaced angle $\alpha \simeq a/g$, yielding a displacement $\Delta x \simeq L\alpha$ of the pendulum mass relative to the chamber (for a displacement of the same sign as in the left figure the horizontal acceleration a should be drawn in the opposite direction).

chamber. It defines the local vertical (as measured relative to the chamber) and we ask how the pendulum position relative to the lab is affected by the perturbations mentioned above. Let us first consider the effect of a tilt of the chamber (for whatever reason), as shown in Fig. 4.1 [Left]. We shall measure a displacement of the pendulum relative to the chamber (see caption).

Consider now (Fig. 4.1 [Right]) the effect caused on the pendulum mass by a horizontal acceleration of the chamber: the pendulum is now in a non inertial accelerated frame and therefore the suspended mass will be affected by an inertial acceleration exactly equal and opposite to that of the accelerated frame. Under the effect of this inertial force and of the local gravitational acceleration, the pendulum mass will

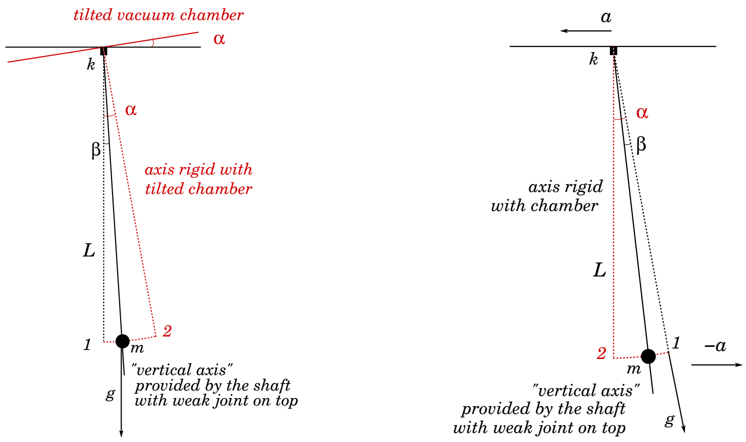

Figure 4.2: Left: Effect of a tilt angle α of the vacuum chamber on a body of mass m attached to a shaft of length L which is suspended from the chamber through a laminar joint providing, in this configuration, a torsional stiffness k. If the shaft were totally rigid (no weak joint) the mass m would be in position 2; if it were a pendulum (as in Fig. 4.1 [Left]) the mass m would be in position 1 (remember that the direction of local gravity is identified by the pendulum). In the case of a rigid shaft with weak joint on top the equilibrium position of the mass m will be an intermediate one, and the forces being balanced are gravity ($g\beta$ component) and the elastic force (towards the axis rigid with the chamber). Notice that the two "extreme" cases considered above are the correct ones. A rigid shaft with an infinitely weak joint is not physically meaningful because it would not be able to carry the weight. Right: Effect of a horizontal acceleration a of the vacuum chamber on a body of mass m attached to a shaft of length L which is suspended from the chamber through a laminar joint providing, in this configuration, a stiffness k. If the shaft were totally rigid (no weak joint) the mass m would be in position 2; if it were a pendulum the mass m would be in position 1 identified by $\alpha \simeq a/g$ as in Fig. 4.1 [Right]. In the case of a rigid shaft with weak joint on top the equilibrium position of the mass m will be an intermediate one, and the forces being balanced are gravity ($g\beta$ component) and the elastic force (towards the axis rigid with the chamber).

reach its equilibrium position where:

$$g \sin\alpha = a \cos\alpha \quad , \quad \alpha \simeq a/g \tag{4.1}$$

thus, a tilt angle α and a horizontal acceleration a which are related as $\alpha \simeq a/g$ (and have the same low frequency time variation) will produce the same displacement of the pendulum mass relative to the chamber (for perfect equivalence between the horizontal acceleration of Fig. 4.1 [Right] should indeed be in the opposite direction with respect to that of the drawing...). Note that this is so because in writing the equilibrium condition (4.1) we have used the equivalence between inertial and gravitational mass.

A very important difference between Fig. 4.1 [Left] and Fig. 4.1 [Right] should be noticed and stressed. The pendulum provides, by definition, the direction of the local vertical, and therefore in this respect Fig. 4.1 [Left] and Fig. 4.1 [Right] are different: the pendulum is unaffected by the tilt (Fig. 4.1 [Left]) while it is affected by the horizontal acceleration (Fig. 4.1 [Right]). However, as long as what is measured is only the relative displacement of the pendulum mass w.r.t the chamber (and the equivalence principle is valid) there is no way of distinguishing the two.

In GGG we don't have masses suspended from wires but masses suspended – in a properly designed manner – from 2D weak laminar joints through rigid arms. Let us therefore consider a system formed by a rigid bar of length L with a mass m at its bottom and a weak joint at its top with torsional elastic constant k (measured in Nm/rad) for rotations around the suspension point along both directions of the horizontal plane. Given a tilt angle α of the chamber, the equilibrium condition for the mass m now reads (see Fig. 4.2 and caption):

$$mg\beta L \simeq k(\alpha - \beta) \tag{4.2}$$

yielding the following β/α tilt attenuation factor:

$$\beta/\alpha \simeq \frac{k}{mgL} \qquad (with\ k \ll mgL) \tag{4.3}$$

As it is clear from Fig. 4.2, the same equilibrium condition holds in the case that the chamber is affected by a horizontal acceleration $a \simeq \alpha g$. It is therefore proved that the effects of tilts and horizontal accelerations (at low frequencies) are totally equivalent and cannot be distinguished. Note that the best attenuation of DC tilt and horizontal acceleration is obtained with very weak joints (small values of k), large mass m and long suspension shaft L.

4.2 Low frequency tilt and horizontal acceleration noise in GGG

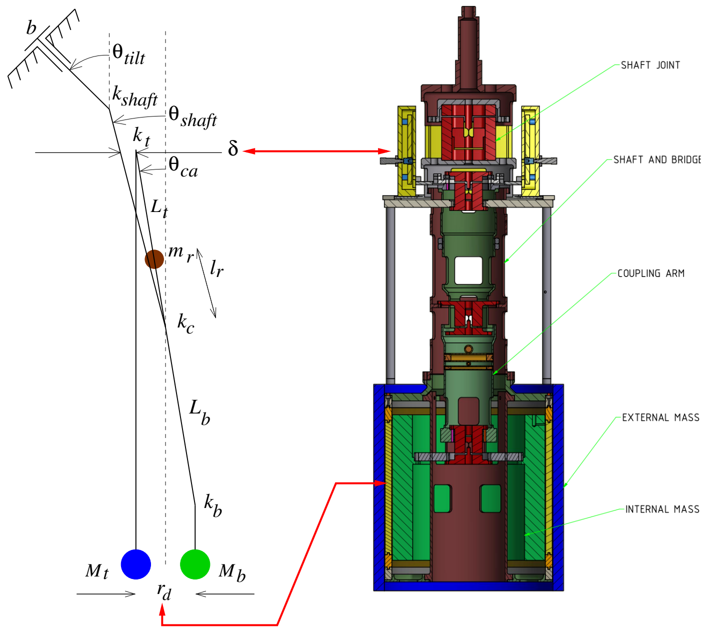

Figure 4.3: Schematic (left) and section (right) of the GGG accelerometer are shown to understand the low frequency tilt attenuation and rejection. Tilt is attenuated by the 2D shaft joint. The displacements δ and r_d are read by the appropriate capacitance sensors (shown by red arrows). M_t, M_b are the masses of the test cylinders (nominally 10 kg each) and m_r is a small regulation mass used to adjust the balance.

Let us now assume that no differential force $\vec{F}$ is applied between the test bodies but the coupling arm is tilted (at very low frequencies) by an angle θ_{ca} from the direction of local gravity as sketched in Fig. 4.3 [Left]. The capacitance bridges shown in Fig. 4.3 in between the test cylinders will measure a low frequency differential displacement (in modulus)

$$r_{d-tilt} = (L_t + L_b)\theta_{ca} \simeq 2L\theta_{ca} \tag{4.4}$$

as due to a low frequency differential acceleration in the horizontal plane

$$a_{d-tilt} = \frac{4\pi^2}{T_d^2} r_{d-tilt} \simeq \frac{4\pi^2}{T_d^2} \cdot 2L\theta_{ca} \tag{4.5}$$

mimicking the effect of the low frequency differential accelerations of interest.

The coupling arm is connected to the local terrain through the shaft, to which it is weakly connected by a 2D laminar joint at its middle point (the pivot point of the balance) of stiffness k_c (Fig. 4.3 [Left]). We must therefore compute the equilibrium value of θ_{ca} in response to a tilt angle of the shaft θ_{shaft}. This is done by writing the potential energy of the system (gravitational plus elastic) whose minimum gives the equilibrium position. If we neglect the mass of the coupling arm with respect to the mass of the test cylinders, and take into account that the axes of the test cylinders are very little affected by the tilts of the shaft, we get:

$$\theta_{ca} \simeq \frac{k_c}{k_t + k_c + k_b - M_t g L_t + M_b g L_b - m_r g \ell_r} \cdot \theta_{shaft} \tag{4.6}$$

where all symbols are defined as in Fig. 4.3 [Left].

Using this relationship between θ_{ca} and θ_{shaft}, and

$$T_d^2 = 4\pi^2 \frac{M_t L_t^2 + M_b L_b^2 + m_r \ell_r^2}{k_t + k_c + k_b - M_t g L_t + M_b g L_b - m_r g \ell_r} \tag{4.7}$$

for the natural differential period, we can write the spurious differential acceleration (4.5) resulting from an input tilt angle of the shaft θ_{shaft} as:

$$a_{d-tilt} \simeq \frac{k_c}{MgL} \cdot (g\theta_{shaft}) \tag{4.8}$$

having used $M_t \simeq M_b \equiv M$, $L_t \simeq L_b \equiv L$ and $m_r \ell_r^2 \ll 2ML^2$. This relationship shows that to reduce the spurious differential effects of tilts of the shaft we should have small values for the elastic constant of the central joint of the balance and large values for the mass of each test cylinder and the length of half the balance arm. However, it is easy to estimate that the values of such spurious accelerations are by far too large as compared with the very small differential accelerations that we would like to detect with this instrument.

It is worth noticing that we have written (4.8) in terms of the acceleration $g\theta_{shaft}$ rather than of the tilt angle θ_{shaft}. As long as we consider low frequencies tilts and horizontal accelerations are perfectly equivalent (see Sec. 4.1 and 4.3). Thus, all statements and results on low frequency tilt noise apply also to the corresponding horizontal acceleration noise, even if the latter is not mentioned. Tilt noise of the shaft is due to local microseismicity and also to imperfections in the bearings, particularly in ball bearings.

4.2.1 Attenuation

If a weight attached to a rigid arm is suspended through a weak joint at the top rather than being rigidly connected, any low frequency tilt of the suspension point will be attenuated; the weight will reach equilibrium at an angle from the local vertical smaller than the tilt. From Fig. 4.3, if k_{shaft} is the elastic constant (in Nm/rad) of the 2D joint placed on the shaft below the bearings, M_{tot} is the total mass suspended from it and L_{equiv} the length of the equivalent arm of the suspended system, obtained by adding the gravitational torques of all weights involved, under an input tilt angle θ_{tilt} the shaft will reach equilibrium at an angle θ_{shaft} given by:

$$\theta_{shaft} \simeq \frac{k_{shaft}}{M_{tot} g L_{equiv}} \cdot \theta_{tilt} \tag{4.9}$$

and using it in (4.8) we get:

$$a_{d-tilt} \simeq \frac{k_c}{MgL} \cdot \frac{k_{shaft}}{M_{tot} g L_{equiv}} \cdot (g\theta_{tilt}) \tag{4.10}$$

which provides the spurious differential acceleration noise in response to a low frequency input tilt of the top of the shaft by the angle θ_{tilt}.

4.2.2 Rejection

The acceleration a_{d-tilt} is a response in differential mode to a tilt/horizontal acceleration of the shaft that the balance is suspended from, which is a disturbance "common" to the whole balance. We can therefore reject the effects of such tilts.

At low frequencies (4.6) relates the tilt angle θ_{ca} of the coupling arm in response to a given tilt angle θ_{shaft} of the shaft it is suspended from (see Fig. 4.3). We notice that the denominator of (4.6) is essentially $k_t + k_c + k_b - m_r g \ell_r$ (because $M_b g L_b - M_t g L_t \simeq 0$) where the elastic constants of the laminar joints are small. Therefore, it is apparent that the mass m_r and arm ℓ_r of the regulating body can be adjusted in such a way that the product $m_r g l_r$ counter balances all other quantities at the denominator except the elastic constant of the central joint k_c, so that, as a result it will be:

$$\theta_{ca} \simeq \theta_{shaft} \tag{4.11}$$

In these conditions the coupling arm will "exactly" follow the tilts of the shaft, so that, if we measure their relative displacement δ (see Fig. 4.3) it will be "unaffected" by the tilts of the shaft. In reality the effects of tilts of the shaft on the relative displacement δ will be rejected by a finite factor. See Fig. 2.4 for the capacitance read-out that will measure δ (see also Fig. 2.2 and Fig. 2.3).

Using the regulating mass to achieve (4.11) amounts to changing the natural period T_d, given by (4.7). In point of fact, the denominator of (4.7) is the same as the denominator of (4.6) and is affected by the regulating mass, while the numerator is not. More precisely, using (4.7) we can write (4.6) as

$$\theta_{ca} \simeq \frac{T_d^2}{\tau^2} \cdot \theta_{shaft} \tag{4.12}$$

where we have defined the time τ as:

$$\tau^2 \equiv 4\pi^2 \frac{M_t L_t^2 + M_b L_b^2 + m_r \ell_r^2}{k_c} \simeq 4\pi^2 \frac{2ML^2}{k_c} \quad . \tag{4.13}$$

Note that, unlike T_d, τ is essentially not affected by small adjustments of the regulating mass m_r and of its arm ℓ_r because $m_r \ell_r^2 \ll 2ML^2$. To the contrary, small changes of $m_r \ell_r$ can significantly affect the denominator of (4.7) and significantly change the value of the natural period of differential oscillations T_d. Thus, adjusting the regulating mass and its arm in order to achieve (4.11) and reject the low frequency tilts of the shaft amounts to making the differential period equal to the time τ given by (4.13). Note that the only elastic constant involved in the value of τ is the elastic constant k_c of the central suspension of the balance.

It is important to notice that even with the tilt rejection, the relative displacements r_d read by the capacitance sensors in between the test cylinders (see Fig.4.3) still registers the effect of θ_{shaft}, while the displacements δ read by the appropriate capacitance sensor rejects the effects of θ_{shaft} upto a finite level.

4.2.3 Terrain tilt input noise

It is important to understand the tilt input noise to the GGG accelerometer at frequencies where its low frequency performance is affected. Knowledge is required of the level of tilt noise at frequencies ν_{GG}, ν_{day} and also ν_{spin} and $2\nu_{spin}$ (see Sec. 4.4). These tilts may originate from two sources, namely from the terrain where the apparatus is sitting and from the bearings which are used to spin the accelerometer. In this section we report the level of terrain tilt input noise at these frequencies as measured with great care by an ISA tiltmeter designed for space applications by V. Iafolla at IFSI lab (in a very quiet location a few meters underground and in a well isolated room) and by ourselves in downtown Florence with an accelerometer provided by him.

- Fig. 4.4 reports the long term measurements of tilt noise performed with ISA tiltmeter by V. Iafolla and by ourselves at the above mentioned locations. At $\nu_{GG} = 1.7 \cdot 10^{-4}$ Hz the lowest tilt noise is recorded underground and it is 25 times smaller than the one measured in Florence. For GGG we assume an input tilt noise only a factor 2.5 smaller than the value measured downtown Florence. This is a rather conservative assumption because our current lab in San Piero is certainly more quiet than downtown Florence.

- Fig. 4.5 reports another measurement of tilt noise performed with ISA tiltmeters by V. Iafolla from which we can get the tilt noise input at frequencies $\nu_{spin} = 0.2$ Hz and $2\nu_{spin}$ amounting to a few 10^{-8} rad/$\sqrt{\text{Hz}}$. The red and blue curves are measurements performed with two "equal" ISA accelerometers next to each other on a "stable" bench. The black curve is the difference of the two measurements. So the common mode rejection obtained in this way shows that the accelerometers are dominated by local noise, not by their intrinsic noise. According to V. Iafolla, even at low frequencies, where the electronic noise is obviously higher, the local tilt noise is the dominant error source for the instrument. This figure shows that terrain tilts (as measured before rejection) are smaller at frequencies close to 0.1 Hz, with values of about $7 \cdot 10^{-9}$ rad/$\sqrt{\text{Hz}}$ and a minimum peak of $3 \cdot 10^{-9}$ rad/$\sqrt{\text{Hz}}$.

With this level of terrain input noise we expect that the current improved design of suspensions (Ch. 5) will help us to meet the goal.

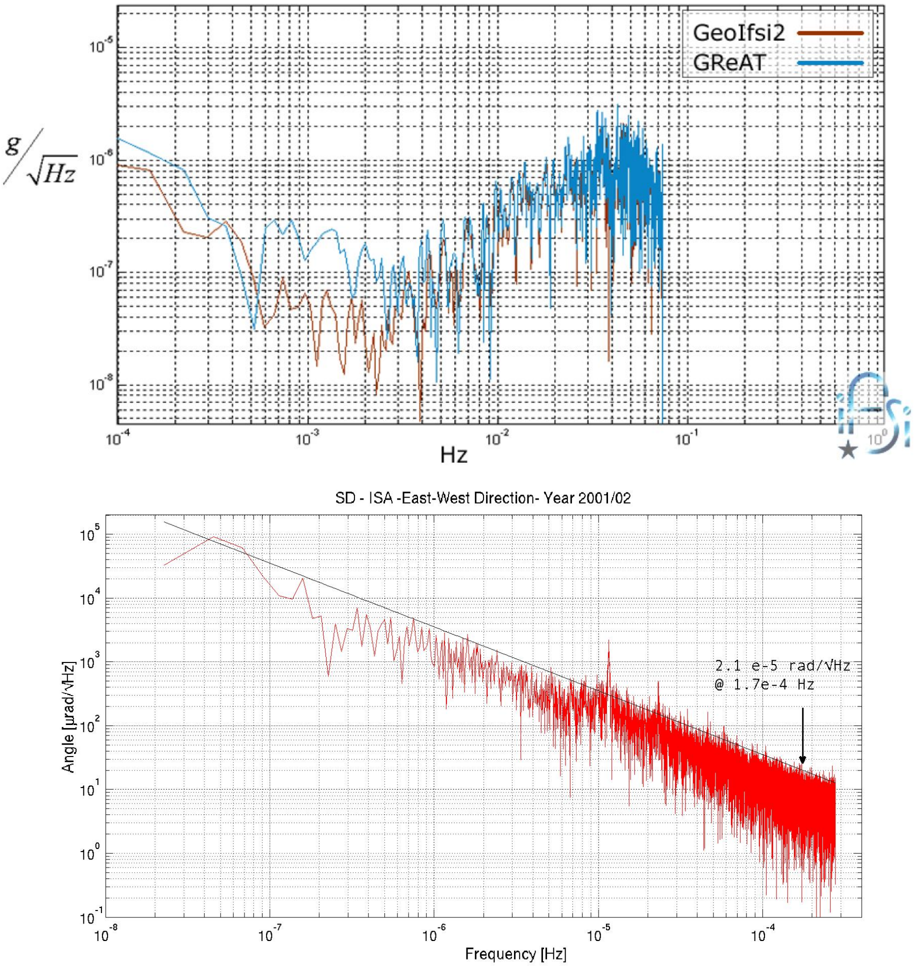

Figure 4.4: Top: terrain tilt noise as measured by V. Iafolla's ISA accelerometer in two different locations at IFSI lab (Roma Tor Vergata) (g is equivalent to rad), showing at the frequency $\nu_{GG} = 1.7 \cdot 10^{-4}$ Hz a noise of $9 \cdot 10^{-7}\,\mathrm{rad}/\sqrt{\mathrm{Hz}}$ in a quiet location and of $3 \cdot 10^{-7}\,\mathrm{rad}/\sqrt{\mathrm{Hz}}$ in an underground room. Bottom: terrain tilt noise as measured in Florence (over 16 months) with an ISA tiltmeter, showing $2.1 \cdot 10^{-5}\,\mathrm{rad}/\sqrt{\mathrm{Hz}}$ at ν_{GG}. In this plot peaks at ν_{day} and $2\nu_{day}$ are also visible.

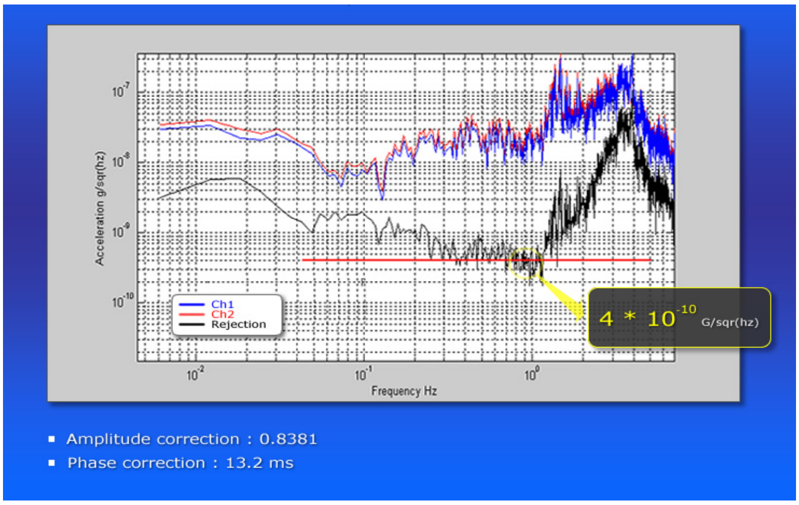

Figure 4.5: Terrain tilt noise as measured by V. Iafolla's ISA accelerometer. The red and blue curves are measurements performed with two "equal" ISA accelerometers next to each other on a "stable" bench. The black curve is the difference of the two measurements. The rejection of common tilts demonstrates that the intrinsic noise of each accelerometer is lower than the terrain tilt noise. At the frequency $\nu_{spin} = 0.2$ Hz the tilt noise is about $2 \cdot 10^{-8}\,\mathrm{rad}/\sqrt{\mathrm{Hz}}$ and at $2\nu_{spin} = 0.4$ Hz noise is about $3 \cdot 10^{-8}\,\mathrm{rad}/\sqrt{\mathrm{Hz}}$.

4.3 Tilt and horizontal acceleration noise at all frequencies

Consider a compound pendulum suspended at its top by a weak joint of elastic constant k (in Nm/rad) and damping coefficient γ (in Nms/rad); let m be its mass, h_{cm} the distance of its center of mass from the suspension point and I its moment of inertia with respect to the axis passing through the suspension point and perpendicular to the plane of motion. For small oscillations the natural angular frequency is $\omega_n^2 = (mgh_{cm} + k)/I \simeq mgh_{cm}/I$ and the effect of damping is expressed by the value of the dimensionless damping ratio $\zeta = \gamma/(2I\omega_n)$.

Let the suspension joint be subject to a tilt angle $\theta_{tilt}(t)$ around the axis perpendicular to the oscillation plane through the suspension point, and a tiltmeter be placed on the compound pendulum at distance h_1 from the suspension point capable to measure the instantaneous tilt angle of the pendulum relative to the local vertical. The equation of motion reads:

$$\ddot{\theta} + 2\zeta\omega_n(\dot{\theta} - \dot{\theta}_{tilt}(t)) + \omega_n^2\theta = -\frac{k}{I}(\theta - \theta_{tilt}(t)) \tag{4.14}$$

and the tilt signal measured by the tiltmeter is:

$$\frac{S}{g} = \frac{h_1}{g}\ddot{\theta} + \theta \tag{4.15}$$

From the Fourier Transform of (4.14) and (4.15) we obtain the transfer function between the tilt applied to the suspension of the pendulum and the signal measured by the tiltmeter on the pendulum:

$$T_{tilt} = \left|\frac{\hat{S}/g}{\hat{\theta}_{tilt}}\right| = \frac{(1 - \frac{\omega^2}{\omega_n^2}K)(\frac{k}{mgh_{cm}} + i2\zeta\frac{\omega}{\omega_n})}{1 - \frac{\omega^2}{\omega_n^2} + \frac{k}{mgh_{cm}} + i2\zeta\frac{\omega}{\omega_n}} \tag{4.16}$$

with

$$K = \frac{mh_{cm}h_1}{I} = \frac{mh_{cm}h_1}{mh_{cm}^2 + I_{cm}} \quad . \tag{4.17}$$

Fig. 4.6 plots T_{tilt} as function of frequency for various values of the damping ratio ζ.

In GGG $\frac{k}{mgh_{cm}} \simeq 2 \cdot 10^{-4}$, the constant K depends on the geometry of the system and its value is $K \simeq 0.87$. The pendulum natural frequency of the suspended part of GGG is $\nu_n \simeq 0.53$ Hz. It should be noticed that $T \to \frac{k}{mgh_{cm}}$ for $\omega \to 0$.

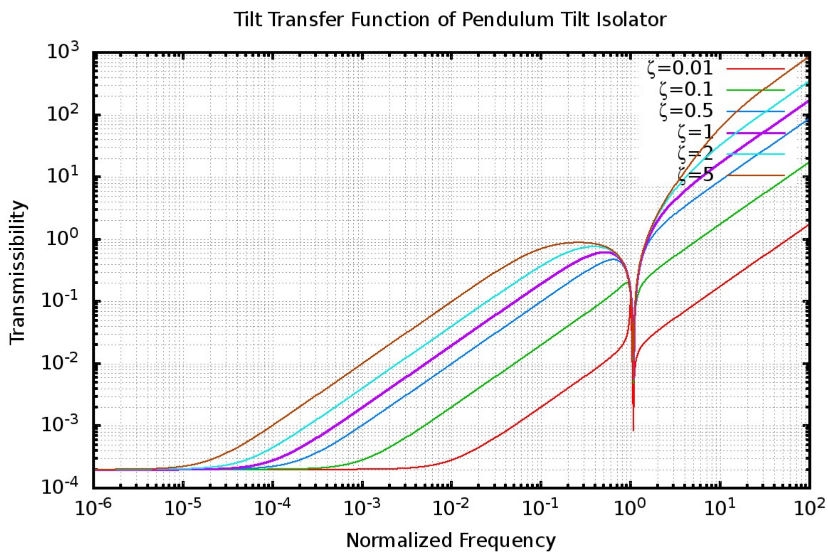

Figure 4.6: Transfer function between the applied tilt θ_{tilt} and the signal S/g measured by the accelerometer fixed to the pendulum at height h_1, for various values of the damping ratio ζ. $\zeta = 1$ is the critical damping. The parameters $\frac{k}{mgh_{cm}}$ and h_1 have been set as in GGG.

Consider now the case that the suspension joint is subject to an acceleration $a_x(t)$ along the x axis of the horizontal plane. A 1-axis accelerometer is connected to the compound pendulum at distance h_1 from the suspension point with its sensitive axis directed along the axis perpendicular to the pendulum axis (coincident with the horizontal axis x when the pendulum is in the vertical position).

The equation of motion of the pendulum under the effect of the horizontal acceleration $a_x(t)$ is:

$$\ddot{\theta} + 2\zeta\omega_0\dot{\theta} + (\omega_0^2 + k/I)\theta = -\frac{mh_{cm}}{I}a_x(t) \tag{4.18}$$

and the signal measured by the accelerometer on the pendulum is:

$$S = a_x + h_1\ddot{\theta} + g\theta \tag{4.19}$$

From the Fourier Transform of of (4.18) and (4.19) we can write the transfer function between the horizontal acceleration applied to the suspension of the compound pendulum and the signal measured by the accelerometer on it:

$$T_{hor-acc} = \left|\frac{\hat{S}}{-\omega^2\hat{a}_x}\right| = \left|\frac{\frac{\omega^2}{\omega_0^2}[K-1] + i2\zeta\frac{\omega}{\omega_0} + \frac{k}{mgh_{cm}}}{1 - \frac{\omega^2}{\omega_0^2} + \frac{k}{mgh_{cm}} + i2\zeta\frac{\omega}{\omega_0}}\right| \tag{4.20}$$

whose plot is shown in Fig. 4.7

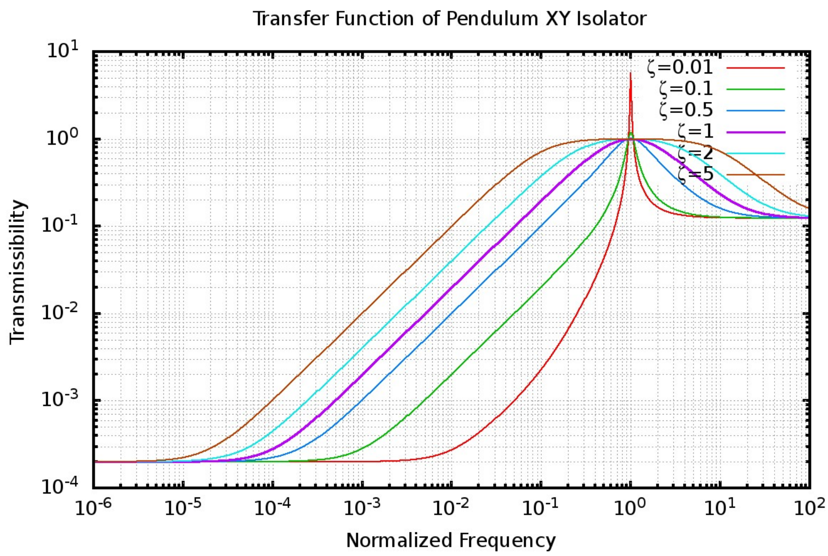

Figure 4.7: Transfer function between the horizontal accelerations $\ddot{X}$ of the body A and the signal S of the accelerometer fixed to the pendulum at height h_1, for various values of the damping ratio ζ. $\zeta = 1$ is the critical damping.

Note that if $a_x(t) = constant \equiv a$ and if we impose $\ddot{\theta} = 0$, $\dot{\theta} = 0$ (oscillations completely damped) from the equation of motion we get that the equilibrium angle is $\theta_{eq} = -\frac{a}{g+\frac{k}{mh_{cm}}} \simeq -\frac{a}{g}$ and the signal of the accelerometer is $S = a\frac{\frac{k}{mgh_{cm}}}{1+\frac{k}{mgh_{cm}}} \simeq a\frac{k}{mgh_{cm}}$.

Figs. 4.6 and 4.7 show that at low frequencies the response to tilts and to horizontal accelerations is the same and they cannot be distinguished.

4.4 Tilt and horizontal acceleration noise related to spin

In GGG it is important to consider also low frequency effects due to terrain and bearings tilt noise acting close to $2\nu_{spin}$. Recent SimMechanics simulations of GGG indicate that terrain and bearings tilt noise applied close to $2\nu_{spin}$ appears in the low frequency region.

Characteristics of the simulation: Simulation time=3000 s ($f_{min} = 3.33{\cdot}10^{-4}$ Hz), T_{diff}=18 s, ν_{spin}=0.19 Hz and k_c=0.11 Nm/rad. Tilt noise is applied only in the Y direction and it is a sinusoid with frequencies as reported in Fig. 4.8 and amplitude of 1 mrad.

Some observations from the simulation:

- Tilt noise close to $2\nu_{\rm spin}$ is downconverted to low frequency, but not tilt noise close to $\nu_{\rm spin}$ and $3\nu_{spin}$.
- The tilt rejection system with the capacitance plates on the top, works well for tilt noise at low frequencies but not for tilt noise close to $2\nu_{spin}$.
- Tilt noise close to $2\nu_{\rm spin}$ is applied only in one direction but when it is downconverted at low frequencies, it gives the same effect along X and Y.

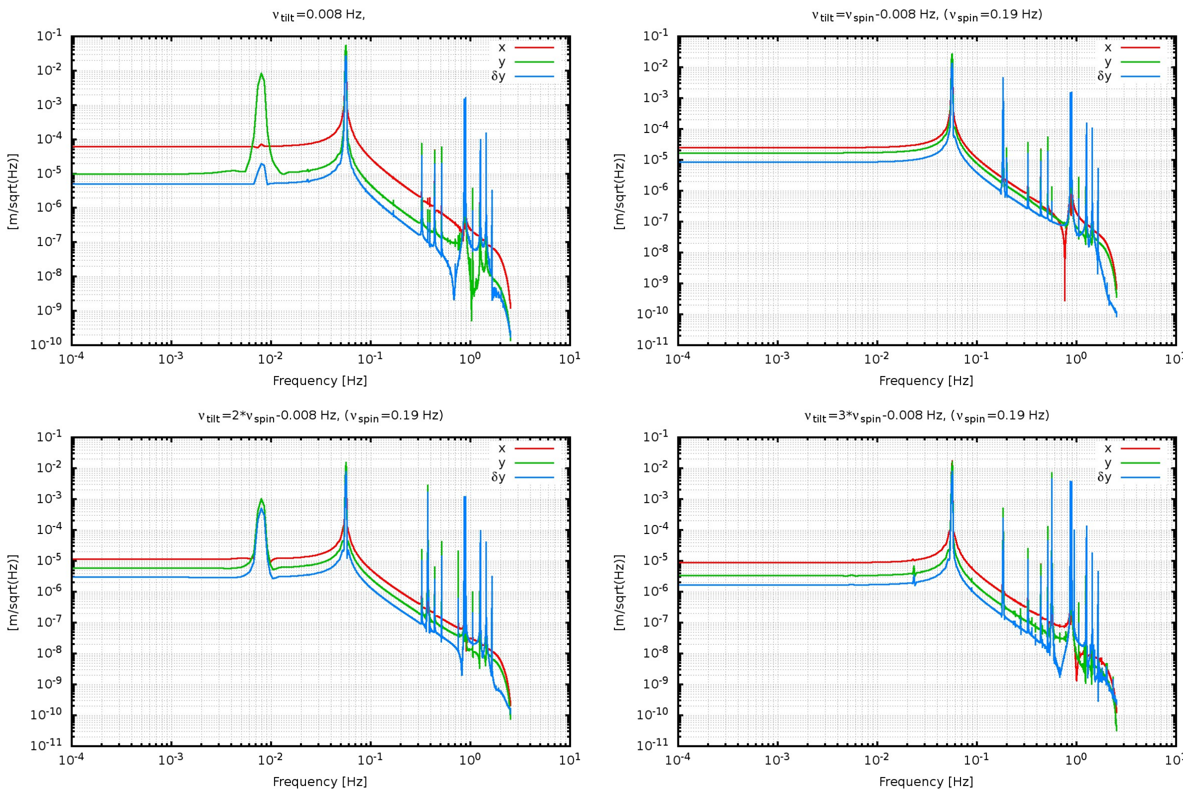

Figure 4.8: Simulation results: The effect of tilt noise at frequencies 0.008 Hz (top left), $\nu_{spin} - 0.008$ Hz (top right), $2\nu_{spin} - 0.008$ Hz (bottom left), $3\nu_{spin} - 0.008$ Hz (bottom right). Plots show the PSD of distance between the center of mass of the two test masses along X (red line) Y (green line) and the measurement with the "capacitance plates on the top of the experiment" used for tilt rejection (δy) blue line (see Subsec. 4.2.2). The amplitude of applied sinusoidal tilt is about 1 mrad and it is always applied along the Y direction only.

If this effect real and relevant can be mitigated as follows:

- Terrain tilts are known to have a minimum between 0.1 Hz and about 1 Hz, and can also be controlled pretty well actively because ordinary accelerometers to be used in the loop are reliable at these high frequencies
- Bearings tilts can be reduced by moving from ball bearings to air bearings (as in the slowly rotating torsion balances). An air bearing can reduce bearings noise on the rotating shaft (at all frequencies)

by more than 2 orders of magnitude compared to ball bearings and should also allow a better control of the rotation speed.

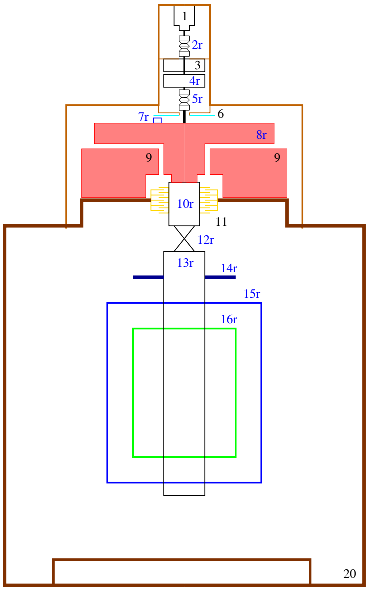

Figure 4.9: Air Bearing

4.5 Experimental measurement of passive tilt attenuation with a simple set-up

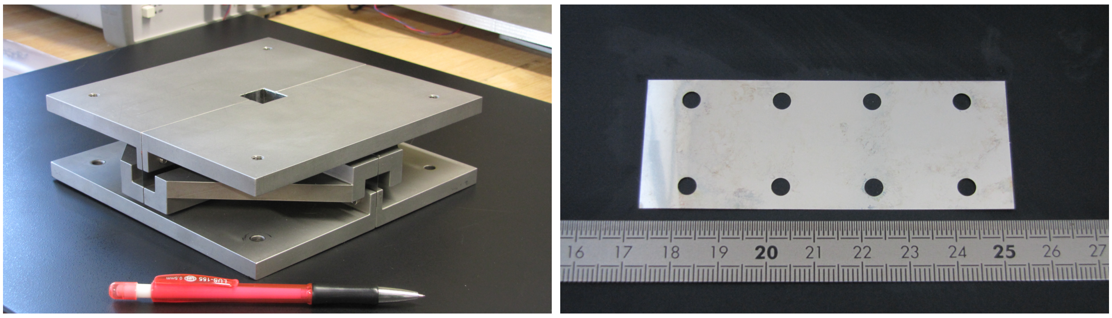

Figure 4.10: Passive laminar 2-D suspension and one of the steel blade (totally 4, 2 in each direction) used to suspend GGG. In this X-Y isolation suspension, two pairs of orthogonal membranes provide tilt isolation in both directions. The central connecting block of the suspension which cross clamps these orthogonal pair of steel membranes, so that they are at the same distance from the suspension point. The advantage of this configuration is that the length of pendulum is equal for both degrees of freedom.

In order to passively attenuate the low frequency ground noise on GGG accelerometer, an inexpensive laminar cardanic suspension has been originally designed (Fig. 4.10). The primary elements of this suspension are four rectangular steel blades. The first main consideration before designing any flexure is that the stress in the strip flexure ($S = Mg/bt$) must be very much less than the yield strength (Y) of the material. Otherwise we are destroying the elastic behaviour and entering into the plastic region. In GGG we are supporting with safe yield. This suspension consists of 3 blocks i.e. top, central and bottom one. Four steel blades, two in each direction are used to link these blocks. 2 blades are clamped in parallel between the top and central blocks in one direction and an another set of blades are clamped in parallel between central and bottom blocks in orthogonal direction, so that the laminar joint is free to move in 2D. The central block is designed in such a way that four blades occupy the same height (symmetrical in 2 directions) and 2 half joints are in perfect alignment, which can be easily seen from the Fig. 4.10.

The top block is mounted with the frame which is rigidly fixed on the base plate of the vacuum chamber. The bottom bock is fixed with the frame inside which the whole accelerometer is residing, which has to be suspended for passive tilt attenuation. The angular spring constants of these blades will decide the level of seismic attenuation on the GGG accelerometer. Prior to mounting it on the real system, we have to evaluate the angular spring constants and tilt reduction under realistic condition of load as in GGG. To assess them a simple experimental set-up as shown in Fig. 4.11 has been designed using one of the steel blade of the laminar joint.

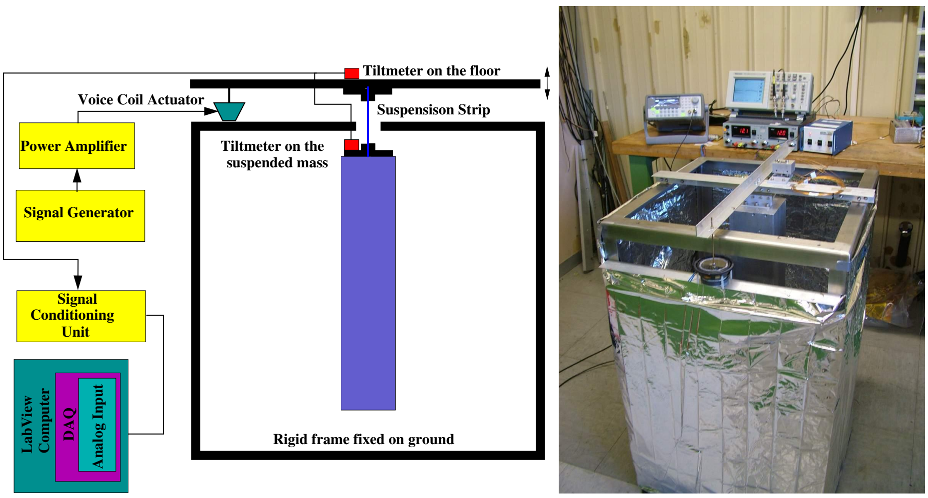

Figure 4.11: Schematic view of the experimental setup, DAQ arrangement and real set-up

This set-up is nothing but a compound pendulum [57 cm × 12 cm × 12 cm], in which a mass of 64 kg is suspended by the weak joint, which is the steel blade in our case. In this joint, we use the flex blades of 80 μm thick and 80 mm wide; the load on each of them is about 630 N for a resulting stress of 0.1 GPa which is small compared with the yield strength of the workshop steel. So we are supporting with 3.6% yield, hence we are safe. The concept is simple: apply a known tilt on the suspension point of the pendulum at a known frequency and measure the response of applied tilt on the suspended mass at the same frequency. The ratio of these two tilts will give us the tilt attenuation factor of the suspension. In this context the setup consists of an Iron block of 64 kg suspended by one of these steel blades. The other end of the blade is fixed with a thick steel strip. This strip has two knife edges at its ends which are sitting on a steel rectangular ground support. An Al strip is connected to the steel strip as shown in Fig. 4.11. A voice coil actuator fixed at the end of this Al strip is used to apply tilts at known frequencies. Two Geo-mechanics tilt meters mounted on the steel strip and on the suspended mass has been used to measure tilts. This whole setup is wrapped with an Al foil to reduce air currents on the system.

For this dynamical system we can easily show that the tilt attenuation factor χ_{tilt}, which is the ratio between attenuated tilt on the suspended mass ($\theta_{response}$) and applied tilt ($\theta_{applied}$) on the suspension point is simply given by

$$\chi_{tilt} = \frac{\theta_{response}}{\theta_{applied}} = \frac{k}{MgL + k} \tag{4.21}$$

where k is the angular spring constant of the joint, M is the suspended mass and L is the distance from the point of suspension to the center of the mass of the suspended body.

For $MgL \gg k$, we can write

$$\chi_{tilt} = \frac{\theta_{response}}{\theta_{applied}} \simeq \frac{k}{MgL} \tag{4.22}$$

FFT of two tilt meter signals will give us χ_{tilt}. Fig. 4.12 shows the FFT of two tilt meter signals. From this plot we can evaluate χ_{tilt} and for the suspended mass M of about 64 kg and L of 0.31 m. Under these experimental parameters we have measured tilt reduction factor χ_{tilt} of about 1/12000. The dimensions of the steel blade, elastic properties and measured tilt reduction factor χ_{tilt} are tabulated in Table 4.1.

Table 4.1: Laminar blade dimensions and experimentally measured tilt reduction factor χ_{tilt}

Dimensions	Measured χ_{tilt}
Thickness (t) = 80 μm	
Flexible length (l) = 10 mm	≈1/12000 (Fig. 4.12)
Width (b) = 80 mm	
Suspended mass (M) = 64 kg	
Young's Modulus (E)=180 − 200 Gpa=(1.8 − 2.0) × 10^{11} N/m^2	
Yield strength (Y)=2.8 Gpa=2.8 × 10^9 N/m^2	

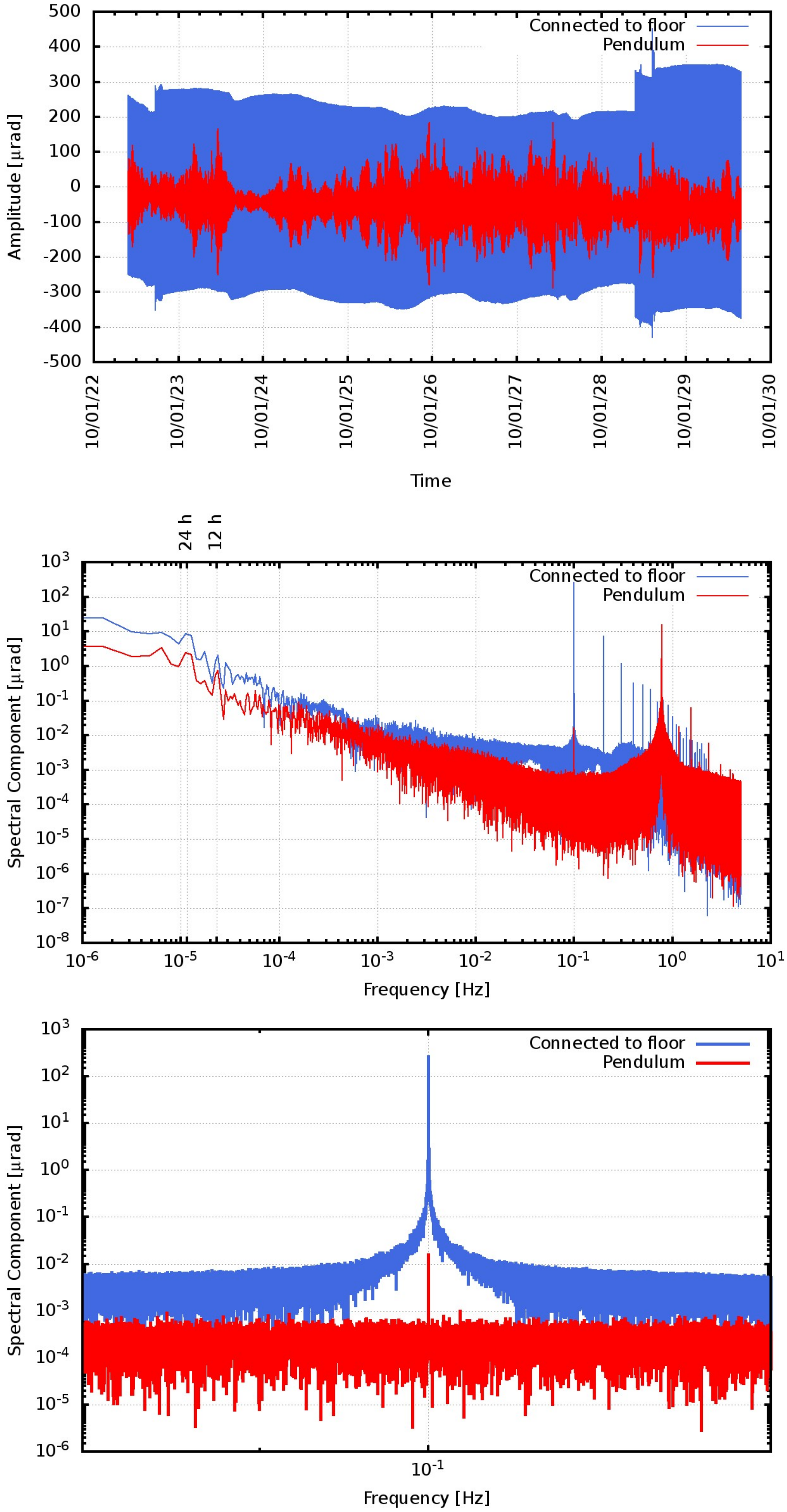

Figure 4.12: Time Series, FFT of the tilt meter signal and a plot shown with magnification of the FFT plot at 0.1 Hz applied tilt frequency. In blue we see the signal of the top tiltmeter (rigid with floor, hence sensitivie to full terrain tilts) on which the 0.1 Hz forcing tilt signal is applied. In red we see the signal measured by the tiltmeter on the suspended pendulum, clearly smaller. Tilt reduction factor χ_{tilt} is about 1/12000. Note that the peak at 0.7752 Hz (1.290 s) is due to the natural frequency of the pendulum.

4.6 Laminar flexure joints: comparision between theory and experiment

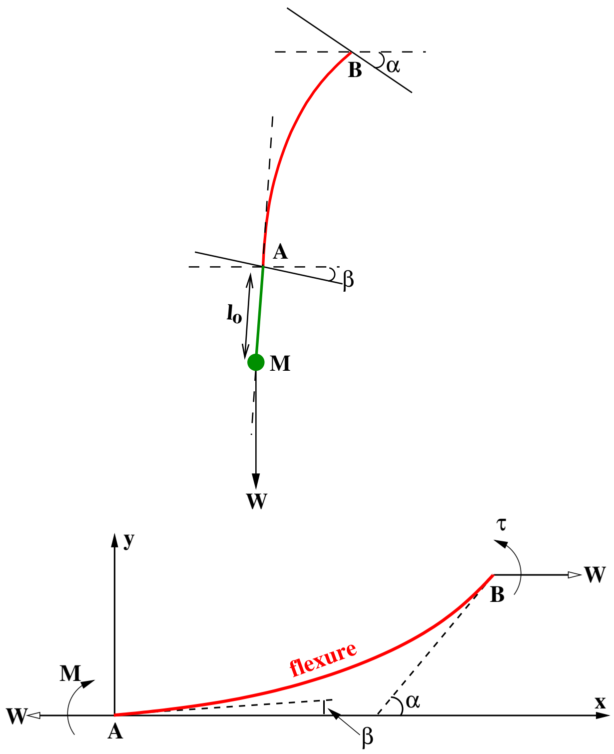

Figure 4.13: Top: Schematics of the effect of tilt on the flexure Bottom: Coordinate system as used in the text.

Now let us consider the mass M is suspended by using the strip flexure as shown in Fig. 4.13. The centre of mass is at a distance l_0 from the end of the flexure of length l. This figure illustrates schematically a ground tilt of a amplitude α at B, inducing a deflection β of the suspended mass at A. Fig. 4.13 also shows the coordinate system used, where M and τ are the moment of the centre of mass about A and moment about B required to produce tilt are given as:

$$M = Wl_o\beta \tag{4.23}$$

$$\tau = \frac{W\alpha}{\lambda\tanh(\lambda l)} - \frac{W\beta}{\lambda\sinh(\lambda l)} \tag{4.24}$$

Quinn [2] showed that the tilt attenuation factor χ_{tilt} which is the ratio between the amplitude of attenuated tilt on the suspended mass at A and the amplitude of ground (applied) tilt α on the suspensioin point B is given by

$$\chi_{tilt} = \frac{\beta}{\alpha} = \frac{1}{\lambda l_0\sinh(\lambda l) + \cosh(\lambda l)} \tag{4.25}$$

As shown already (4.22), we can also express the tilt attenuation factor in terms of an effective spring constant k:

$$\chi_{tilt} = \frac{\beta}{\alpha} \simeq \frac{k}{Mgl_0} \tag{4.26}$$

By comparing (4.26) and (4.25) we can arrive

$$k = Mgl_0\chi_{tilt} = Mgl_0\,\frac{1}{\lambda l_0\sinh(\lambda l) + \cosh(\lambda l)} \tag{4.27}$$

Figs. 4.14 and 4.15 show the expected and measured k and tilt attenuation factor χ_{tilt} for the strip of $t = 80\,\mu\text{m}$, $l = 10\,\text{mm}$, $b = 80\,\text{mm}$ and suspended mass at a distance of $l_0 = 31\,\text{cm}$ for the suspended mass M of 64 kg. These are the real conditions of the experiment conducted in the previous Sec. 4.5.

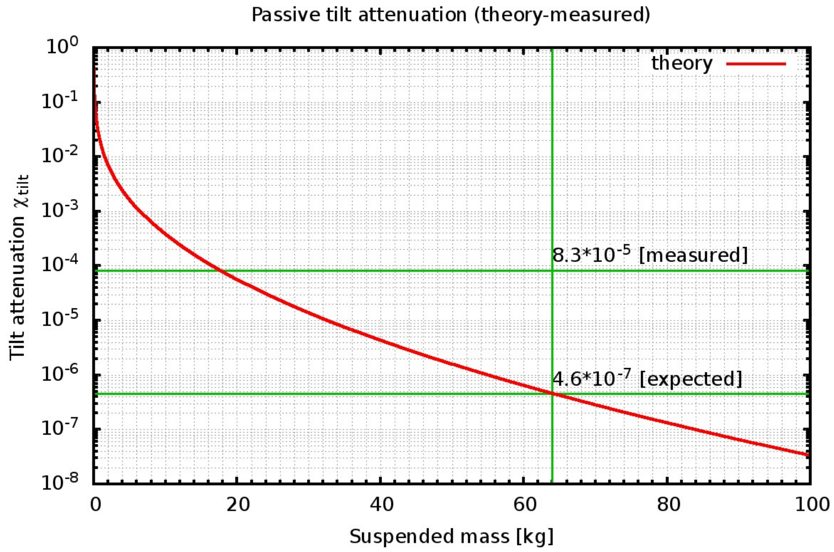

Figure 4.14: Estimated tilt attenuation factor χ_{tilt} by using (4.25) for the strip of $t = 80\,\mu\text{m}$, $l = 10\,\text{mm}$, $b = 80\,\text{mm}$ and suspended mass at a distance of $l_0 = 31\,\text{cm}$ as a function of suspended mass M. These are the real conditions of the experiment conducted in the previous Sec. 4.5.

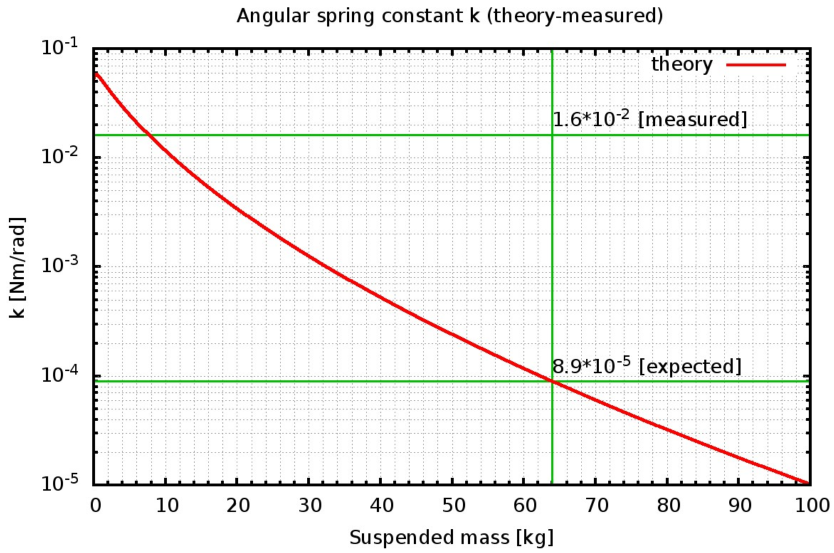

Figure 4.15: Estimated angular spring constant k by using (4.27) for the strip of $t = 80\,\mu\text{m}$, $l = 10\,\text{mm}$, $b = 80\,\text{mm}$ and suspended mass at a distance of $l_0 = 31\,\text{cm}$ as a function of suspended mass M. These are the real conditions of the experiment conducted in the previous Sec. 4.5.

Experimentally obtained tilt reduction is about 2 orders lower than theoretically expected. The reason why we were not able to obtain the theoretically expected tilt attenuation factor and the degradation which was observed in GGG passive tilt attenuation (Sec. 4.7) are explained as follows: due to poor clamping, at some point the flexure is only sustained by the screws which are used to clamp the flexures with blocks. So the flexures are no more rigid with blocks. Due to this, the stress is accumulated between holes as shown in Fig. 4.16 (red lines between holes). The cross sectional view shows that the effect of stress accumulation. So the flexure gets undulations (which was observed by carefull commissioning) along its cross section, which completely degrades k hence χ_{tilt}. This effect can be mitigated by very careful clamping and manipulating, but it can be avoided only by using a monolithic 2D joint (similar to those used for the test cylinders) also for tilt attenuation, as described in Sec. 4.2.

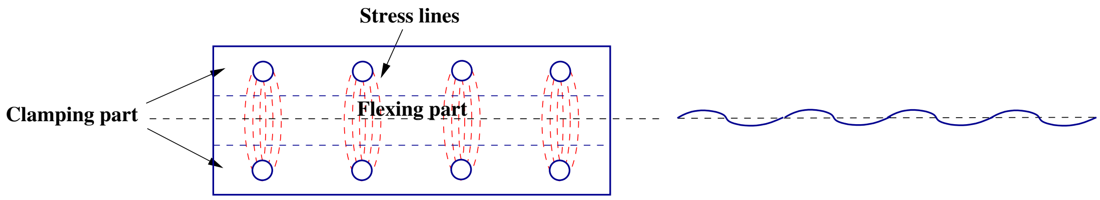

Figure 4.16: Stress accumulation on flexures and its effect along cross section of the flexure

4.7 GGG: a procedure for the measurement of low frequency tilt attenuation

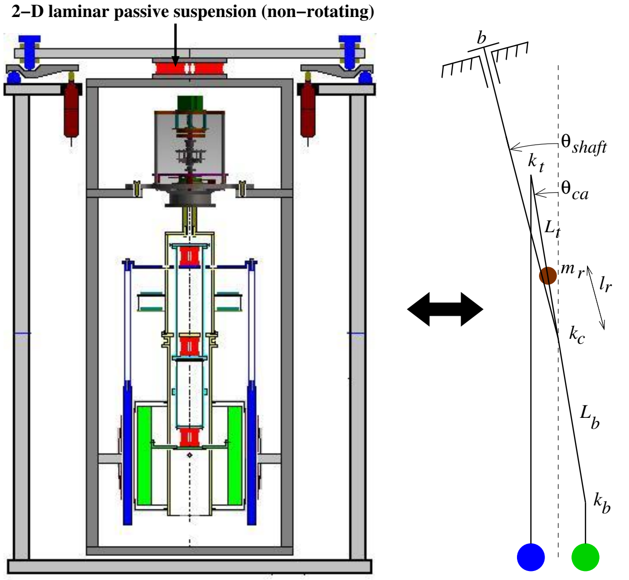

Figure 4.17: GGG suspended using laminar joint for passive tilt attenuation

Having performed and checked the performance and passive tilt attenuation level of steel flexures with the simple set-up, we implemented the passive laminar joint on GGG to measure the performance. At the time of the measurement the frame inside which the GGG differential accelerometer is mounted was weakly suspended from this laminar 2D joint (not rotating) (see Fig. 4.17) attached to the top flange rigidly connected to the vacuum chamber. The weak laminar joint in CuBe below the ball bearings was not installed at the time.

We measured the tilt sensitivity of GGG by applying a sinusoidal tilt to the upper plate and then measure the tilt on the Suspended Frame (SF) and the differential displacement between the GGG test masses. The experiment was not rotating. We expect (from theory, numerical simulations and measurements so far) no difference in tilt attenuation when the system rotates.

The frequency of the sinusoidal tilt signal applied to the upper plate was 10 mHz; its amplitude about 10 μrad. The amplitude of the tilt measured on the suspended frame was about 2 nrad, see the plot of Fig. 4.18. The tilt attenuation provided by the suspension of the frame is then $\chi_{SF} \simeq 1/5000$ in this frequency region. This good level of attenuation in the low frequency is as expected from the theoretical transfer function.

Unfortunately when we performed the same type of measurement after couple of days, there was a degradation in the attenuation level most probably due to the flexures degradation discussed above. This time the frequency of the sinusoidal tilt signal applied to the upper plate was the same 10 mHz; now its amplitude was about 22 μrad. The amplitude of the tilt measured on the suspended frame was about 70 nrad, see the plot of Fig. 4.19. So the tilt attenuation provided by the suspension of the frame is then $\chi_{SF} \simeq 1/300$ in this frequency region. A thorough investigation on the suspension revealed us that this degradation in the low value of the measured tilt attenuation with respect to the expected and measured value has been found to be due to deformations of the elastic joint from which the experiment has been suspended as discussed already. These deformations is due to an inappropriate clamping mechanism of the 80 μm thick steel foil flexures. This effect of degradation due to clamping is inevitable. So, a CuBe joint, manufactured by extro erosion from a single block of material has been manufactured to avoid such problems. As shown in Sec. 4.2 this joint is located on the shaft (rotating with it) below the bearings, so that bearing noise will be attenuated too. This monolithic joint is expected to have better mechanical quality and lower k to provide better tilt attenuation at low frequencies (see Ch. 5).

In Fig. 4.20, we report the measured differential displacement between the GGG test masses as seen

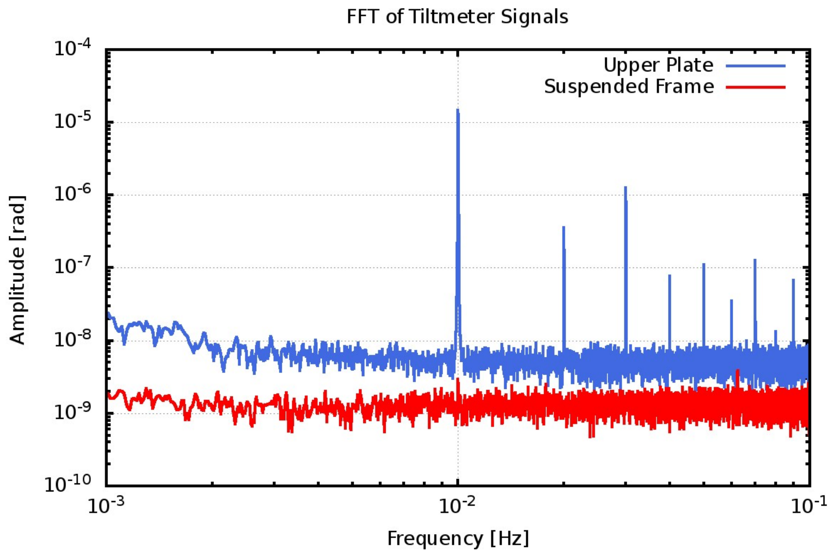

Figure 4.18: FFT of tilt meters signals measuring the applied tilt on the upper plate and the transmitted tilt on the suspended frame. The amplitude of the sinusoidal 10 mHz tilt signal applied to the upper plate is 10 μrad; the corresponding tilt amplitude measured on the suspended frame is 2 nrad. The tilt attenuation provided by the suspended frame in this frequency region is then about a factor 1/5000.

by the χ and ψ bridges that have been placed in the angular position sensitive to the applied tilt for two different measurements. It can be seen that the amplitude of the peak at 10 mHz is about 13 nm in the χ direction and 80 nm in the ψ direction. From these measurements we conclude that the 22 μrad tilt applied to the upper plate corresponds to a GGG test masses differential displacement of 13 nm in the χ direction and 80 nm in the ψ direction; that is the sensitivity of the non–rotating GGG experiment to floor tilts is $5.9 \cdot 10^{-4}$ m/rad in the χ direction and $3.6 \cdot 10^{-3}$ m/rad in the ψ direction.

The tilt amplitude transmitted to the isolated suspended frame is 70 nrad; hence the non–rotating GGG differential test masses displacement sensitivity to suspended frame (that is the shaft) tilt is 0.18 m/rad in the χ direction and 1.15 m/rad in the ψ direction, corresponding to a 0.49 rad/rad in χ and 3.14 rad/rad in ψ coupling arm tilt (of length $L = 0.183$ m) to shaft tilt sensitivity. Table 4.2 reports the differential periods and tilt sensitivities as measured from the FFT reported in Fig. 4.20; Table 4.3 reports the measured tilt attenuation factor as provided by the Suspended Frame and the non–rotating GGG sensitivity to tilts expressed in terms of the differential displacement between the test masses.

$T_{\chi diff}$	$\chi_{\theta\chi}$	$\chi^{da}_{\theta\chi}$	$\chi_{cma\chi}$
8.073 s	0.47 rad/rad	$0.11\,\mathrm{ms^{-2}/rad}$	$1.1 \cdot 10^{-2}\ \mathrm{ms^{-2}/ms^{-2}}$
$T_{\psi diff}$	$\chi_{\theta\psi}$	$\chi^{da}_{\theta\psi}$	$\chi_{cma\psi}$
16.285 s	3 rad/rad	$0.17\,\mathrm{ms^{-2}/rad}$	$1.7 \cdot 10^{-2}\ \mathrm{ms^{-2}/ms^{-2}}$

Table 4.2: Measured non–rotating GGG differential periods and tilt sensitivities along the χ and ψ directions. ("*da*": differential acceleration; "*cma*": common mode acceleration)

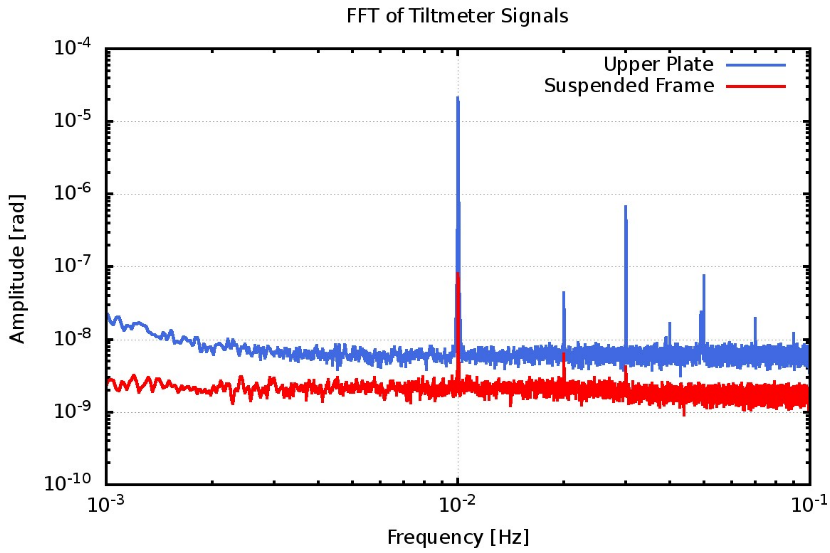

Figure 4.19: FFT of tilt meters signals measuring the applied tilt on the upper plate and the transmitted tilt on the suspended frame. The amplitude of the sinusoidal 10 mHz tilt signal applied to the upper plate is 22 μrad; the corresponding tilt amplitude measured on the suspended frame is 70 nrad. The tilt attenuation provided by the suspended frame in this frequency region is then about a factor 1/300.

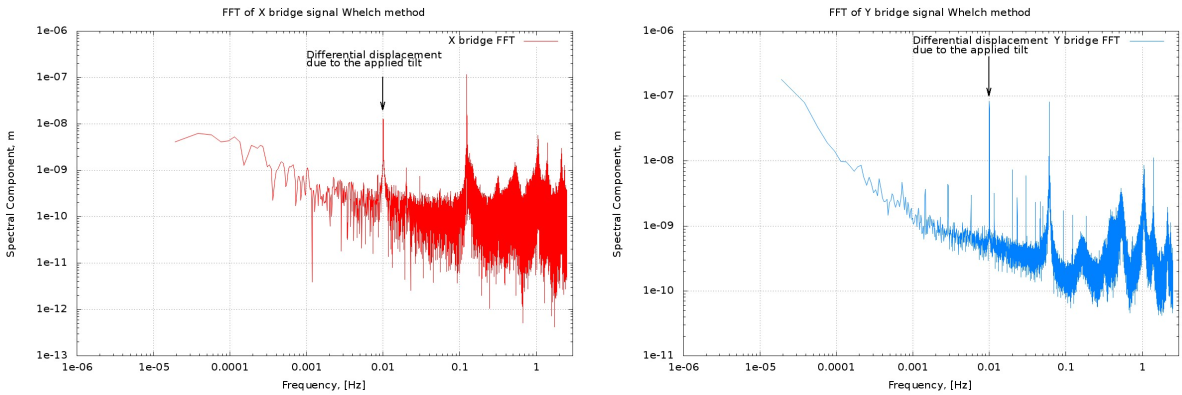

Figure 4.20: FFT of the GGG χ and ψ bridge signals sensitive to the applied tilts when the experiment is not rotating. The amplitude of the peak at 10 mHz is about 13 nm in the χ direction and 80 nm in the ψ direction.

GGG Tilt Sensitivity along χ		
χ_{SF}	Displacement Sens. wrt Floor Tilt	Displacement Sens. wrt Susp. Frame Tilt
1/300 rad/rad	$5.9 \cdot 10^{-4}$ m/rad	0.18 m/rad
GGG Tilt Sensitivity along ψ		
χ_{SF}	Displacement Sens. wrt Floor Tilt	Displacement Sens. wrt Susp. Frame Tilt
1/300 rad/rad	$3.6 \cdot 10^{-3}$ m/rad	1.15 m/rad

Table 4.3: Measured tilt attenuation provided by the Suspended Frame (SF), sensitivity of the non–rotating GGG experiment to tilt applied in the χ and ψ directions.

References

[1] R. Pegna, A. M. Nobili, T. R. Saravanan *et al.*, "Attenuation and rejection of vibration noise in the GGG rotating differential accelerometer", in preparation

[2] T. J. Quinn *et al.*, Metrologia 23, 87-100, (1986/87)

Chapter 5

The GGG laminar 2D suspensions

5.1 The design

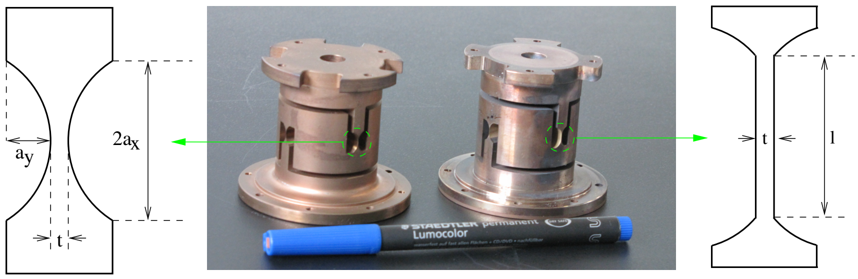

Figure 5.1: Laminar suspensions in the GGG experiment. Left: Elliptical Flexures-Old design Right: Rectangular Flexures-New design

GGG monolithic cardanic suspensions have been obtained by electrical discharge machining (EDM) from a single block of CuBe alloy. This wire EDM is a method to cut conductive materials with the help of a thin electrode that follows a computer controlled path. This electrode is a thin wire with a diameter ranging from 50 to 300 μm. The nominal accuracy of machining is of the order of 5 μm. The hardness of work material has no detrimental effect on the cutting precision because there is no physical contact between the wire and the part being machined. The wire is immersed in de-ionized water and is charged at high voltage until a spark jumps the gap and erodes a small portion of the work piece. The de-ionized water cools and flushes away the removed particles from the gap.

Beryllium-copper (CuBe) alloy has been chosen because it has a good thermal stability by having the coefficient of thermal expansion $17 \cdot 10^{-6}$ K^{-1}, it is not magnetic, its intrinsic loss angle ϕ is about 10^{-4} and its yield strength ranges from 500 MPa to 1300 MPa if the material is precipitation hardened (baked at 315°C for 2 hours). The high thermal conductivity allows to reduce drifts in the accelerometer output due to thermal gradients. Another peculiarity of the precipitation hardened materials is that they maintain their mechanical properties even with applied stresses close to the yield point; for CuBe no changes in the loss-angle have been observed up to 95% of the yield stress [1]. Table 5.1 gives the manufacturer's quoted CuBe physical properties.

These cardanic suspensions are designed in such a way that they support the load against gravity and allow the test masses to move in 2D (see Fig. 5.1). Every suspension has two couples of coaxial flexures, one pair for each direction. The middle part of the suspension cross connects these orthogonal pair of flexures, so that they are at the same distance from the suspension point. The two pairs of orthogonal flexuress provide weak coupling in the two directions of the horizontal plane and are extremely rigid in the vertical direction. Two versions of the GGG joints are discussed here, whose difference in the flexures design is shown in Fig. 5.1.

Table 5.1: CuBe physical properties. E is the Young's modulus, Y is the yield strength, α is the coefficient of linear thermal expansion and c_w is the thermal conductivity.

E (GPa)	Y (MPa)	α ($\times 10^{-6}$/K)	c_w (W/cm-K)
120	500	17	1.51

5.2 On-bench measurements and performance

In the GGG rotor there are three cardanic joints: the central one suspends the coupling arm of the balance from the rotating shaft, the top and bottom ones suspend the outer and inner test cylinder respectively from the two ends of the coupling arm. A fourth joint is located on the shaft, below the ball bearings, in order to attenuate microseismic terrain noise as well as bearings tilt noise. The old version of joints have elliptical flexure geometry. All the joints share the same design geometry except for the thickness and width. Since these joints govern the dynamics (natural coupling frequencies of the test masses, common mode force rejection and immunity to ground noise) of the rotor, it is essential to have a well accepted theoretical model and an on-bench experimental method to evaluate their angular spring constants. We have therefore designed a simple experimental set-up to measure them.

The angular spring constant can be modeled using the Tseytlin formula [2],

$$k_\theta = \frac{Ebt^2}{16\left[1+\sqrt{1+0.215\,(2R_e/t)}\right]} \tag{5.1}$$

$$R_e = \epsilon a_x = a_x^2/a_y \tag{5.2}$$

$$\epsilon = a_x/a_y \tag{5.3}$$

$$\beta_e = t/2a_x \tag{5.4}$$

where E is the Young's modulus of the material, b is the width of the flex joint, t is the thickness at the center, R_e is the radius of curvature ϵ is the hinge ellipticity and β_e is the relative thickness of the elliptical hinge as shown in Fig. 5.1 [Left]. This expression is strongly recommended for thin elliptical hinges and it is also in good agreement with finite element analysis (FEA) models.

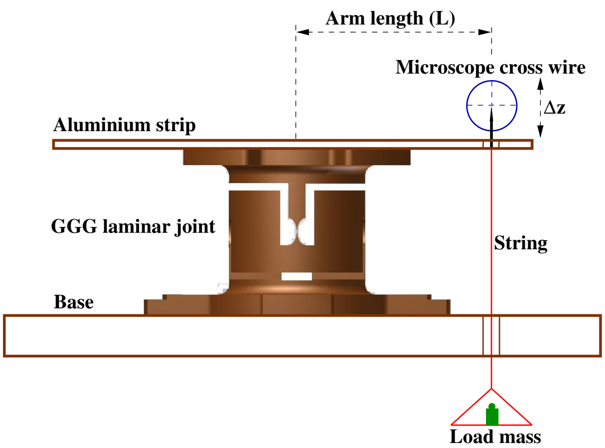

Figure 5.2: Angular spring constant measurement set-up

The experimental set-up is sketched in Fig. 5.2. The bottom part of the joint is rigidly fixed on the table and a weightless Al bar is rigidly fixed on the top part of the joint hence the central part is the flexible portion of the joint. Angular stiffness is evaluated by placing known masses m ranging from 1 to 8 gram onto the Al bar at known arm length L and noting the subsequent vertical displacements Δz as measured by the vernier caliper. Considering that this configuration refers to an inverted pendulum, the total or effective angular spring constant k is given by,

$$k = k_\theta - k_g \tag{5.5}$$

where k_θ is the angular spring constant of the flexible joint and k_g is contribution due to gravity and they are given as

$$k_\theta = \frac{mgL}{\Delta\theta} \tag{5.6}$$

m is the added mass and $\Delta\theta$ is given as:

$$\Delta\theta = \frac{\Delta z}{L} \tag{5.7}$$

therefore, k_θ can be written as:

$$k_\theta = \frac{mgL^2}{\Delta z} \tag{5.8}$$

and k_g is given as:

$$k_g = Mgh \tag{5.9}$$

where M is the total mass of the elements above the center of the joint respectively. h is the distance from the center of the joint to the center of mass of the entire elements above it.

Table 5.2 lists the (nominal) numerical values of the geometrical parameters for all four joints (in the two directions of the plane). Table 5.3 gives the predicted value of k_θ, along with the measured one for all four joints in each direction of the plane.

Table 5.2: GGG Joints and their dimensions (old design)

Joint	Thickness (t) (μm)	Width (b) (mm)	a_x (mm)	a_y (mm)	ϵ	R_e (mm)	β_e
Top and Bottom (χ, ψ)	90	30	4	2.455	1.629	6.52	0.011
Central (χ)	120	30	4	2.440	1.639	6.56	0.015
Central (ψ)	130	30	4	2.435	1.643	6.57	0.016
Below bearing (χ, ψ) (Seismic Attenuation)	90	13.8	4	2.455	1.629	6.52	0.011

Table 5.3: Angular spring constants of the GGG joints (old design)

Joint	Direction	Theoretical (k_θ) (5.1) (Nm/rad)	Experimental (k_θ) (Nm/rad)
Top	(χ)	0.273	0.26±0.01
	(ψ)	0.273	0.38±0.01
Bottom	(χ)	0.273	0.34±0.01
	(ψ)	0.273	0.33±0.01
Central	(χ)	0.545	0.59±0.01
	(ψ)	0.659	1.14±0.01
Below bearing	(χ, ψ)	0.126	0.17±0.01

5.3 Improved design and results from measurements

In GGG we have recently adopted a new design of flexure geometry (strip flexure instead of elliptical flexure) for the following reasons:

- The four weak joints used in the GGG balance namely the top, bottom, central joints and the joint below bearing hold different loads. The top and bottom joints suspend 10 kg each; the central joint suspends about 20.5 kg, the joint below the bearings suspends about 41 kg. The theoretical expression (5.1) we have used to evaluate k_θ is in agreement with the on-bench measurement under no load. The effect of load on the elastic constant is important but apparently it has not been investigated in the case of elliptical hinge flexures.
- We need weaker joints in order to increase the natural differential period of the test cylinders so as to get higher sensitivity. We also need a weaker joint in order to reduce tilt noise. With the elliptical hinge flexures of the old design this can be achieved only by reducing the thickness t of the flexures, which is quite hard. Instead, with the new flexure design we can play also with the length l of the flexure (see Fig. 5.1) to reduce the stiffness.

Basic theory of strip flexures: Since there is a well accepted theoretical model for rectangular strip flexures under load is available and it is in good agreement with experiments, we have chosen this flexure design. The model used to design the new GGG laminar joints is the following. Consider the flexure as shown in the Fig. 5.3 suspended by load W at its end.

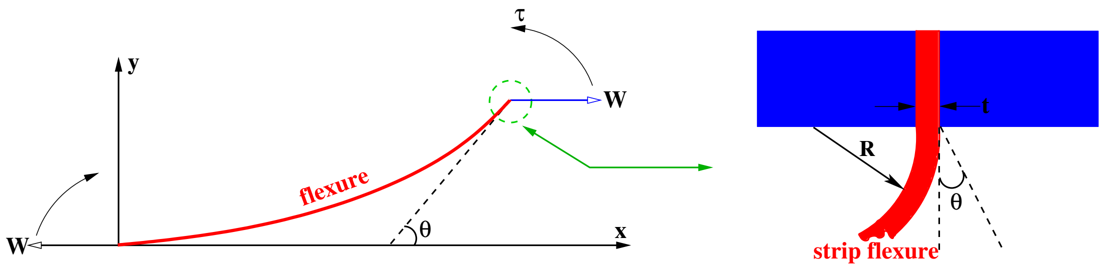

Figure 5.3: (left) Coordinate axes representation of the bending of a flexure for a torque of τ when under a load W. (right) Magnified portion of lower end of the flexure (junction).

If a torque τ is applied at the lower end of a flexure strip under tension, according to Terry Quinn [3], the resulting deflection angle θ is given by

$$\theta = \frac{\lambda \tanh(\lambda l)}{W}\tau \tag{5.10}$$

where l is the length of the flexure and λ is given by

$$\lambda = \sqrt{\frac{W}{EI}} \tag{5.11}$$

where E is the Young's modulus and ($I = bt^3/12$) is the cross-section moment of inertia for a rectangular strip of width b and thickness t. The resulting elastic constant of the strip is:

$$k_\theta = \left(\frac{WEbt^3}{12}\right)^{\frac{1}{2}} \coth\left[\left(\frac{12W}{Ebt^3}\right)^{\frac{1}{2}} l\right] \tag{5.12}$$

This expression is the sum of two contributions:

- One is due to the elastic energy stored in a flexure when a bending torque is applied to one end (not taking into account the restoring torque of the suspended mass). It is given by:

$$k = (WEI)^{\frac{1}{2}} \ \mathrm{cosech}(\lambda l) \tag{5.13}$$

  Thus the stiffness of the strip alone is an exponentially decreasing function of λl. This is to be expected: the longer is the strip, the easier it is to bend it.

- A second contribution k_g comes from the gravitational restoring torque due to the suspended mass. Gravitational restoring torque due to the suspended mass adds a second term k_g. If the centre of mass of the suspended load is at the end of the flexure it is:

$$k_g = WR \tag{5.14}$$

where R is the effective radius of curvature as shown in Fig. 5.3 (left). From this figure, we can write:

$$y = \frac{\theta}{\lambda} \tanh(\lambda l/2) \tag{5.15}$$

$$y = R\theta \tag{5.16}$$

with

$$R = \frac{\tanh(\lambda l/2)}{\lambda} \tag{5.17}$$

hence

$$k_g = \frac{W}{\lambda} \tanh(\lambda l/2) \tag{5.18}$$

The total stiffness k_θ is therefore

$$k_\theta = k + k_g \tag{5.19}$$

$$k_\theta = (WEI)^{\frac{1}{2}}\ [\tanh(\lambda l/2) + \mathrm{cosech}(\lambda l)] = (WEI)^{\frac{1}{2}}\ \coth(\lambda l) \tag{5.20}$$

and finally, by substituting the expressions given above for I and λ, we get (5.12) which is the correct theoretical formula for the elastic constant of a loaded strip flexure.

From (5.12) it is apparent that we can reduce the stiffness k_θ as follows:

- By making the thickness t of the suspension as small as possible, considering the fact that the stress in the strip flexure ($\sigma = \frac{Mg}{bt}$) must be much smaller than the Yield strength (Y) of the material. Otherwise we are destroying the elastic behavior and entering into the plastic region
- By making the ratio (l/t) just large enough for the hyperbolic cotangent to be closer to its minimum value of unity. (But increasing l further has little effect on decreasing the value of k_θ)

For $(l\lambda) > 3$ it is $\coth(l\lambda) \sim 1$. This condition gives the maximum length for the strip above which there is no further reduction of the spring constant (see [4], [5], [6], [7]). Under these conditions (5.12) becomes,

$$k_\theta = EI\lambda = \sqrt{MgEI} \tag{5.21}$$

Adopted design geometries for the GGG suspensions

1. **Joint on the shaft for tilt attenuation:** As already discussed in Ch. 4, in the case of rectangular flexure with suspended mass, the tilt attenuation factor χ_{tilt} is given by

$$\chi_{tilt} = \frac{\beta}{\alpha} = \frac{1}{\lambda l_0 \sinh(\lambda l) + \cosh(\lambda l)} \tag{5.22}$$

In Fig. 5.4 we report the angular tilt attenuation provided by the laminar joint on the shaft of GGG as a function of the joint length l, with a joint thickness t = 70 μm width b = 30 mm and $l_0 = 0.45$ m, by using the above expression. The stress on the suspension is $\sigma = \frac{\mathrm{M}g}{\mathrm{bt}} \simeq 187$ N/mm^2 for a suspended mass of M $\simeq$ 40 kg, to be compared with the Yield strength $Y = 500$ N/mm^2 of CuBe. We have chosen a joint length of $l = 3$ mm giving a tilt attenuation of 10^{-5}.

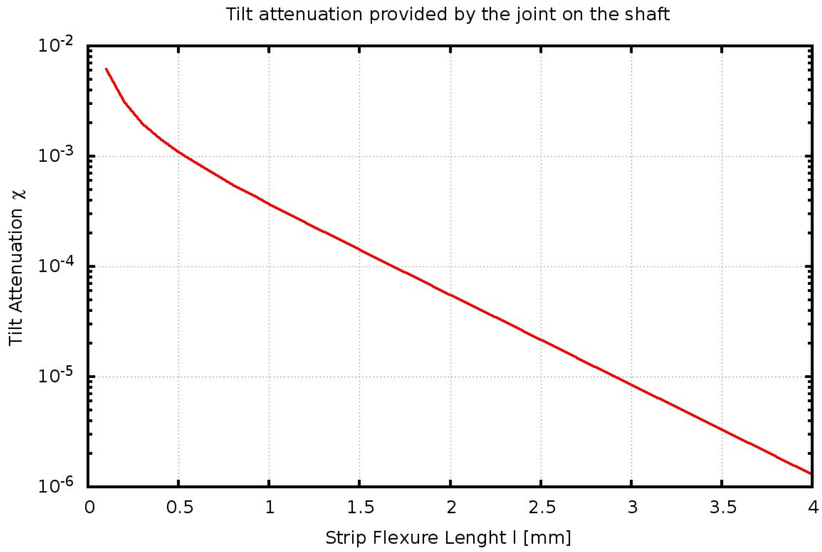

Figure 5.4: Tilt attenuation provided by the joint located on the rotating shaft of GGG for a suspended mass of M $\simeq$ 40 kg suspended at a distance of $l_0 = 0.45$ m, as a function of the strip flexure length l, with a strip thickness t = 70 μm and a width $b = 30$ mm.

2. **GGG balance central joint:** As demonstrated in the Subsec. 4.2.2 of Ch. 4, the rejection of tilt noise depends mainly on the angular spring constant k_c of the central joint. By making it lower we can reject the tilts as well as increase the differential period of the GGG balance. As already shown, the differential period of the GGG balance with the condition that the arm balance follows the tilt of the shaft ($\chi_\theta \simeq 1$) is given by:

$$T_{d\,(\chi_\theta \simeq 1)} \simeq 2\pi \sqrt{\frac{m_t L_t^2 + m_b L_b^2 + m_r l^2}{k_c}} \tag{5.23}$$

By using the expression (5.12), in GGG with $m_t = m_b \simeq 10$ Kg $L_t = L_b = 0.183$ m and with expected $k_c \simeq 0.11\,\mathrm{Nm/rad}$ (as in the plot of Fig. 5.5) we will obtain $T_{d\,(\chi_\theta \simeq 1)} \simeq 15$ s. It is evident from Fig. 5.5 that the the angular spring constant does not decrease significantly for $l > 1.5\,\mathrm{mm}$. The stress on the suspension is $\sigma = \frac{\mathrm{M}g}{\mathrm{bt}} \simeq 110$ N/mm^2 for a suspended mass of M $\simeq$ 20 kg, well within the safety limit given by the Yield strength. We have chosen a joint length of $l = 3$ mm, thickness t = 80 μm and width $b = 30$ mm.

3. **GGG balance top and bottom joint:** The same design geometry has been adopted as in the case of the central joint of the GGG balance.

4. **Test joints:** Before choosing the final manufacture design of the GGG joints three test joints have been manufactured with the same length $l = 1.5$ mm, width b = 30 mm, and different thickness

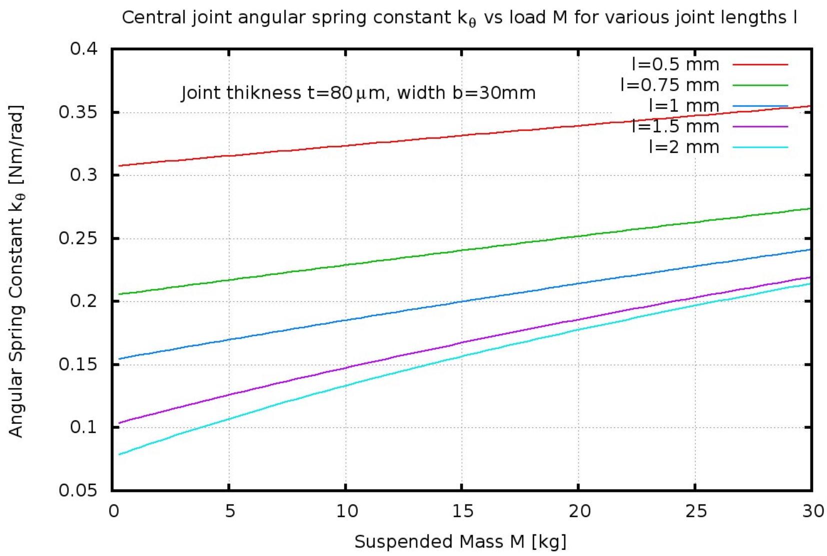

Figure 5.5: Angular spring constant of the central joint as a function of the suspended mass M, for various values of the length l of the laminar part, for a thikness t = 80 μm and a width b = 30 mm.

$t_1 = 50$ μm, $t_2 = 60$ μm and $t_3 = 70$ μm (see Fig. 5.6). The joint with 50 μm thickness was damaged during transportation. We have set-up an experiment to measure their spring constants. We have measured the elastic constant k_θ of the test joints with a static and a dynamic method, and have compared the results with the theoretical prediction.

Before go for final manufacturing of GGG joints, three test joints (see Fig. 5.6) have been designed and manufactured for testing. These joints have equal lengths l = 1.5 mm and width b = 30 mm (the same width as in the central joint) and three different thiknesses $t_1 = 50$ μm, $t_2 = 60$ μm and $t_3 = 70$ μm. Among these test joints the first one already got damaged during manufacturing itself. This shows that we can't manufacture the joint with thickness 50 μm. We have set-up an experiment to measure their spring constants. We have used two methods namely, static and dynamic method to estimate (k_θ) and compared with theoretical prediction.

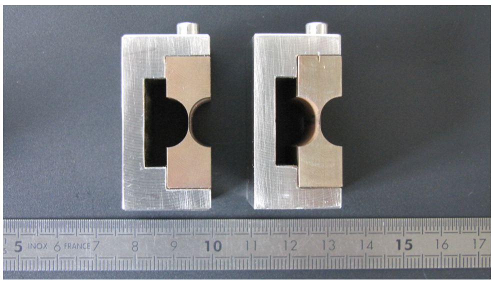

Figure 5.6: Test joints with rectangular flexure geometry

Static method: The experimental apparatus is shown in Fig. 5.7. The top part of the test joint is rigidly fixed on the heavy Al frame and another Al bar is rigidly fixed on the bottom part of the joint. The central part of the joint is the flexible part of the assembly. The angular stiffness is evaluated by placing known masses m onto the Al bar at known arm length L and noting the subsequent vertical displacements Δz as measured by the traveling microscope having 20 μm resolution. For every mass the displacement is measured by coinciding the microscope cross wire with the tip of a small pin on the Al bar at arm length L as shown in Fig. 5.7 and noting down the corresponding value from the vernier on the microscope. Due to this configuration (compound pendulum), the total or effective angular spring constant k is given by,

$$k = k_\theta + k_g \tag{5.24}$$

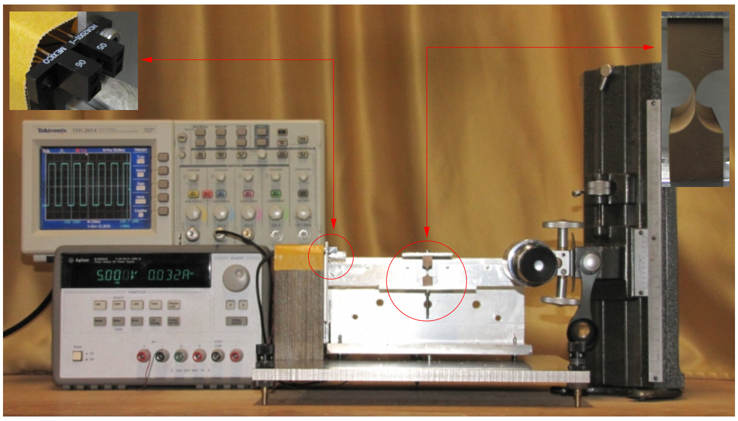

Figure 5.7: Experimental set-up. Enlarged view of flexure is shown. Enlarged view of photo detector, sensor and obstacle to measure the period of oscillation of the assembly is shown.

As already shown k_θ and k_g are given by (5.8) and (5.9) respectively. Where $\Delta\theta$ is the deflection due to the mass m, M is the total mass of the assembly below the center of the joint and h is the distance from the center of the joint to the center of mass of the entire assembly. The gravity term can be easily estimated from the Autodesk design software. Since now we know the value of the gravity term (k_g) and the effective angular constant (k), we can evaluate (k_θ) (see Fig. 5.8).

Dynamic method: The same set-up as shown in Fig. 5.7 is also used for the dynamic method. This method is an adapted version of relations (18) and (19) of Quinn's [3] paper. In this method we must precisely measure the oscillation period of the pendulum for the given pendulum configuration and estimate k_θ from that. As explained in the previous section, the stiffness of the assembly is due to flexure angular constant(k_θ) and due to gravity (k_g). If T_0 is the period of oscillation of the assembly, the dynamical equation of motion becomes,

$$\frac{4\pi^2 I_0}{T_0^2} = k_\theta + Mgh \tag{5.25}$$

where I_0 is the moment of inertia of the assembly about the axis of rotation and M is the mass of the assembly they are precisely $I_0 = 149.3 \times 10^{-6}\,\mathrm{kgm}^2$, $M = 0.080\,\mathrm{kg}$ and $h = 9.57\,\mathrm{mm}$, can be directly read from the Autodesk Inventor design. Instead of placing the known masses at given arm length L as like in the static method, here known masses ($m_n = n \cdot m_{test}$ $n = 0...4$; $m_{test} \simeq 8.75\,\mathrm{g}$ so that $4 \cdot m_{test} \simeq 35\,\mathrm{g}$ that is comparable with $M \simeq 80\,\mathrm{g}$, this is why we corrected the approximation made in the Quinn's paper) are placed below the effective centre of rotation of the flexure at known distance y or simply saying vertical distance of mass m_n from the centre of rotation, and hence (5.25) becomes,

$$\frac{4\pi^2 (I_0 + m_i y_i^2)}{T_i^2} = k_\theta + Mgh + m_i g y_i \tag{5.26}$$

$$i = 0, .., 4 \tag{5.27}$$

$$m_i = i m_{test}, i = 0, .., 4 \tag{5.28}$$

Now we know all the values in (5.26) other than the period of oscillation of the assembly for various m for evaluating k_θ. Using an optical photo-diode sensor, the period of oscillation have been measured. For this purpose a small obstacle is pasted on the Al bar. This obstacle cuts the light between the photodiode and the sensor, so the photo-sensor gives the TTL pulses. Measuring the time between the rising edges of these TTL signals by using the oscilloscope as shown in Fig. 5.9, we can precisely (1 ms) measure the oscillation period of the assembly for various masses (m_i) at distances (y_i). Fig. 5.10 shows the measured angular spring constants by the dynamic method.

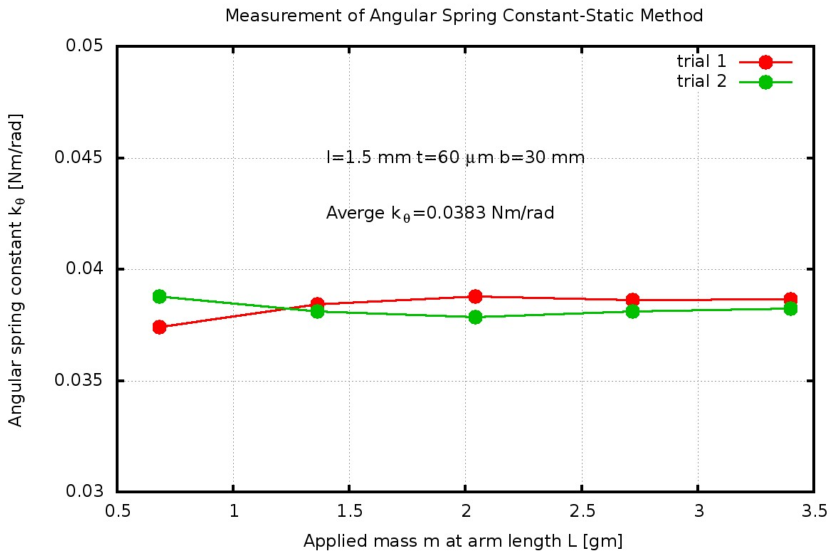

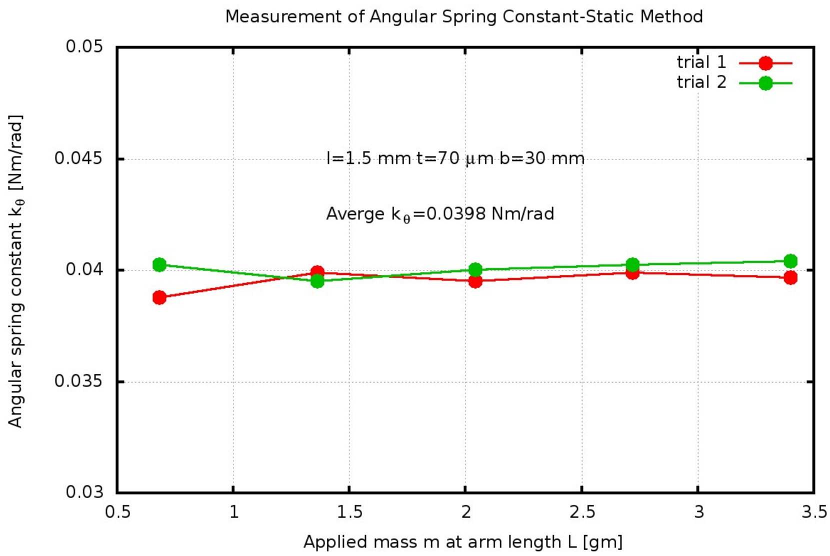

Figure 5.8: Measured angular spring constant by static method for 2 Trials. Top plot: Applied mass m [kg] vs k_θ [Nm/rad], for l=1.5 mm, t=60 μm and b=30 mm Bottom plot: Applied mass m [kg] vs k_θ [Nm/rad], for l=1.5 mm, t=70 μm and b=30 mm.

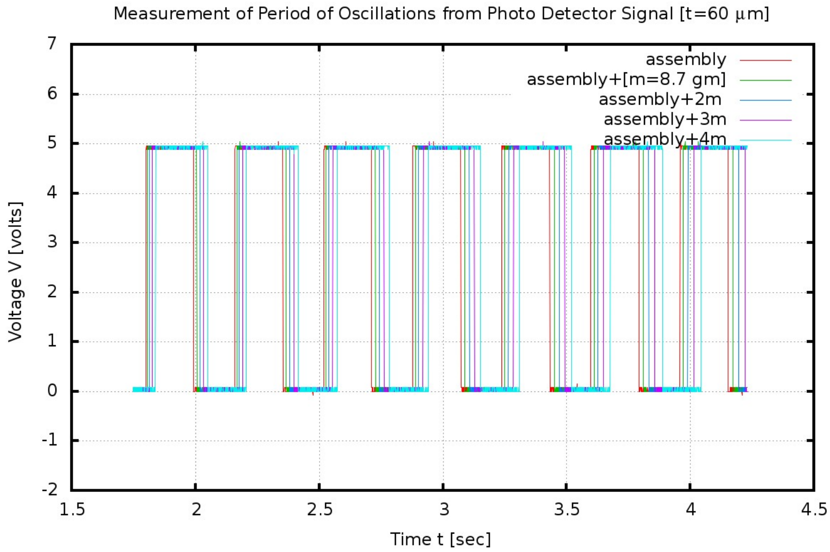

Figure 5.9: Oscilloscope traces of TTL signals from the photo-sensor from which the period of oscillation relative to the five different measurements with $m_n = n \cdot m_{test} \quad n = 0...4$ can be precisely (1 ms) measured.

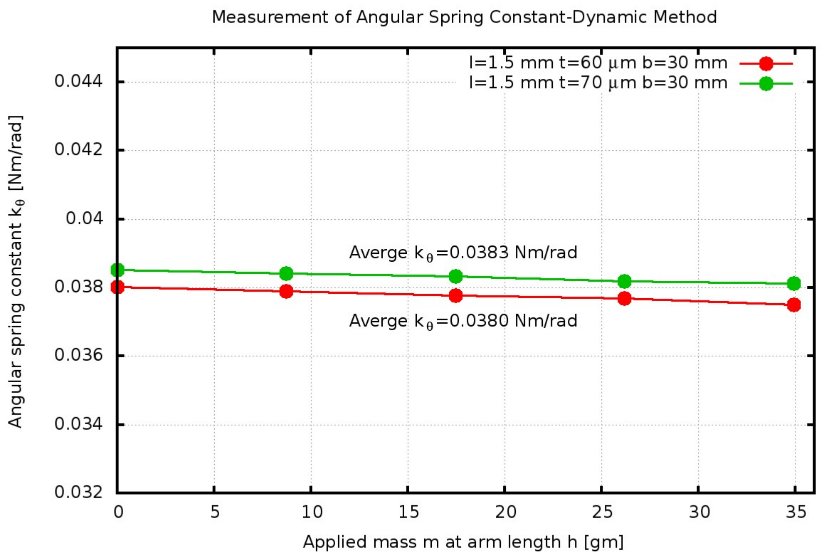

Figure 5.10: Measured angular spring constant by dynamic method. Top plot: Applied mass m [kg] vs k_θ [Nm/rad], for l=1.5 mm, t=60 μm and b=30 mm Bottom plot: Applied mass m [kg] vs k_θ [Nm/rad], for l=1.5 mm, t=70 μm and b=30 mm.

Table 5.4 reports the results of our measurements. We find that the two measured elastic constants are both lower than the theoretical value and that the 60 μm flexure elastic constant is close to that measured for the 70 μm one. The first fact can be explained by the thermal treatment of the flexures material giving a Young's modulus smaller than expected; the second fact can be explained by the machining tolerances, that have been quoted by the manufacturer at the level of few microns but are probably bigger.

Table 5.4: k_θ measurement results for the test flexure strips

Dimensions	Theory [Nm/rad]	Static Method [Nm/rad]	Dynamic Method [Nm/rad]
t=60 μm $l = 1.5$ mm and width=30 mm	0.044	0.038	0.038
t=70 μm $l = 1.5$ mm and width=30 mm	0.069	0.040	0.038

Based on the theoretical knowledge and these experimental measurements a new set of GGG joints have been manufactured with the geometrical parameters as given above. Their elastic constants (in both directions of the plane) have been measured on bench and are reported in Table 5.5.

Table 5.5: Angular spring constants of the GGG joints (Improved design)

Joint	Direction	Experimental (k_θ) (Nm/rad)
Top	(χ)	0.08±0.01
	(ψ)	0.08±0.01
Bottom	(χ)	0.10±0.01
	(ψ)	0.10±0.01
Central	(χ)	0.11±0.01
	(ψ)	0.09±0.01
Below bearing	(χ)	0.04±0.01
	(ψ)	0.03±0.01

By comparing Table 5.5 with Table 5.3 we can see that the GGG joints with the new design have lower stiffness than the old ones, especially the central joint of the coupling arm and the joint on the shaft below the ball bearings which are the most relevant. Moreover, we also notice a very good level of isotropy in the two directions – much better than with the old joints – which is very important to ensure the best performance in sensitivity of the rotating GGG accelerometer.

The GGG apparatus has therefore been assembled by replacing the old joints with the new ones.

References

[1] T. J. Quinn, C. C. Speake, R. S. Davis, W. Tew, Phys. Lett. A 197 (1995)

[2] Yakow M. Tseytlin, Rev. Sci. Instrum. 73, 3363-3368 (2002)

[3] T. J. Quinn *et al.*, Metrologia 23, 87-100 (1986/87)

[4] D. G. Blair *et al.*, Rev. Sci. Instrum. 64, 1899-1904 (1993)

[5] D. G. Blair *et al.*, Report

[6] J. Winterflood *et al.*, Physics Letters A 277, 143-155 (2000)

[7] A. Bertolini *et al.*, LIGO-Internal Working Note, (1999)

Chapter 6

GGG sensitivity at low frequencies

6.1 The measurements

The output data we acquire from the GGG experiment are the relative displacements of the test cylinders in 2 orthogonal directions (χ, ψ) of the sensitive plane of the GGG accelerometer perpendicular to the spin/symmetry axis. They are read 2^n times every turn by two capacitance bridges co-rotating with the accelerometer, i.e. 2^n is the number of data points acquired per spin period T_{spin}. Hence the data set is in the form of two time series (χ_i, ψ_i) with a given sampling time $\nu_{samp} = T_{spin}/2^n$. For GGG we have chosen $2^n = 32$, i.e. the data points are regularly spaced at ($2\pi/32$ radians) angular positions. This is achieved by means of an optical rotary encoder which for each data point (χ_i, ψ_i), provides also the associated phase angle of the rotating test cylinders relative to a fixed direction in the laboratory frame. The sampling frequency ν_{samp} is related to the spin frequency ν_{spin} as:

$$\nu_{samp} = 32\nu_{spin} \tag{6.1}$$

The digitally converted readings of the rotating bridges are sent from the rotating electronics in RS232 format for computer acquisition through an optical link, and are then time stamped by a *Rb* clock. They are de-modulated in the data analysis in order to obtain the relative displacement of the test cylinders in the non rotating laboratory frame through the relationship (written for one of the two directions and for the k-th turn):

$$x(k) = \frac{1}{16}\sum_{i=1}^{32} \chi^k(i)\cos(\vartheta^k(i)) \tag{6.2}$$

where $\chi^k(i)$ is the *i-th* datum of the *k-th* turn; $\vartheta^k(i)$ is the phase angle and $x(k)$ is the *k-th* datum in the non-rotating frame.

A set of data-quality check plots are usually produced for every experimental run:

- Time series of the Sampling time jitter, giving also a measurement of the spin speed noise.
- 1 mHz low pass filtered time series of bridge signals in order to monitor the behavior of the bridge electronics.
- Fast Fourier Transform (FFT) and Linear Spectral Density (LSD) of the bridge signals in order to monitor the noise components of the capacitance bridges.
- 1 mHz low pass filtered time series of displacements in the laboratory frame showing the low frequency behaviour of the experiment during the run.
- FFT and LSD of the displacements in the laboratory frame, giving the level of noise measured by the GGG accelerometer.
- Mean of the test masses relative displacements in the non rotating frame, giving the mean offsets typically due to fixed residual tilts of the shaft.

Since we are interested in low frequency effects (at the frequency of interest for GG and at the diurnal frequency) we need experiment runs of several days. Longer runs allow random noise sources such as electronics noise and thermal noise to be reduced. The spectral density of the test masses displacement noise at these frequencies, combined with the value of the differential period for that run, provides the corresponding sensitivity to differential accelerations.

6.2 Analysis of GGG output data and low frequency sensitivity

A 29 day run of GGG was performed from 27 December 2011 to 25 January 2012. The natural differential period of the test cylinders was $10\,s$, the spin frequency was $0.19\,\mathrm{Hz}$, the monolithic 2D CuBe joint described in Sec. 4.2 was mounted on the rotating shaft below the ball bearings for tilt attenuation. The test cylinders were suspended and coupled with 2D CuBe joints of the old design as described in Ch. 5.

The relative displacements of the test cylinders after de-modulation to the non-rotating horizontal plane of the lab, and after filtering out high frequency variations (above 1 mHz), are shown in Fig. 6.1. The FFT and SD of the relative displacement and differential accelerations of the test cylinders in the non-rotating plane are reported in Fig. 6.2. As we can see, at the frequency relevant for the GG experiment in space ($\nu_{GG} \simeq 1.7 \cdot 10^{-4}\,\mathrm{Hz}$) the relative displacement noise is about 180 pm and the corresponing differential acceleration noise is about $7 \cdot 10^{-11}\,\mathrm{ms}^{-2}$ (see [1]).

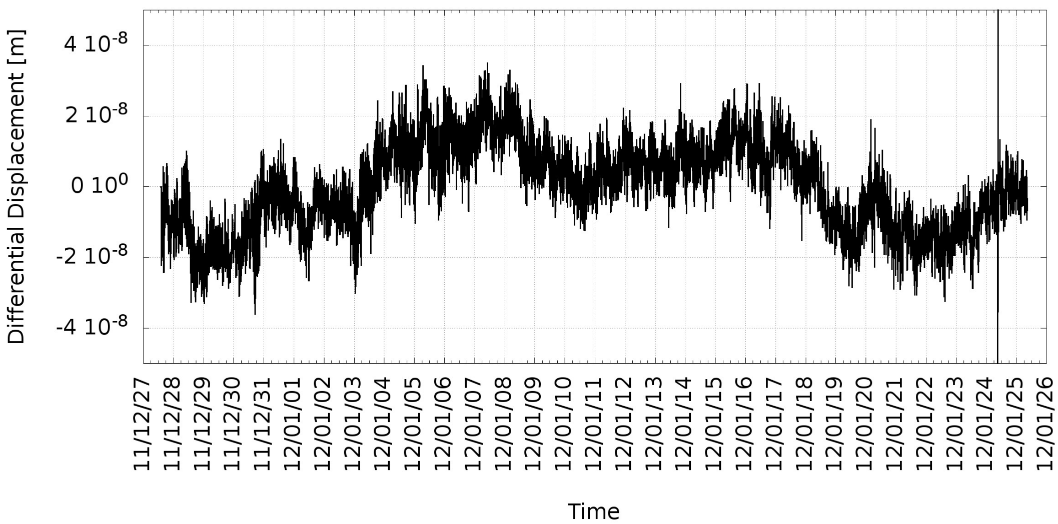

Figure 6.1: Time series of the relative displacements of the GGG test masses (frequencies above 1 mHz filtered out) in one direction of the horizontal plane of the lab during a 29 d (27 December 2011–25 January 2012) run.

The sensitivity of GGG to an EP violation in the field of the Sun is defined as:

$$\eta^{\odot}_{GGG} = \frac{\Delta a^{\odot}_{GGG}}{a^{\odot}_{GGG}} \tag{6.3}$$

where $\Delta a^{\odot}_{GGG} \simeq 3.4 \cdot 10^{-10}\,\mathrm{ms}^{-2}$ is the FFT of the differential acceleration of the test cylinders at the diurnal frequency $\nu_{day} = 1.16 \cdot 10^{-5}\,\mathrm{Hz}$ as given in Fig. 6.2 and

$$a^{\odot}_{GGG} \simeq \frac{GM_{\odot}}{R^2_{\oplus\odot}} \simeq 0.006\,\mathrm{ms}^{-2} \tag{6.4}$$

is the gravitational attraction from the Sun ($R_{\oplus\odot}$ is the Earth-Sun distance and $M_{\odot}$ the mass of the Sun). For test masses at latitude θ

$$a^{\odot}_{GGG}(\theta) \simeq \frac{GM_{\odot}}{R^2_{\oplus\odot}} \sin(\theta) \tag{6.5}$$

with $\theta_{Pisa} \simeq 43^{\circ}.7$. When the sun is at the equinoxes (Fig. 6.3) it is:

$$a^{\odot}_{GGG} \simeq \frac{GM_{\odot}}{R^2_{\oplus\odot}} \sin(\theta_{Pisa}) \simeq 0.0041\,\mathrm{m\,s}^{-2} \quad @ \text{ equinoxes} \tag{6.6}$$

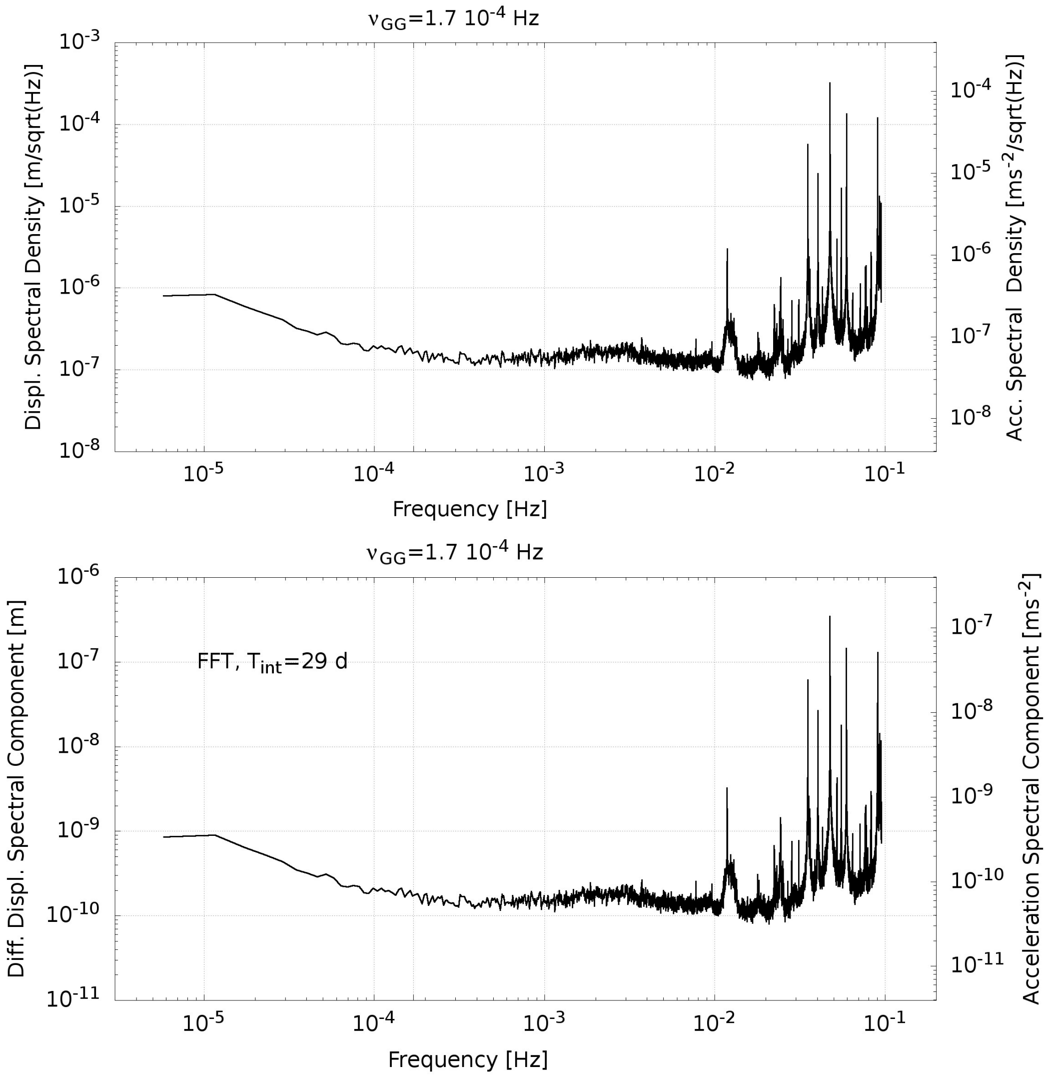

Figure 6.2: GGG noise performance as measured from a 29 d run. (Top): SD of the relative displacements and acceleration of the test cylinders in one direction of the horizontal plane of the lab; the GGG differential accelerometer is spinning at $\nu_{spin} = 0.19\,\mathrm{Hz}$ with the natural coupling frequency of 0.1 Hz. The measured relative displacement is $\simeq 1.8 \times 10^{-7}\,\mathrm{m\,Hz^{-1/2}}$ and the measured relative acceleration is $\simeq 6 \times 10^{-8}\,\mathrm{m\,s^{-2}\,Hz^{-1/2}}$ at the frequency $\nu_{GG} \simeq 1.7 \times 10^{-4}\,\mathrm{Hz}$, the orbital frequency relevant for GG in space. (Bottom): Measured relative test masses displacement and acceleration noise integrated over the full run duration. At ν_{GG}, we get an integrated differential displacement noise of $\simeq 1.8 \times 10^{-10}\,\mathrm{m}$ and a differential acceleration noise of $\simeq 7 \times 10^{-11}\,\mathrm{m\,s^{-2}}$ (taken from [1]).

while at the winter solstice it is (Fig. 6.4):

$$a^{\odot}_{GGG} \simeq \frac{GM_{\odot}}{R^2_{\oplus\odot}} \sin(\theta_{Pisa} + \epsilon) \simeq 0.0055\,\mathrm{m\,s^{-2}} \quad \text{@ winter solstice} \tag{6.7}$$

($\epsilon = 23°.5$). In the Northern hemisphere the maximum value of this acceleration occurs in the period December–January because this is both close to winter solstice and to the perihelion of the Earth orbit and it is:

$$a^{\odot}_{GGG} \simeq \frac{GM_{\odot}}{R^2_{\oplus\odot}(1 - e_{\oplus})^2} \sin(\theta_{Pisa} + \epsilon) \simeq 0.0057\,\mathrm{m\,s^{-2}} \tag{6.8}$$

As shown in Table 6.1, this run yields $\eta^{\odot}_{GGG} \simeq 6 \cdot 10^{-8}$.

It is worth recalling that $\Delta a = (2\pi/T_{diff})^2 \Delta r$, with $T_{diff} = 1/\nu_{diff}$ the natural period of oscillation of the test cylinders relative to each other. This means that the smaller the differential frequency (i.e. the longer the differential period), the more sensitive the GGG balance is to differential accelerations acting in between the test cylinders. A differential period twice as long makes the displacement in response to the

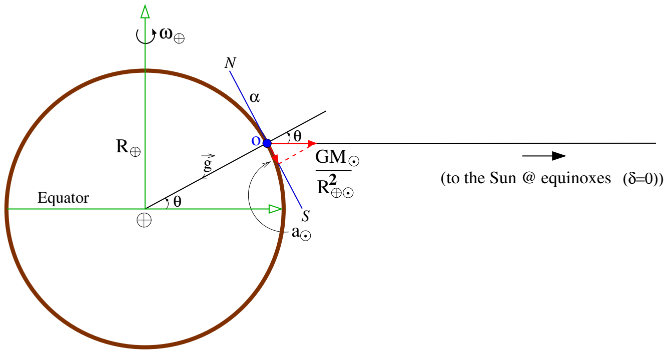

Figure 6.3: O is the location of GGG test masses at latitude θ, α is the horizontal plane of lab. The Sun is at the equinoxes.

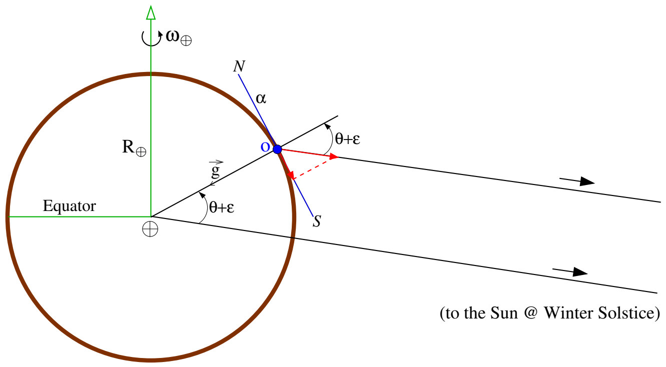

Figure 6.4: O is the location of GGG test masses at latitude θ, α is the horizontal plane of lab. The Sun lies in at the winter solstice when its declination is equal to the obliquity of the ecliptic $\epsilon = 23°.5$.

same differential acceleration four times larger; similarly, the capability of detecting relative displacements twice as small makes the instrument four times as sensitive to differential accelerations.

Table 6.1: GGG sensitivity to EP violation in the field of the Sun (run 27 Dec. 2011 - 25 Jan. 2012)

GGG–Sensitivity to EP violation in the field of the Sun	
Driving acceleration of the Sun $a^{\odot}_{GGG}$	$\simeq 0.0057\,\mathrm{m/s^2}$
Frequency of Interest	$\nu_{day} = 1.16 \times 10^{-5}$ Hz
Natural coupling period of the test masses T_{diff}	10 s
Integration time T_{int}	29 days
Differential acceleration sensitivity relative to the Sun $\Delta a^{\odot}_{GGG}$ [Fig. 6.2] @$\nu_{day} = 1.16 \times 10^{-5}$ Hz	$3.4 \times 10^{-10}\,\mathrm{m/s^2}$
Sensitivity to EP $\eta^{\odot}_{GGG} = \frac{\Delta a^{\odot}_{GGG}}{a^{\odot}_{GGG}}$ $\Delta a^{\odot}_{GGG} = (\frac{2\pi}{T_{diff}})^2 \Delta r^{\odot}_{GGG}$ $\eta^{\odot}_{GGG} \simeq 6 \times 10^{-8}$	

6.3 Conclusions

Low frequency tilt noise from terrain microseismicity and ball bearings irregularities is a major source of noise in the GGG differential accelerometer prototype of the similar instrument to fly in GG. In space the whole satellite is isolated and there are no motor and no bearings, therefore this noise is absent. On ground it must be reduced in order to test the performance of the prototype.

Passive tilt attenuation has proved much more effective than the active tilt control implemented in the past based on a commercial tiltmeter as sensor and PZT as actuators. Temperature variations, especially at low frequencies, affect the signal of the tiltmeter on which the loop is closed and therefore result in the reintroduction of spurious tilts by the actuators. Despite temperature stabilization such spurious low frequency tilts are a limitation to the GGG sensitivity.

We have shown that tilt noise can be very effectively reduced with a rotating monolithic 2D joint placed below the ball bearings. The monolithic structure avoids clamping issues. The location below the bearings ensures effectiveness in the reduction of shaft tilts caused not only by terrain microseismicity but also by irregularities in the bearings.

The geometrical design of the 2D joint responsible for tilt attenuation has recently been optimized and the improvement has been demonstrated by on bench measurements. The same type of design has been adopted for the 2D joints which suspend and couple the GGG test cylinders. Their stiffness has been reduced and isotropy has improved; the natural period of differential oscillation of the test cylinders has increased from 10 to 15 s. The GGG system has been assembled with the new suspensions after completion of their on bench characterization; after balancing and centering in the usual commissioning phase it has been set in rotation and the run is ongoing. A typical one month duration is planned, to be compared with the one month run performed with the previous joints and reported in Sec. 6.2. After completion of this run, the tilt rejection method described in Subsec. 4.2.2 will be implemented, for which all hardware components have been manufactured, and a further improvement is expected.

At present, the best GGG sensitivity is given by the run reported in Sec. 6.2. At the orbital frequency of GG the differential acceleration noise is $7 \cdot 10^{-11}\,\mathrm{ms}^{-2}$ and the relative displacement noise is 180 pm. In space GG is required to detect, at the same frequency, 0.6 pm displacements. In terms of differential acceleration GG is required to detect $8 \cdot 10^{-17}\,\mathrm{ms}^{-2}$, but it will have a sensitivity 3000 times better than GGG (due to the much weaker suspensions that can be used in space), which makes GGG in this run about a factor 300 worse than the GG target.

References

[1] A. M. Nobili, M. Shao, R. Pegna, G. Zavattini, S. G. Turyshev, D. M. Lucchesi, A. De. Michele, S. Doravari, G. L. Comandi, T. R. Saravanan, F. Palmonari, G. Catastini and A. Anselmi, Class. Quantum Grav. 29, 184011 (2012)

List of Figures

List of Tables

List of Symbols

EP	Equivalence principle
UFF	Universality of free fall
LLR	Lunar laser ranging
GG	"Galileo Galilei" space experiment
GGG	"Galileo Galilei on the ground" experiment
ν_{GG}	Orbital frequency of the GG satellite around the Earth
ν_{day}	Diurnal frequency at which the Sun moves around the GGG test masses
η	Eötvös parameter
η_{GG}	The sensitivity of GG to an EP violation in the field of the Earth
$\eta_{GGG}^{\odot}$	The sensitivity of GGG to an EP violation in the field of the Sun
$\Delta a_{GGG}^{\odot}$	Differential accelerations sensitivity of GGG at ν_{day}
$a_{GGG}^{\odot}$	Common acceleration from the Sun in the horizontal plane of the lab on the GGG test masses located at the latitude of Pisa
θ_{shaft}	Tilt angle of the shaft
θ_{ca}	Tilt angle of the coupling arm
m_r	Mass of the regulating body
l_r	Arm length of the regulating body
T_d (or) T_{diff}	Natural period of oscillations of the test cylinders relative to each other
ν_d	Natural frequency of oscillations of the test cylinders relative to each other
M_b, M_t	Masses of the inner and outer test cylinders
k_t, k_c, k_b	Angular elastic constants of the top, central and bottom laminar suspensions
k_{shaft}	Angular elastic constant of the 2D joint placed on the shaft below the bearings
M_{tot}	Total mass suspended from the shaft joint
L_t, L_b	Lengths of the top and bottom parts of the coupling arm
L_{equiv}	Equivalent arm length of the suspended system
Δr	Relative displacement in response to the diferential acceleration Δa
μ	Reduced mass of the two bodies have the same mass m
$\gamma_{\omega_{spin}}$	Damping coefficient of the oscillator rotating at angular velocity ω_{spin}
$\vec{L}$	Angular momentum of the body
ω_n	Natural angular frequency of oscillations of the test masses relative to each other
$\vec{\epsilon}$ (or) $\vec{\varepsilon}$	Offset or unbalance of the test masses from the rotation axis due to construction and mounting errors
(x, y, z)	Non-rotating inertial reference frame
(χ, ψ, z)	Rotating reference frame
$\vec{r}_{eq}$	Equilibrium position of the mass
$\vec{F}$	External constant force
Q	Quality factor
$\phi_{\omega_{spin}}$	Loss angle
g	Local acceleration due to gravity
$a^{\oplus}$	Horizontal component of the local gravitational acceleration
$\omega_{\oplus}$	Diurnal angular velocity of the Earth
$R_{\oplus}$	Radius of the Earth
θ	Latitude at which the test bodies are located
FFT	Fast Fourier Transform
LSD	Linear Spectral Density
PZT	Piezoelectric actuator
USB	Universal serial bus
IC	Integrated circuit
Δx_{cm}	Common mode displacement of the GGG test masses
Δx_{dm}	Differential mode displacement of the GGG test masses
ϵ_0	Permittivity of free space ($\epsilon_0 = 8.854 \times 10^{-12}$ F/m)
ADC	Analog-to-digital converter
DAC	Digital-to-analog converter
A_{bridge}	Gain of the capacitance bridge
A_{ampli}	Gain of the amplifier
σ_{discr}	Discretization noise of the ADC

N_{bits}	Number of resolution bits of the ADC
ν_{samp}	Sampling frequency of the capacitance bridge
ν_{spin}	Spin frequency of the test cylinders
C_0	Nominal value of the capacitance of each capacitance plate facing one of the test cylinders
(a, b)	Gaps between the capacitance plates and the surfaces of the test cylinders
C_1, C_2	Capacitances of each plate resulting from the displacements
LED	Light emitting diode
$FPGA$	Field-programmable gate array
PC	Personal computer
$T_{pendulum}$	Oscillation period of the suspended pendulum
M_{sp}	Total mass of the suspended pendulum
k	Spring constant
I_{sp}	Moment of inertia of the suspended pendulum relative to an axis passing through the suspension point
h_{sp}	Distance from the center of mass to the suspension point of the pendulum
$\nu_{\chi diff}, \nu_{\psi diff}$	Natural frequencies of differential oscillations of the test cylinders in the χ and ψ directions
$\nu_{\chi com1}, \nu_{\psi com1}$	Natural frequencies of first common mode oscillations of the test cylinders in the χ and ψ directions
$\nu_{\chi com2}, \nu_{\psi com2}$	Natural frequencies of second common mode oscillations of the test cylinders in the χ and ψ directions
r_w	Amplitude of the whirl orbital motion
T_n (or) T_w	Natural or whirl period
Q_{spin}	Quality factor at spin frequency
ν_{whirl}	Whirl frequency
τ_w	Time constant of the whirl motion
φ	Phase
$F_{suspension}$	Elastic force of the suspension
DAQ	Data acquisition
γ	Damping coefficient
ζ	Damping ratio
I	Moment of inertia
α	Terrain tilt angle
a	Horizontal acceleration of the ground
χ_{tilt}	Tilt attenuation factor
k_θ	Torsional elastic constant
TTL	Transistor-transistor logic
T_{spin}	Spin period
$x(k)$	k^{th} datum of the relative displacement of the test cylinders in the non-rotating laboratory frame
$\chi^k(i)$	i^{th} datum of the k^{th} turn of the relative displacement of the test cylinders in the rotating frame
$\vartheta^k(i)$	Phase angle of the i^{th} datum
G	Newton's gravitational constant
$M_\odot$	Mass of the Sun
$R_{\oplus\odot}$	Earth–Sun distance